

The official bi-monthly publication of Bhabha Atomic Research Centre



BARC

newsletter



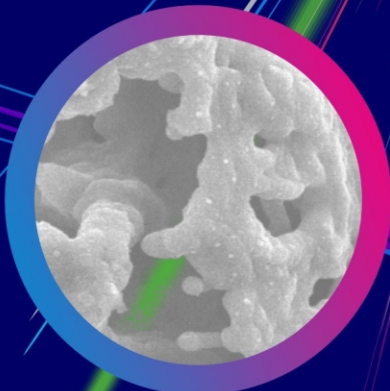
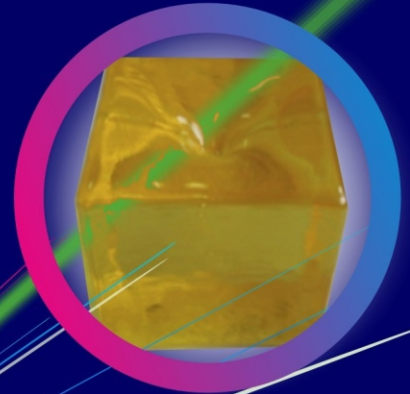
March-April 2024

ISSN: 0976-2108

● Healthcare Applications

● Radiation Safety Studies

● Advanced Laser Technologies



Interdisciplinary Research
for futuristic technologies

Editors

Dr. S. Adhikari
Manoj Singh

Editorial Assistant

Madhav N

Content Curation & Design

Dinesh J. Vaidya
Jyoti Panda
Madhav N

Newsletter Committee

Chairman

Dr. S. Adhikari

Members

Dr. L.M. Pant
Dr. B.K. Sapra
Dr. C.N. Patra
Dr. S. Santra
Dr. V.H. Patankar
Dr. J. Padma Nilaya
Dr. S. Mukhopadhyay
Dr. V. Sudarsan
Dr. Tessy Vincent
Dr. S.R. Shimjith
Dr. Sandip Basu
Dr. K.K. Singh
Dr. Kinshuk Dasgupta
Dr. I.A. Khan
Dr. Deepak Sharma
P. P. K. Venkat
Dr. K. Tirumalesh
Dr. Arnab Dasgupta
Dr. S. Banerjee
Dr. V.K. Kotak

Member Secretary & Coordination

Madhav N



BARC Newsletter
March-April 2024
ISSN: 0976-2108



The uniqueness of BARC **@ interdisciplinary research**

Bhabha Atomic Research Centre (BARC) is proud to be home to one of India’s prominent cutting-edge scientific research projects in the highly advanced domain of nuclear energy. The centre is at the forefront of national efforts for establishing India’s foothold in fundamental research with an overlay on high tech areas of science, new and fast emerging digital transformations through unlocking numerous interdisciplinarity; all with a human face to ensure the fruits of scientific research translate sufficiently to bring about a positive change in the lives of people down to the grassroots.

In this issue of newsletter, we pull back the curtain on the sustained multidisciplinary research in BARC with a renewed focus on latest developments in beam technologies and its interlinkages in biomaterials development and quantum computing research. Expanding the scope of radiation-assisted healthcare continues to be one of the key mandates of Department of Atomic Energy and BARC, successful implementation of these programs, and the related developments are captured in this issue.

A key pillar of BARC’s life-long mission is to sensitize and engage citizens of all demographics, enthuse them about the exciting aspects of scientific research and technology development underpinning BARC’s research and its positive impact on overall S&T landscape. The National Science Day celebration served as a perfect platform to bring all stakeholders under one umbrella thereby helping us in our efforts to fulfill the desired objective.

We’re glad that you have an opportunity to experience the happenings across limited verticals at BARC, in this issue of the newsletter. It will definitely motivate and encourage the researchers, in particular, those who are closely associated with the multi-disciplinary programs aimed at bringing out new and futuristic technologies that would steadily catapult India to become technologically self-sufficient in the times ahead.

We wish the readers will enjoy this issue of newsletter as another testament of accomplishments possible in interdisciplinary scientific research.

S. Adhikari
Associate Director, KMG, BARC

Manoj Singh
Head, SIRD, BARC

- **EDITORIAL:** Dr. S. Adhikari and Manoj Singh **3**
- **Abstracts of Technical Manuscripts in Hindi** *i-iv*
Hindi Section and SIRD Newsletter Editorial Team, BARC

RESEARCH AND DEVELOPMENT

- 1 Dosimetric Characterization of 10 MeV Electron Accelerator Developed by BARC for Food Irradiation** **7**
Shatabdi Chakrabarty, Rajesh Kumar, Nitin Kakade, Jyoti Sharma, R. B. Chavan, Munir Pathan, S. D. Sharma, P. C. Saroj and B. K. Sapra
- 2 Wet Chemical Synthesis of Hydroxyapatite Powder and Estimation of Curcumin and Berberine Drug Loading Efficacy** **12**
Prabha Soundharraj, Sunita Kedia, Goutam Chakraborty, Arati Magar and J. Padma Nilaya
- 3 CW CO₂ Laser Induced Graphene on Biodegradable Surface** **16**
Tatsat Dwivedi, Hrithik Gupta, Sunita Kedia, R. C. Das and J. Padma Nilaya
- 4 Indigenous Development of Cold Atmospheric Pressure Plasma Device for Multipurpose Applications** **19**
Rajib Kar, Vishakha Bende, Vandan Nagar, Vanita Sekar, and Namita Maiti
- 5 Optical Power Enhancement of High Repetition Rate Copper Vapor Laser MOPA Chains** **23**
Anil S. Nayak, Rajasree Vijayan, Dheeraj Singh, S. Mandal, B. V. Gangwane and V. S. Rawat
- 6 Laser Cooling of Atoms Down to Doppler Limit: A Step Towards Atomic Qubit** **27**
B. Pal, R. Behera, S. Baruah, T. B. Pal, S. R. Chowdhury, G. Sridhar, B. Dikshit, S. Kundu and Archana Sharma
- 7 Atomistic Technology of Materials (ATOM) Software Suite for Computing Properties of Molecules and Materials** **30**
Nirbhay Chandorkar, Anil Boda, Pooja Sahu, Kislay Bhatt, Sk. Musharaf Ali and K. Rajesh
- 8 Synthesis and Characterization of Lead Silicate Glasses for Radiation Shielding Window Application** **35**
P. Nandi, D. Dutta, B. Sanyal, R. Mishra, M. Goswami and A. K. Arya
- 9 Comparison of Annual Maximum Series and Annual Exceedance Series** **40**
Saha Dauji, Pankaj Srivastava, Kapilesh Bhargava, A. Baburajan, I. V. Saradhi and A. Vinod Kumar
- 10 Solar Powered Two Phase Variable Frequency Inverter Drive** **44**
Ashish Kumar Pandey, Mahesh B. Patil, Vivek Sanadhya and S. Mukhopadhyay

POPULAR SCIENCE

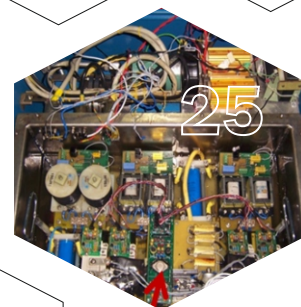
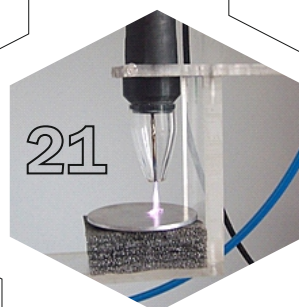
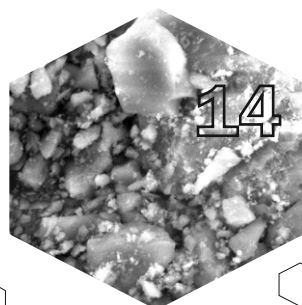
- **Hunting the Magnetic Monopoles** **48**
Krishna Kumar Singh
- **Indigenous IRMA Kit for Routine Estimation of Serum Thyroglobulin in Thyroid Cancer Patients: Radiation Medicine Centre, BARC Completing a Decade of Accomplishment** **52**
Chandrakala Gholve and Nawab Singh Baghel
- **Up-gradation of Animal House from a Conventional one to a State-of-the-art Facility: Experience at BARC's Radiation Medicine Centre in Mumbai** **54**
Yogita Shete and Sandip Basu

NEWS & EVENTS

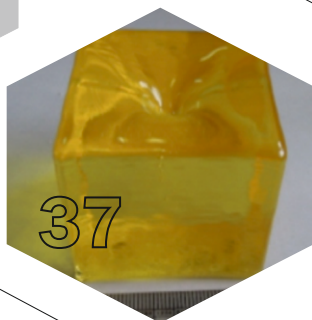
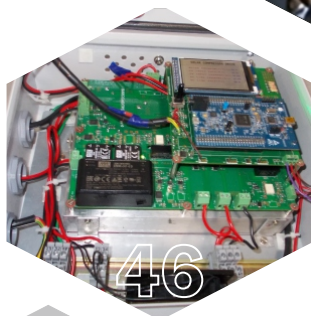
- **TROMBAY COLLOQUIUM: Indigenous Indian Vaccine - The Story of Human Compassion & Cooperation** **59**
Prof. (Dr.) Balram Bhargava, Chief of Cardiothoracic Centre, AIIMS
- **BARC water technologies now bring smiles to train commuters** **60**
Chemical Engineering Group and SIRD Editorial Team, BARC

CONNECT

- **NSD-2024: BARC celebrates National Science Day** **61**
- **BARC, Central Ground Water Board join hands for capacity building in Isotope Hydrology** **62**



CONTENTS



FORTHCOMING ISSUE

Research and Development



HEALTH, FOOD & AGRICULTURE

- Radioimmunotherapy of HER2 positive breast cancer patients.
- Affordable organic ligands for prostate cancer management.
- Mutation breeding by augmenting genomic resources in pulse crops.
- A new gamma ray-induced mutant of groundnut for cultivation in Gujarat and Maharashtra.
- Biosensors for Pesticides: From concept to technology
- Valorization of fish waste.

This page intentionally left blank

बीएआरसी न्यूज़लेटर मार्च-अप्रैल 2024 अंक में सम्मिलित तकनीकी आलेखों के सारांश

खाद्य किरणन के लिए बीएआरसी द्वारा विकसित 10 MeV इलेक्ट्रॉन त्वरक का मात्रामिति अभिलक्षणन

शताब्दी चक्रवर्ती¹, राजेश कुमार*¹, नितिन काकड़े¹, ज्योति शर्मा², आर. बी. चव्हाण², मुनीर पठान¹, एस. डी. शर्मा¹, पी. सी. सरोज² और बी. के. सपरा¹

¹विकिरण विज्ञान भौतिकी एवं सलाहकार प्रभाग, स्वास्थ्य, संरक्षा एवं पर्यावरण वर्ग, भाभा परमाणु अनुसंधान केंद्र, ट्रॉम्बे-400085, भारत

²इलेक्ट्रॉन किरणपुंज केंद्र, किरणपुंज प्रौद्योगिकी विकास वर्ग, खारघर, नवी मुंबई-410210, भारत

सारांश

यह लेख बीटीडीजी, बीएआरसी द्वारा विकसित 10 MeV विकिरण आवृत्ति (आरएफ) इलेक्ट्रॉन लीनियर एक्सेलेरेटर (लाइनेक) से खाद्य किरणन संबंधी शोध प्रस्तुत करता है। अन्वेषण का उद्देश्य इलेक्ट्रॉन किरणपुंज की एकरूपता का आकलन करना, प्रतिशत गहन-डोज (पीडीडी) वितरण और किरणपुंज गुणवत्ता सूचकांक का मूल्यांकन करना और किरणपुंज की उत्पादन क्षमता को सत्यापित करना है। अध्ययन में मिर्च पाउडर किरणन की डोज एकरूपता का सत्यापन करना भी शामिल है। रेडियोक्रोमिक B3 फिल्मों को नियमित डोसिमीटर के रूप में नियोजित किया गया है। परिणाम स्कैन और कन्वेयर दिशाओं के साथ अवशोषित डोज में ~ 8 प्रतिशत भिन्नता प्रदर्शित करते हैं। तुलना से यह पता चलता है कि ईबीसी लाइनेक की मात्रामिति विशेषताएँ 9 MeV मेडिकल लाइनेक के साथ सुमेलित हैं। एकल-पक्षीय उद्दासन के लिए डोज एकरूपता अनुपात (डीयूआर) के आधार पर उत्पाद की मोटाई को समायोजित करने की सिफारिशें समांगी जल के समतुल्य पदार्थ के लिए 3.3 से.मी. और मिर्च पाउडर पैकेट के लिए 8 से.मी. के साथ की जाती हैं। विषमांगी पदार्थों और विभिन्न डी. यू. आर. मान के लिए मामले-विशिष्ट विश्लेषण की आवश्यकता पर जोर देने वाली सिफारिशें भी प्रस्तुत की जाती हैं।

(पूरे लेख के लिए पृष्ठ संख्या 7 देखें।)

हाइड्रॉक्सीपेटाइट पाउडर का गीला रासायनिक संश्लेषण और करक्यूमिन और बर्बेरिन ड्रग लोडिंग प्रभावकारिता का अनुमान

प्रभा सुंदरराज¹, सुनीता केडिया^{1,2}, गौतम चक्रवर्ती^{1,2}, आरती मगर¹ और जे. पद्मा निलया^{1,2}

¹लेसर एवं प्लाज्मा प्रौद्योगिकी प्रभाग, भाभा परमाणु अनुसंधान केंद्र, ट्रॉम्बे-400085, भारत

²होमी भाभा राष्ट्रीय संस्थान, अणुशक्तिनगर, मुंबई-400094, भारत

सारांश

हाइड्रॉक्सीपेटाइट (एचएपी) खनिज मानव हड्डी का ~70% है। इसलिए, सिंथेटिक एचएपी ऑर्थोपेडिक्स के संदर्भ में एक प्रमुख स्थान रखता है। सिंथेटिक एच. ए. पी. जलभित्ति की सीमाओं और कुछ सामान्य कैंसररोधी दवाओं से जुड़े खराब अवशोषण को दूर करने के लिए एक वाहक के रूप में कार्य कर सकता है। वर्तमान कार्य में, एचएपी पाउडर को संरचनात्मक अभिलक्षणन के बाद सरल रासायनिक वर्षा विधि द्वारा संश्लेषित किया गया था। इसके अलावा, अवशोषण माप का उपयोग करके भौतिक अवशोषण के माध्यम से करक्यूमिन और बर्बेरिन जैसी एंटीट्यूमर दवाओं के वाहक के रूप में एचएपी पाउडर की क्षमता का अध्ययन किया गया है। संश्लेषित एचएपी पाउडर में बर्बेरिन (27 प्रतिशत) की तुलना में करक्यूमिन दवा के प्रति ~77% की उच्च लोडिंग प्रभावकारिता पाई गई है।

(पूरे लेख के लिए पृष्ठ संख्या 12 देखें।)

बायोडिग्रेडेबल सतह पर CW CO₂ लेसर प्रेरित ग्राफीन

तत्सत द्विवेदी^{1,2}, हृतिक गुप्ता³, सुनीता केडिया^{1,2}, आर. सी. दास^{1,2} और जे. पद्मा निलया^{1,2}

¹लेसर एवं प्लाज्मा प्रौद्योगिकी प्रभाग, भाभा परमाणु अनुसंधान केंद्र, ट्रॉम्बे-400085, भारत

²होमी भाभा राष्ट्रीय संस्थान, अणुशक्तिनगर, मुंबई-400094, भारत

³सोमैया कॉलेज, मुंबई विश्वविद्यालय, मुंबई-423601, भारत

सारांश

जैव निम्नीकरण अवस्तर, नामतः नारियल के खोल की सतह का लेसर-प्रेरित ग्राफेनाइजेशन प्रतिवेदित है। सेटअप में एक कार्बन डाइऑक्साइड (सीओ) लेसर, मैकेनिकल चॉपर, ट्रांसलेशन स्टेज और लेसर आउटपुट पावर की निगरानी के लिए एक संसूचक शामिल था। इष्टतम लेसर प्रवाह पैरामीटर और स्कैन गति निर्धारित की गई थी, जो पिछले लेख के साथ बहुत भिन्न थी। उत्पादित ग्राफीन की गुणवत्ता का मूल्यांकन रमन स्पेक्ट्रोस्कोपी का उपयोग करके किया गया था। स्कैनिंग इलेक्ट्रॉन माइक्रोस्कोप प्रतिबिंबों ने लेसर शक्ति के आधार पर छिद्रपूर्ण फोम और रेशेदार बंडलों सहित विभिन्न एल. आई. जी. संरचनाओं को प्रदर्शित किया। इसके अतिरिक्त, उत्पन्न लेसर प्रेरित ग्राफीन (एल. आई. जी.) की गुणवत्ता का मूल्यांकन करने के लिए एक्स. आर. डी. और शीट प्रतिरोध माप आयोजित किए गए।

(पूरे लेख के लिए पृष्ठ संख्या 16 देखें।)

बहुउद्देशीय अनुप्रयोगों के लिए शीत वायुमंडलीय दाब प्लाज्मा उपकरण का स्वदेशी विकास

राजीब कर^{1,2}, विशाखा बेंदे², वंदन नागर^{2,3}, वनिता सेकर¹, और नमिता मैती^{1,2}

¹लेसर एवं प्लाज्मा प्रौद्योगिकी प्रभाग, भाभा परमाणु अनुसंधान केंद्र, ट्रॉम्बे-400085, भारत

²होमी भाभा राष्ट्रीय संस्थान, अणुशक्तिनगर, मुंबई-400094, भारत

³खाद्य प्रौद्योगिकी प्रभाग, भाभा परमाणु अनुसंधान केंद्र (बीएआरसी), ट्रॉम्बे-400085, भारत

सारांश

शीत वायुमंडलीय दाब प्लाज्मा (सीएपीपी) प्रौद्योगिकी अपनी कम लागत, सरलता और सक्रिय प्रजातियों को बनाने की क्षमता के कारण ध्यान आकर्षित कर रही है। यह आवरण, उत्कीर्णन, सतह उपचार और चिकित्सा अनुप्रयोगों के लिए प्रतिबद्ध है। वर्तमान अध्ययन में, हमने टेस्ला कॉइल सिद्धांत के आधार पर स्वदेशी रूप से अभिकल्पित 10 MHz वायुमंडलीय दाब प्लाज्मा जेट का उपयोग किया है। इसके बाद अभिकल्पित उपकरण को रासायनिक नक्काशी के साथ-साथ इसकी बहुउद्देशीय प्रभावकारिता दिखाने के लिए जीवाणु निष्क्रियता के लिए लागू किया गया था। हमारे अवलोकनों से पता चला कि यह उपकरण CF_4 और O_2 जैसी जटिल आणविक प्लाज्मा गैसों का प्रबंधन कर सकता है। लगभग 20 वॉट विद्युत के स्तर पर काम करने वाले उपकरण के साथ प्रभावी जीवाणुनाशक प्रभाव प्राप्त किए जा सकते हैं, जबकि कुशल उत्कीर्णन तब प्राप्त की जा सकती है जब उपकरण लगभग 80 वॉट विद्युत पर काम करता है।

(पूरे लेख के लिए पृष्ठ संख्या 19 देखें।)

(ii)

उच्च पुनरावृत्ति दर कॉपर वेपर लेसर एमओपीए श्रृंखलाओं की ऑप्टिकल शक्ति में वृद्धि

अनिल एस. नायक*, राजश्री विजयन, धीरज सिंह, एस. मंडल, बी.वी. गंगवाने और वी. एस. रावत

प्रगत ट्यूनेबल लेसर अनुप्रयोग प्रभाग, भाभा परमाणु अनुसंधान केंद्र, ट्रॉम्बे-400085, भारत

सारांश

कॉपर वेपर लेसर (सी. वी. एल.) एक उच्च शक्ति स्पंदित लेसर प्रणाली है जिसमें उच्च प्रतिकृति दर होती है। लेसर स्रोत विद्युत चुम्बकीय विकिरण के दृश्य स्पेक्ट्रम (510 एवं 578 nm) में है। महत्वपूर्ण अनुप्रयोगों में से एक रेडियोन्यूक्लाइड के उत्पादन के लिए स्थिर आईसोटोपों का लेसर आधारित प्रबलीकरण है जिसका उपयोग कैंसर चिकित्सा के लिए चिकित्सा अनुप्रयोगों (लू. वाईबी, एसएम) में किया जाता है। सी. वी. एल. सटीक रूप से ट्यूनेबल नैरो बैंड ड्राई लेसर के लिए एक पंप स्रोत के रूप में कार्य करता है। यह वेपर व्यक्तिगत सीवीएल की ऑप्टिकल शक्ति को बढ़ाने की कार्य प्रणाली का वर्णन करता है, जिससे मास्टर ऑसिलेटर पावर एम्पलीफायर (एमओपीए) विन्यास में विन्यासित सीवीएल से बिजली उत्पादन में वृद्धि होती है। स्पंद ट्रांसफॉर्मर के प्राथमिकी में डीसी रेज़ोनेन्ट चार्जिंग सर्किट में ऊर्जा भंडारण धारिता को बढ़ाकर शक्ति वृद्धि प्राप्त की जाती है। यह शोधपत्र व्यक्तिगत प्रणाली की ऑप्टिकल शक्ति वृद्धि के साथ-साथ सीवीएल एमओपीए श्रृंखला से आउटपुट और इसकी लंबी अवधि की ऑप्टिकल शक्ति स्थिरता को दर्शाता है। स्पंद ट्रांसफॉर्मर के द्वितीयक पर चार्जिंग समय, आवेश हस्तांतरण समय, प्रसार देरी और वोल्टेज प्रवर्धन पर इन संशोधनों के प्रभाव का वर्णन इस शोधपत्र में उपयुक्त रूप से किया गया है।

(पूरे लेख के लिए पृष्ठ संख्या 23 देखें।)

डॉप्लर सीमा तक परमाणुओं की लेसर कूलिंग: परमाणु क्यूबिट की दिशा में एक कदम

बी.पाल¹, आर. बेहरा¹, एस. बरुआ¹, टी.बी. पाल¹, एस.आर. चौधरी¹, जी. श्रीधर^{1,2}, बी. दीक्षित^{1,2}, एस. कुंडू¹ और अर्चना शर्मा^{1,2}

¹एटीएलएडी, भाभा परमाणु अनुसंधान केंद्र, ट्रॉम्बे-400085, भारत; ²होमी भाभा राष्ट्रीय संस्थान, अणुशक्तिनगर, मुंबई-400094, भारत

सारांश

जब परमाणु बिना किसी अवांछित गड़बड़ी के अंतरिक्ष में पूर्वनिर्धारित स्थानों में ट्रेप हो जाते हैं और नियंत्रित किए जाए तो क्वांटम बिट्स (क्यूबिट्स) के रूप में काम कर सकते हैं। परमाणुओं को ऑप्टिकल या चुंबकीय सूक्ष्म ट्रेप में कुशलता से फंसाने के लिए परमाणु क्लाउड के तापमान को कुछ माइक्रोकेल्विन तक कम करने की आवश्यकता होती है। परमाणु क्यूबिट्स को प्रदर्शित करने के प्रयास में, हमने हाल ही में एक मैग्नेटो-ऑप्टिकल ट्रेप का उपयोग करके सीज़ियम ठंडे परमाणु क्लाउड के डॉप्लर सीमित न्यूनतम तापमान (~ 130 μ K) को ड्रॉप किया और प्राप्त किया है। तापमान को छोड़ने और पुनः प्राप्त करने की तकनीक द्वारा मापा गया था। हमारा अगला लक्ष्य उप-डॉप्लर शीतलन तकनीकों द्वारा तापमान को और नीचे ~ 5 μ K तक कम करना है ताकि परमाणुओं को ऑप्टिकल जाली में फंसाया जा सके जहां क्यूबिट्स का उलझाव प्राप्त किया जा सके।

(पूरे लेख के लिए पृष्ठ संख्या 27 देखें।)

आणविक और पदार्थों के कम्प्यूटिंग गुणधर्मों के लिए पदार्थ का परमाणु प्रौद्योगिकी (एटम) सॉफ्टवेयर सूट

निर्भय चंदोरकर¹, अनिल बोड़ा², पूजा साहू², किसलय भट्ट¹, एस.के. मुशर्रफ अली² और के. राजेश¹

¹कंप्यूटर प्रभाग, भाभा परमाणु अनुसंधान केंद्र, ट्रॉम्बे-400085, भारत

²रासायनिक इंजीनियरिंग प्रभाग, भाभा परमाणु अनुसंधान केंद्र, ट्रॉम्बे-400085, भारत

सारांश

एटम (पदार्थ की परमाणु प्रौद्योगिकी) पहल का उद्देश्य परमाणु और आणविक अनुकार के लिए इनपुट, आउटपुट और विश्लेषण को सुव्यवस्थित करने के लिए उपयोगकर्ता के अनुकूल समर्पित एक सॉफ्टवेयर सूट विकसित करना है। यह शोधपत्र एटम सॉफ्टवेयर के एक उप मॉड्यूल के अभिकल्पन और विकास पर केंद्रित है, जिसे विशेष रूप से "गैस भंडारण और पारगमन" से संबंधित गणनाओं के लिए विकसित किया गया है। पाइथन और जांगो वेब फ्रेमवर्क का उपयोग करके कार्यान्वित, एप्लिकेशन उपयोगकर्ताओं को नौकरी पंजीकरण, मौजूदा कार्यों को देखने और संपादित करने, फ़ाइल अपलोड और प्रसंस्करण, और गणना किए गए डेटा के व्यापक विश्लेषण जैसी कार्यक्षमताओं के साथ सशक्त बनाता है। इस मंच के माध्यम से, उपयोगकर्ता विभिन्न डेटा सेटों में शामिल हो सकते हैं, जिसमें ऊर्जा, अवशोषण ऊर्जा, हाइड्रोजन गैस प्रसार, पारगमन और घुलनशीलता शामिल हैं, जिससे पूरी तरह से विश्लेषण किया जा सकता है। सावधानीपूर्वक अभिकल्पित की गई डेटाबेस योजना के साथ, एप्लिकेशन कुशलता से महत्वपूर्ण कार्य से संबंधित जानकारी, फ़ाइलों, ऊर्जा प्रोफाइल, मापदंडों और आवृत्तियों को व्यवस्थित और संग्रहीत करता है। कुल मिलाकर, यह अनुप्रयोग एक मूल्यवान संसाधन के रूप में खड़ा है, जो परमाणु अनुकरण डेटा के प्रबंधन और परीक्षण के लिए एक उपयोगकर्ता के अनुकूल इंटरफ़ेस और मजबूत विश्लेषणात्मक उपकरण दोनों प्रदान करता है। इसका महत्व पदार्थ विज्ञान और रसायन विज्ञान के क्षेत्र में काम करने वाले शोधकर्ताओं को बहुत लाभ पहुंचाने की इसकी क्षमता में निहित है।

(पूरे लेख के लिए पृष्ठ संख्या 30 देखें।)

[iii]

विकिरण परिरक्षण विंडो अनुप्रयोग के लिए लेड सिलिकेट कांचों का संश्लेषण एवं अभिलक्षण

पी. नंदी¹, डी. दत्ता^{2,4}, बी. सान्याल^{3,4}, आर. मिश्रा¹, एम. गोस्वामी^{1,4} और ए. के. आर्य^{1,4}

¹कांच एवं प्रगत पदार्थ प्रभाग, भाभा परमाणु अनुसंधान केंद्र, ट्रॉम्बे-400085, भारत

²रेडियो रसायन प्रभाग, भाभा परमाणु अनुसंधान केंद्र, ट्रॉम्बे-400085, भारत

³फूड प्रौद्योगिकी प्रभाग, भाभा परमाणु अनुसंधान केंद्र, ट्रॉम्बे-400085, भारत

⁴होमी भाभा राष्ट्रीय संस्थान, अणुशक्तिनगर, मुंबई-400094, भारत

सारांश

हमने 2 2 3 2 अलग-अलग घटकों के साथ BaO-PbO-K O-B O-SiO कांच प्रणाली का संरचना अनुकूलन किया है। हमने 10 mm मोटे नमूने में 550 m पर 80% की आवश्यक ऑप्टिकल पारदर्शिता के साथ 4.5 gm/cc का अधिकतम घनत्व प्राप्त किया। ऑप्टिकल, तापीय, यांत्रिक, संरचनात्मक एवं विकिरण परिरक्षण गुणधर्मों में परिवर्तनों का अध्ययन करने के लिए कांच को Co-60 गामा कक्ष में किरणित किया गया था। रेखिक क्षीणन गुणांक गामा विकिरण से पहले और बाद में समान रहा, जो कांच को एक अच्छी विकिरण परिरक्षण पदार्थ के रूप में पुष्टि करता है। CeO के साथ डोप किए गए कांच ने 100 kGy तक भूरे रंग के विरुद्ध विकिरण प्रतिरोध दिखाया। 2 रमन स्पेक्ट्रा ने विकिरण के बाद-Si-O-Si-वलय संरचना में परिवर्तन दिखाया, जिससे अपवर्तक सूचकांक में वृद्धि हुई। विकिरण के बाद गैर-संकरण ऑक्सीजन में वृद्धि देखी गई जिसके परिणामस्वरूप संक्रमण तापमान (टीजी) और कांच की कठोरता में कमी आई। पॉज़िट्रॉन विलोपन लाइफटाइम स्पेक्ट्रोस्कोपी (पी. ए. एल. एस.) मापों का उपयोग करते हुए हमने किरणन के बाद रिक्त स्थान/मुक्त मात्रा में वृद्धि देखी है। यहाँ रिपोर्ट की गई लेड सिलिकेट संरचना में आवश्यक ऑप्टिकल और परिरक्षण गुणधर्म हैं और इसमें संभावित विकिरण परिरक्षण विंडो अनुप्रयोग है।

(पूरे लेख के लिए पृष्ठ संख्या 35 देखें।)

तारापुर में वर्षा का ई. वी. ए. विश्लेषण: वार्षिक अधिकतम श्रृंखला एवं वार्षिक अतिरेक श्रृंखला की तुलना

साहा दौजी^{1,2}, पंकज श्रीवास्तव¹, कपिलेश भार्गव^{3,2}, ए. बाबूराजन⁴, आई. वी. सारधि⁵ और ए. विनोद कुमार^{5,2}

¹परमाणु पुनश्चक्रण बोर्ड, भाभा परमाणु अनुसंधान केंद्र, मुंबई-400094, भारत

²होमी भाभा राष्ट्रीय संस्थान, अणुशक्तिनगर, मुंबई-400094, भारत

³इंजीनियरिंग सेवा वर्ग, भाभा परमाणु अनुसंधान केंद्र, ट्रॉम्बे-400085, भारत

⁴पर्यावरण सर्वेक्षण प्रयोगशाला, पर्यावरण निगरानी एवं मूल्यांकन प्रभाग, भाभा परमाणु अनुसंधान केंद्र, तारापुर-400504, भारत

⁵पर्यावरण निगरानी और मूल्यांकन प्रभाग, भाभा परमाणु अनुसंधान केंद्र, ट्रॉम्बे-400085, भारत

सारांश

नाभिकीय सुविधाओं और बाढ़ अध्ययन के लिए अभिकल्पन मापदंडों का पता लगाने के लिए अवक्षेपण एक महत्वपूर्ण विचारणीय पहलू है। किसी विशेष अवधि के लिए किसी स्थल पर होने वाली उच्चतम वर्षा का अनुमान चरम मूल्य विश्लेषण (ई. वी. ए.) द्वारा लगाया जाता है। ई. वी. ए. के नमूना चयन के लिए, दो संभावित दृष्टिकोण वार्षिक अधिकतम श्रृंखला (ए. एम. एस.) और वार्षिक सीमा से अधिक श्रृंखला (ए. ई. एस.) हैं, जिनमें से प्रत्येक की अपना-अपना सामर्थ्य और सीमाएँ हैं। सामान्य रूप से नाभिकीय स्थलों और विशेष रूप से तारापुर के लिए अत्यधिक वर्षा पर अधिकांश अध्ययनों में, असतत वर्षा माप के लिए वार्षिक अधिकतम श्रृंखला दृष्टिकोण अपनाया गया था। तारापुर के लिए अब 24 वर्षों (1997-2020) के लिए निरंतर उच्च-रिज़ॉल्यूशन (प्रति घंटा) वर्षा डेटा उपलब्ध होने के साथ, वर्तमान लेख तारापुर में वर्षा के ई. वी. ए. की तुलना करता है, जो भारतीय वर्षा स्थितियों के लिए लागू होने पर उनकी संबंधित सीमाओं की पहचान करने के लिए दोनों दृष्टिकोणों का उपयोग करके आयोजित किया जाता है।

(पूरे लेख के लिए पृष्ठ संख्या 40 देखें।)

[iv]

सौर ऊर्जा से संचालित दो चरण परिवर्तनीय आवृत्ति इन्वर्टर ड्राइव

आशीष कुमार पांडे *, महेश बी. पाटिल, विवेक संध्या और एस. मुखोपाध्याय

नियंत्रण एवं उपकरण प्रभाग, भाभा परमाणु अनुसंधान केंद्र (बीएआरसी), ट्रॉम्बे-400085, भारत

सारांश

यह शोधपत्र सिंगल फेज इंडक्शन मोटर (आईएम) ड्राइविंग फिक्स्ड स्पीड रेसिप्रोकेटिंग या रोटरी कंप्रेसर की गति को नियंत्रित करने के लिए थ्री-लेग इनवर्टर टोपोलॉजी में इसुलेटेड गेट बाइपोलर ट्रांजिस्टर (आईजीबीटी) मॉड्यूल का उपयोग करते हुए टू फेज परिवर्तनीय आवृत्ति ड्राइव (वीएफडी) के अभिकल्पन और विकास को प्रदर्शित करता है, जो आमतौर पर एयर कंडीशनिंग अनुप्रयोगों में उपयोग किए जाते हैं। यह ड्राइव 3 किलोवाट की पावर रेटिंग तक सिंगल-फेज इंडक्शन मोटर्स के कैपेसिटर-लेस ऑपरेशन करने में सक्षम है। इसे सोलर पीवी पैनल और सिंगल फेज एसी पावर सोर्स दोनों के साथ संचालित किया जा सकता है। प्रमुख औद्योगिक विशेषताओं जैसे कि अन्तर्वाह धारा नियंत्रण, मृदु आरंभ और विभिन्न सुरक्षा योजनाओं को वीएफडी प्रणाली अभिकल्पन में शामिल किया गया है। फर्मवेयर कार्यान्वयन के साथ-साथ कम लागत वाले कॉम्पैक्ट इन्वर्टर स्टैक का हार्डवेयर अभिकल्पन प्रस्तुत किया गया है। वीएफडी में अधिकतम पावर प्वाइंट ट्रैकिंग-आधारित (एमपीपीटी) एल्गोरिदम लागू किया गया है और इसे तब लाया जा सकता है जब यह सौर इनवर्टर स्थापित सौर पैनल पर अधिकतम बिजली उपयोग के लिए एकमात्र भार हो। दीवार पर लगे औद्योगिक बाड़े में रखे ड्राइव का परीक्षण, 2-TR वातानुकूलन इकाई का उपयोग करके किया गया था और परिणाम प्रस्तुत किए गए हैं।

(पूरे लेख के लिए पृष्ठ संख्या 44 देखें।)

Radiation Safety Studies

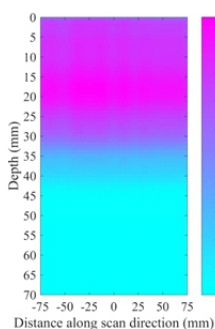
1

Dosimetric Characterization of 10 MeV Electron Accelerator Developed by BARC for Food Irradiation

Shatabdi Chakrabarty¹, Rajesh Kumar^{*1}, Nitin Kakade¹, Jyoti Sharma², R. B. Chavan², Munir Pathan¹, S. D. Sharma¹, P. C. Saroj² and B. K. Sapra¹

¹Radiological Physics and Advisory Division, Health, Safety & Environment Group, Bhabha Atomic Research Centre, Trombay – 400085, INDIA

²Electron Beam Centre, Beam Technology Development Group, Kharghar, Navi Mumbai- 410210, INDIA



2D-Dose plane for 10 MeV EBC LINAC

ABSTRACT

This article delves into the dosimetry of food irradiation from a 10 MeV radiofrequency (RF) electron linear accelerator (LINAC) developed by BTDG, BARC. The investigation aims to assess the uniformity of the electron beam, evaluate Percentage Depth-Dose (PDD) distribution and Beam Quality Index, and verify the reproducibility of the beam. The study also includes dose uniformity verification of chili powder irradiation. Radiochromic B3 films have been employed as routine dosimeters. Results demonstrate ~8% variation in absorbed dose along the scan and conveyor directions. Comparison reveals that the dosimetric characteristics of the EBC LINAC is in agreement with a 9 MeV medical LINAC. Recommendations for adjusting product thickness based on dose uniformity ratios (DUR) of 2.3 for single-sided exposure are made with 3.3 cm for homogeneous water equivalent materials and 8 cm for chili powder packets. Recommendations emphasizing the need for case-specific analyses for heterogeneous materials and different DUR values are also presented.

KEYWORDS: Electron beam irradiation, Food irradiator dosimetry, Film dosimetry

Introduction

Food irradiation refers to the process of subjecting food products like bulbs, roots, vegetables, fruits, seafood, meat, spices, animal feed etc. to ionizing radiation. This process entails the transfer of energy from ionizing radiation source into the treated product. Purpose of irradiation are sprouting inhibition, shelf life extension, insect disinfection, reduction in pathogenic micro-organisms etc. [1]. The quantity of irradiated food is increasing, predominantly in the Asia-Pacific region and the Americas [2]. Studies performed by U.S. Food and Drug Administration (FDA) and the World Health Organization (WHO) confirmed the safety of food irradiation [3, 4, 5].

Gamma radiation from ¹³⁷Cs and ⁶⁰Co electron beams up to 10 MeV energy and X-rays with maximum 5 MeV energy are used to treat food [1, 2]. The benefits of electron beam primarily stem from its clean and room temperature processing, minimal or complete elimination of additional chemicals, simple ON/OFF type machine operation [6], high throughput, safe radiation handling [7] and no chance of recontamination [8]. A radio frequency (RF) 10 MeV electron linear accelerator (LINAC) has been indigenously developed in India by Beam Technology Development Group, Bhabha Atomic Research Centre (BARC) for multi-product irradiation, including food, and is operational at Electron Beam Centre (EBC), Kharghar, Navi Mumbai.

As per design, thermoionically generated 50 keV electrons from electron gun are accelerated to 10 MeV beam in

1 m long coupled-cavity LINAC. Electromagnetic wave at RF range, generated from a 2856 MHz and 6 MW Klystron, is used for acceleration inside the LINAC. Electron beam is passed to the scan horn through the magnetic sweep scanner and comes out in the atmosphere through a Titanium exit window while sweeping a distance of 1m. A vacuum of 10⁻⁷ torr is maintained in the accelerating system. Cooling mechanisms and ozone removal system are in place to carry away excess heat and ozone (from scan horn area) [9]. Products to be irradiated are placed on conveyor system that can move with speeds varying from 0.1 – 10 m/min, equipped with metallic product rack. Distance between the exit window and the top surface of product boxes is approximately 45 cm [6]. The current operational characteristics of the irradiator include a beam energy of 10 MeV, an average beam power of 5 kW, a scanning

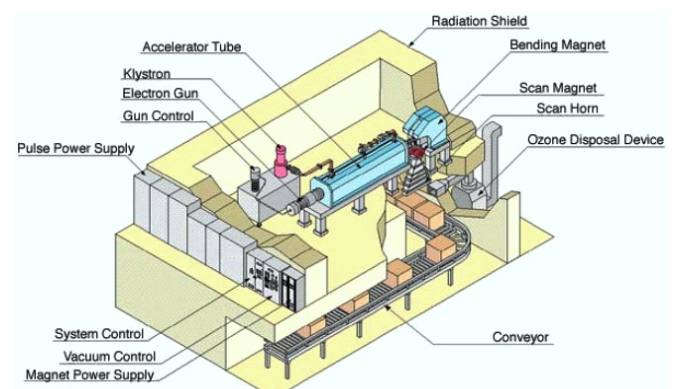


Fig.1: A standard electron beam irradiator (IAEA TRS 481).

*Author for Correspondence: Rajesh Kumar
E-mail: rajeshr@barc.gov.in

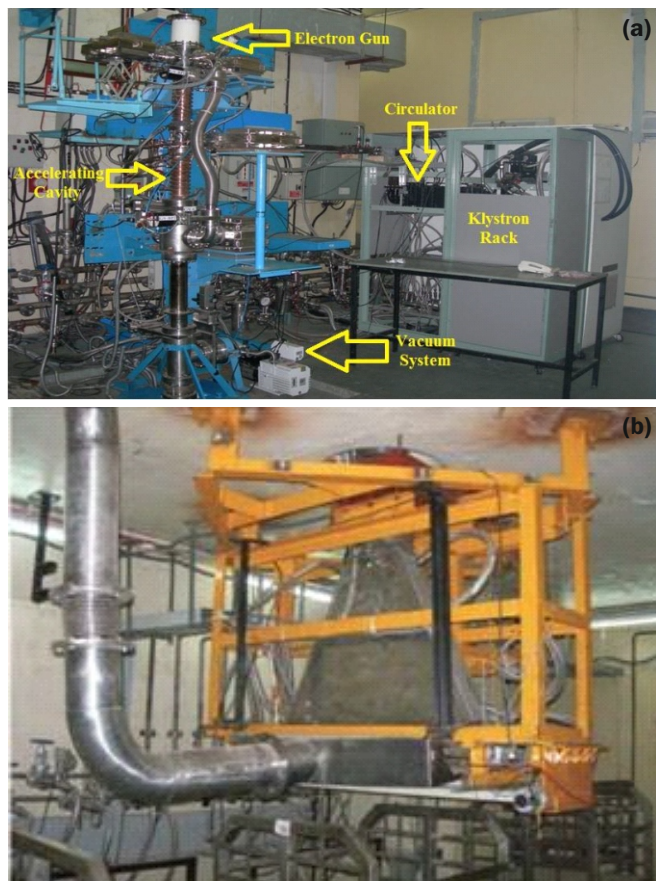


Fig.2: (a) Overview, (b) Scan horn of RF LINAC at EBC, Kharghar [9].

length of 1000 mm and a dose rate per unit area of 3.3 kGy per pass at a conveyor speed of 1 m/min [7]. A standard electron beam accelerator and the accelerator situated at EBC are shown in Fig.1 and Fig.2, respectively.

Stable, repeatable and reliable operation of such high power accelerators are quite challenging tasks [8]. The goals of the current investigation are to examine uniformity of the electron beam, evaluation of the Percentage Depth-Dose (PDD) distribution and Beam Quality Index and verify the reproducibility of the beam. Chili powder was also irradiated for further confidence in the experiments performed.

Material and Methods

Dosimeters

Routine dosimetry systems are used for absorbed dose assessments like dose mapping and process monitoring for quality control [1, 2, 10]. Radiochromic films are frequently used as routine dosimeters because of long shelf life, low atomic number and thus food product equivalence, stable response, simple readout procedure etc. [1]. In this study, radiochromic B3 films have been used. These are thin polyvinyl butyral films containing the leucocyanide of pararosaniline. The colorless film changes to deep pink color when exposed to radiation and the intensity of color is directly related to the amount of dose received. Practically measurable dose range with these films is 1-150 kGy [11]. Spectrophotometric measurements, which are non-destructive, can be performed with maximum sensitivity at 552 nm [6]. In this study, optical density of the films was measured using Genesys-20 portable spectrophotometer (Thermo Electron Corp., USA). The measurements have been performed after a gap of 48 h, post irradiation. Un-irradiated films are also measured to get the net absorbance due to exposure.

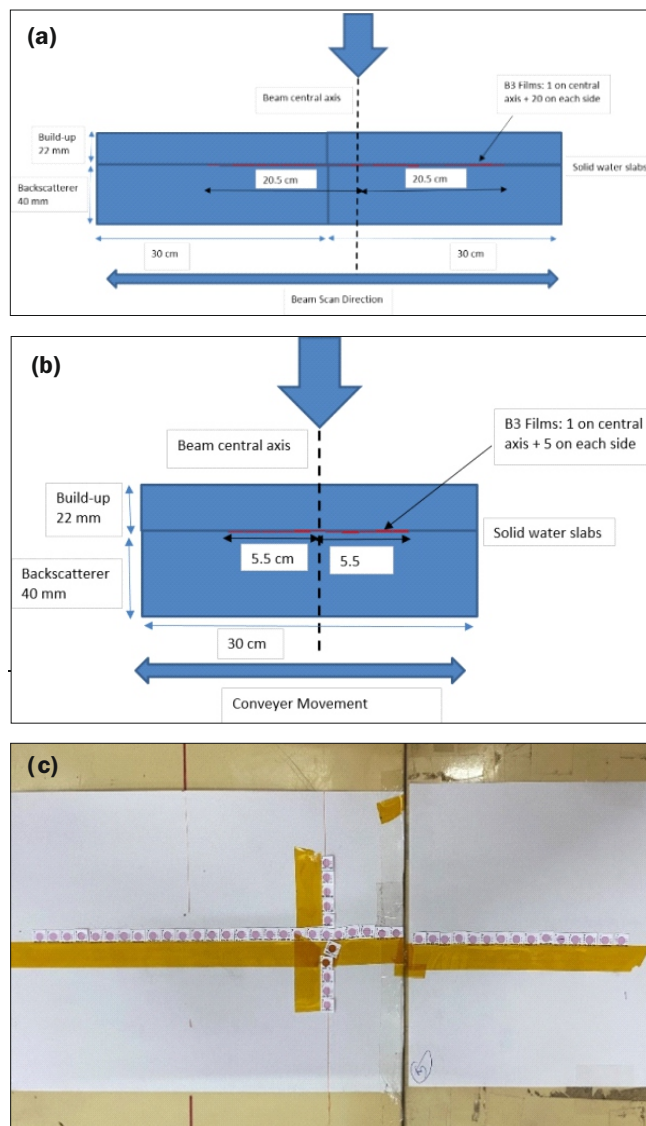


Fig.3: Measurement set-up for beam uniformity: (a) along beam scan direction, (b) along conveyer movement direction, (c) photograph of irradiated samples arranged as exposed.

Beam uniformity

On a 60 x 30 x 4 cm³ solid water slab, forty-one B3 films were placed along the beam scan direction and eleven B3 films along the conveyor movement direction. The films were kept at depth of 2.2 cm. Centre-to-centre distance between two films was 1 cm. The exposure set-up is as shown in Fig.3. Radiation was delivered at 45 mA beam current and 1.4 kW beam power through 15 passes at 1 m/min conveyor speed.

Percentage Depth-Dose (PDD) distribution and beam quality index in terms of R_{50}

Solid water slabs, 30 x 30 cm², of varying thicknesses were arranged in several combinations and B3 films positioned so that the films were at different thicknesses during irradiation. Four sets of these combinations were created to facilitate measurements at all necessary depths. One such experimental set up is shown in Fig.4. Radiation was administered with a beam current of 45 mA and a beam power of 1.4 kW, utilizing 15 passes at a conveyor speed of 1 m/min.

The beam quality index R_{50} , which is the half-value depth in water and R_p , which is the practical range in water of the measured electron beam are calculated using the empirically derived relationships given in ICRU Report 35 [12]:

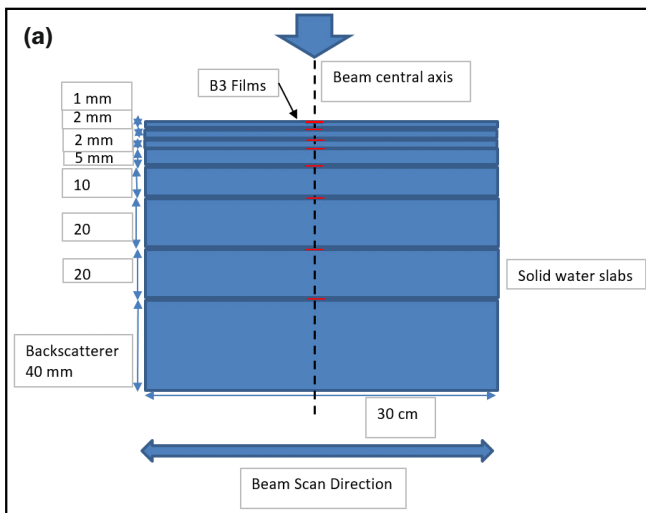


Fig.4: Measurement set-up of PDD (a) Layout (b) photograph.

$$E_a \text{ (MeV)} = 2.33 R_{50} \text{ (cm)} \quad \text{if } 5 \text{ MeV} < E_a < 35 \text{ MeV}$$

$$E_p \text{ (MeV)} = 0.22 + 1.98 R_p + 0.0025 R_p^2 \quad (R_p \text{ in cm})$$

$$\text{if } 1 \text{ MeV} < E_a < 50 \text{ MeV}$$

where E_a is the average electron beam energy at the entrance surface of water and E_p is the most probable electron beam energy.

Dose uniformity during chilli powder irradiation

A 60 x 35 x 16 cm³ cardboard box is filled with chilli powder packets placed in the central volume 50 x 35 x 8 cm³ in two layers. In each layer, 8 packets are kept in two rows. B3 films were placed on top of each packet and also at the bottom packets. The measurement arrangement is depicted in Fig.5. Radiation with beam current of 45 mA and beam power of 1.4 kW was given through 15 passes at 1 m/min conveyor speed.

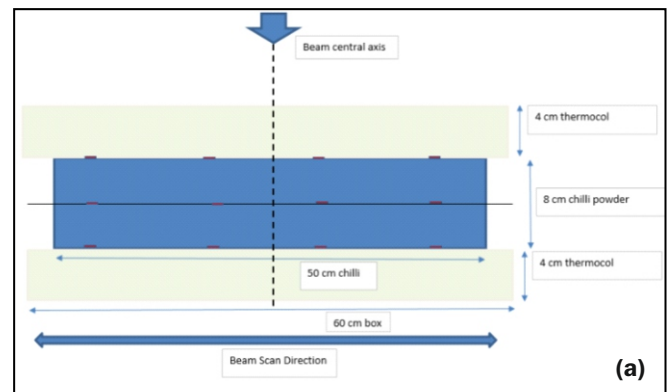


Fig.5: Measurement set-up of dose uniformity in chilli powder irradiation (a) Layout (b) photograph.

Dose uniformity in the chilli powder box is quantified by Dose Uniformity Ratio (DUR), which is the ratio of maximum to minimum dose in the product box. While irradiators are typically engineered to achieve a low DUR, such as ≤ 1.5 , numerous food products can accommodate a higher uniformity ratio of 2 or even 3 [1]. In practice, DUR less than 2.3 for food is considered acceptable.

Reproducibility of delivered dose

On 30 x 30 x 4 cm³ solid water slab, 3 B3 films were placed along the beam scan direction. Centre-to-centre distance between two films was 1 cm. A solid water phantom of dimensions 30 x 30 x 2 cm³ was placed on the films to act as build-up. The exposure set-up is shown in Fig.6. Films were changed and this experiment was repeated thrice. Radiation beam current of 33 mA and 1.4 kW power was delivered through 20 passes at 1 m/min conveyor speed.

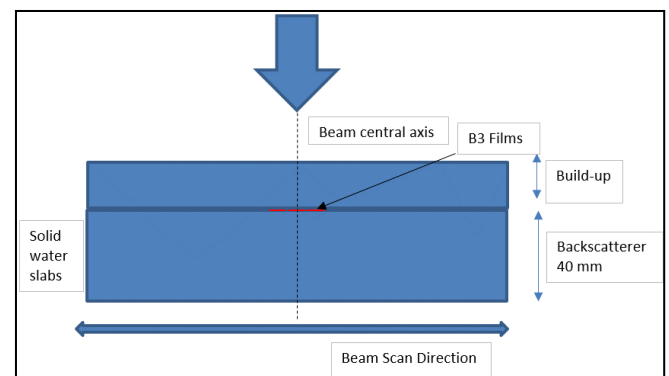


Fig.6: Measurement set-up of repeatability.

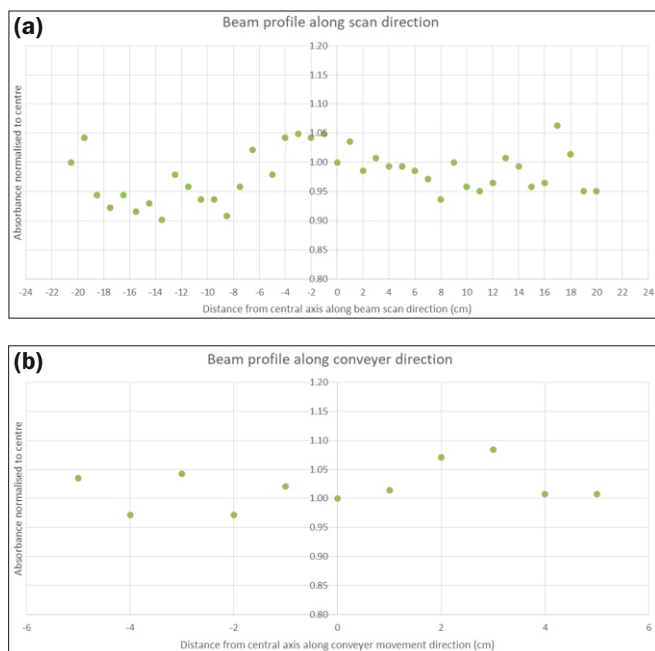


Fig.7: Beam profile (a) along beam scan direction, (b) along conveyer movement direction.

Results and Discussion

Beam uniformity

Normalized to the centre, the absorbed dose varies between 0.90-1.06 along scan direction and 0.97-1.08 along conveyer direction. Beam profiles in both scan and conveyer directions are shown in Fig.7.

Percentage Depth-Dose (PDD) distribution and beam quality index in terms of R_{50}

PDD in solid water slabs is shown in Fig.8.

Using the empirical relationships from ICRU 35, the following parameters were estimated.

Half-value depth $R_{50} = 3.3$ cm

Mean electron beam energy (E_a) = 7.7 MeV

Practical electron range (R_p) = 4.2 cm

Most probable energy (E_p) = 8.6 MeV

Dose Uniformity during chilli powder irradiation

Considering all the of chili powder packets, the DUR is found to be 2.22, with maximum dose at bottom plane of first layer or top plane of second layer and minimum at bottom plane of lowest layer. Therefore, if chili powder is filled till 8 cm below 4 cm of thermocol and exposed from a single side, the DUR value is 2.22 which is within the acceptable limit of 2.3.

Reproducibility of delivered dose

Maximum 14% variation from grand mean is observed.

Comparison with electron beam from 10 MeV Medical LINAC

Parameters of medical LINAC are stable and well established. To compare the PDD of 10 MeV EBC electron beam, dose distribution in a water phantom for electron beam of field size 20×20 cm² and energies 6, 9, 12, 15 and 18 were computed using a radiotherapy treatment planning system. Medical LINAC used in the study, does not have option to produce 10 MeV electron beam. Hence, the calculated PDD values for the mentioned energy levels were used to establish

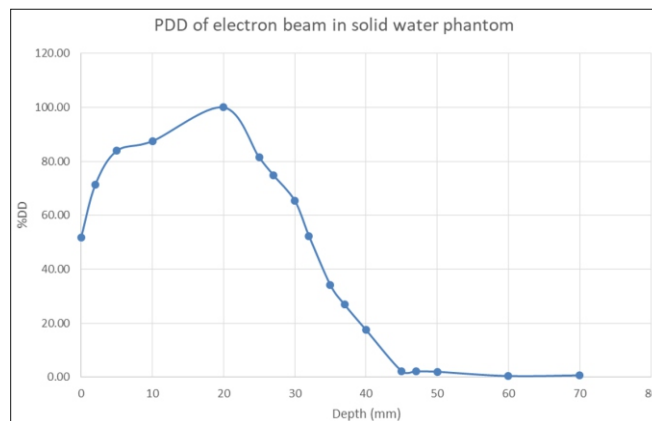


Fig.8: Measured PDD of electron beam in solid water phantom.

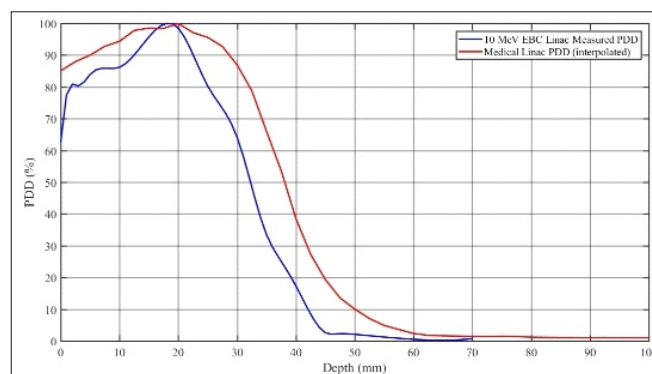


Fig.9: Measured PDD of EBC LINAC and computed PDD of Medical LINAC for 10 MeV.

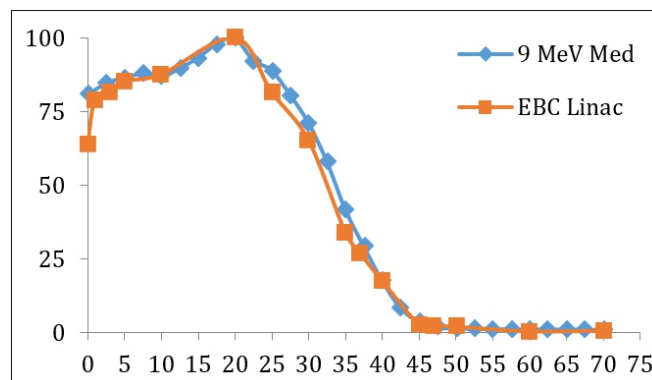


Fig.10: Measured PDD of EBC LINAC and computed PDD of 9 MeV Med LINAC.

the PDD for 10 MeV using the interpolation method. Fig.9 shows the comparison of PDD of EBC and Medical LINAC. It is evident from Figure 9 that the energy of EBC LINAC is less than 10 MeV medical LINAC. Fig.10 shows the PDD curve of 9 MeV electron beam from a Medical LINAC and 10 MeV EBC LINAC. Table-1 shows the comparison of different dosimetry parameters. It can be inferred that measured EBC data is in good agreement with 9 MeV Medical LINAC data.

A 3D dose cube of dimension $40 \times 40 \times 40$ cm³ was computed based on the measured PDD and dose along the scan direction for EBC LINAC. From this, a 2D-Dose distribution plane for field size of 15×15 cm² were compared with data obtained for 10 MeV medical LINAC. Both the dose distributions are shown in Fig.11, which shows that DUR= 2.3 can be achieved till about 3.3 cm in 10 MeV EBC LINAC, whereas the same can be obtained till approximately 3.9 cm in 10 MeV Medical LINAC.

Table 1: EBC and 9 MeV medical LINAC dosimetric parameters.

Parameters	9 MeV Medical LINAC	10 MeV EBC LINAC
R_{50} (cm)	3.4	3.3
R_p (cm)	4.3	4.2
E_p (MeV)	8.8	8.6
E_a (MeV)	7.9	7.7

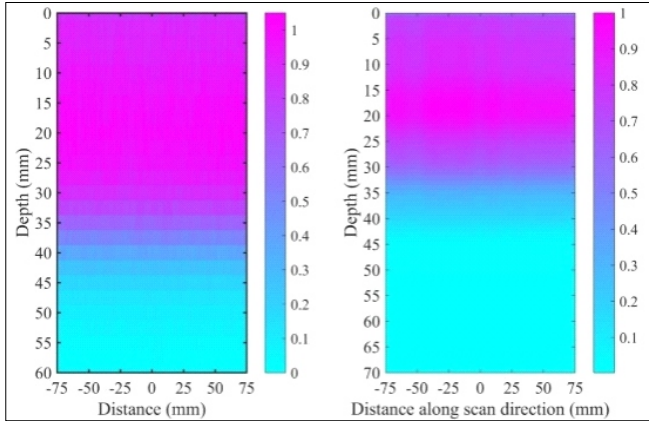


Fig.11: 2D-Dose plane along depth and beam scan direction for (a) 10 MeV Medical LINAC (b) 10 MeV EBC LINAC.

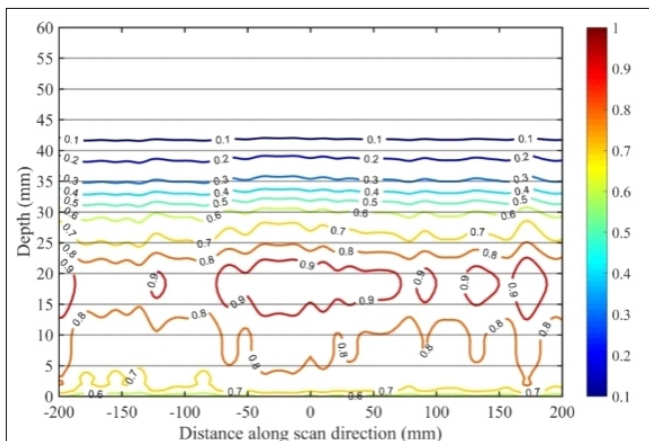


Fig.12: Isodose contour of 10 MeV EBC LINAC.

Isodose contours of measured dose drawn along depth and beam scan direction are shown in Fig.12. DUR= 2.3 is attained till approximately 3.3 cm of homogeneous solid water material.

Conclusion

Dose mapping in homogeneous material is used for operational qualification and that in routine product is necessary for performance qualification of an irradiation facility [2]. Determination of electron beam parameters like R_{50} , R_p , surface dose etc. are required to determine the geometry of product box to be irradiated. As per our study, the dosimetric characteristics of the electron beam in EBC facility matches

closer to that of 9 MeV beam of a medical LINAC. Accordingly, for this energy, for single-sided exposure of water equivalent materials, DUR = 2.3 value can be achieved by irradiating 3.3 cm of homogeneous water equivalent product/medium. For any other DUR limit, product thickness can be adjusted accordingly. For example, Up to 8 cm thick chili powder packets placed under 4 cm thermocol can be exposed from one side to be within the acceptable DUR limit of 2.3. For any other product, or heterogeneous material, case-specific detailed study is recommended to achieve the acceptable performance.

References

[1] International Atomic Energy Agency, 2002. Dosimetry for food irradiation. Technical reports series no, 409. IAEA, Vienna, 92-0-115502-6 IAEA TRS 409.

[2] International Atomic Energy Agency, 2015. Manual of good practice in food irradiation. Technical reports series no, 481. IAEA, Vienna, 978-92-0-105215-5 IAEA TRS 481.

[3] Food and Drug Administration official webpage <https://www.fda.gov/food/buy-store-serve-safe-food/food-irradiation-what-you-need-know>

[4] World Health Organization, 1997. High-dose irradiation: wholesomeness of food irradiated with doses above 10 kGy: report of a Joint FAO/IAEA/WHO study group. Technical Report Series 890, WHO, ISBN: 92-4-120890-2, WHO TRS 890.

[5] World Health Organization, 1988. A technique for preserving and improving the safety of food. ISBN 92 4 154240 3.

[6] Chilkulwar, R.H., et al., Dosimetric evaluation of an indigenously developed 10 MeV industrial electron beam irradiator. Radiation Measurements, 2012. 47 (2012) 628-633 <https://doi.org/10.1016/j.radmeas.2012.06.009>

[7] Chaudhary, Nishant and Sharma, Archana Sharma. Dosimetry characterizations and shielding aspects of high energy electron accelerators. Mumbai, India: Bhabha Atomic Research Centre BARC/2020/E/004 (2020)

[8] Dwivedi, Jishnu. Electron accelerator based radiation processing facility at Indore. RRCAT Newsletter. 2019. Vol 32 Issue 2 2019 (2) <https://www.rrcat.gov.in/newsletter/NL/nl2019/issue2/pdf/T1.pdf>

[9] BARC official website https://www.barc.gov.in/div/78_312_f138_105.pdf

[10] International Organization for Standardization, 2015. Standard practice for dosimetry in an electron beam facility for radiation processing at energies between 300 keV and 25 MeV. ISO/ASTM 51649:2015 (E).

[11] GEX Corporation official website https://www.gexcorp.com/pdf/2013%20Product%20Spec_B3%20Products.pdf

[12] International Commission on Radiation Units and Measurements, 1985. Radiation dosimetry: Electron beams with energies between 1 and 50 MeV. ICRU Report No. 35. <https://doi.org/10.1118/1.595780>

Bioceramics for Healthcare Applications

2

Wet Chemical Synthesis of Hydroxyapatite Powder and Estimation of Curcumin and Berberine Drug Loading Efficacy

Prabha Soundharraj¹, Sunita Kedia^{*1,2}, Goutam Chakraborty^{1,2}, Arati Magar¹ and J. Padma Nilaya^{1,2}

¹Laser & Plasma Technology Division, Bhabha Atomic Research Centre, Trombay – 400085, INDIA

²Homi Bhabha National Institute, Anushaktinagar, Mumbai – 400094, INDIA



Schematic representation of HAP powder synthesized by precipitation method

ABSTRACT

Hydroxyapatite (HAP) mineral constitutes ~70% of human bone. Therefore, synthetic HAP holds a prominent place in the context of orthopaedics. Synthetic HAP can act as a carrier to overcome the limitations of hydrophobicity and poor absorption associated with some common anticancer drugs. In the present work, HAP powder was synthesized by facile chemical precipitation method followed by structural characterizations. Furthermore, the potential of HAP powder as a carrier of antitumor drugs such as curcumin and berberine through physical adsorption using absorption measurements has been studied. The synthesised HAP powder has been found to have a higher loading efficacy of ~77% towards curcumin drug as compared to berberine (27%).

KEYWORDS: Hydroxyapatite (HAP), Raman spectrum

Introduction

Bioceramics such as hydroxyapatite (HAP), β -tricalcium phosphate and biphasic calcium phosphates possess high biocompatibility, chemical stability, and mechanical strength *in-vivo* [1]. Among these, HAP ($\text{Ca}_{10}(\text{PO}_4)_6(\text{OH})_2$), is an osteoconductive bioactive ceramic possessing a structural and chemical similarity with bones. The constituent elements of HAP are primarily calcium and phosphorus, with a stoichiometric Ca/P ratio of ~1.667. Synthetic HAP can be made by various chemical methods such as, precipitation, hydrothermal, hydrolysis, mechanochemical and sol-gel method [2]. Among these, the wet chemical precipitation technique is more popular due to its inherent simplicity and cost effectiveness. With hexagonal crystal structure, HAP has negatively charged phosphate anions (PO_4^{3-}) at both the ends and positively charged calcium (Ca^{2+}) cation on the sides along with surface ions such as OH. All these act as potential binding sites for biomolecules [3]. The similarity in composition with bone is the reason for the usage of HAP in many interesting applications such as bioimplants due to its superior osseointegration and as carrier to deliver several anti-inflammatory drugs, tumour drugs, proteins, antibiotics, and growth factors [4].

Curcumin, a yellow pigment that is derived from the rhizomes of *Curcuma longa* (turmeric) acts as a bioactive agent and is used to treat diabetes, cancer, arthritis and neurological diseases. Researchers are also examining its therapeutic effect towards inhibition of cancer cells and notably it has been used successfully for the treatment of breast cancer [5]. However, it has a limited use in biomedical applications due to its hydrophobicity and poor absorption. Berberine, another drug, found in the rhizome of the barberry plant is also known for its anti-fungal, anti-viral and anti-bacterial properties. It also

works against cancer, inflammation, hypertension and diabetes [6]. The poor water solubility, strong bitter taste and low absorption in the body of this drug restricts its therapeutic applications. To overcome such situations, engineering a suitable carrier to load these drugs and ensure their release can be beneficial.

The purpose of the present study is to synthesize in-house hydroxyapatite powder to load anticancer drugs such as curcumin and berberine and compare their loading efficacy. The powder was synthesized via wet chemical precipitation method using calcium nitrate tetra hydrate, orthophosphoric acid as a precursor. The powder so obtained was characterized by Scanning Electron Microscope (SEM), Energy dispersed X-ray spectroscopy (EDS), micro-Raman and X-ray diffraction (XRD) techniques. The drug loading efficacy was estimated over regular intervals up to 72 h by monitoring the absorbance using a spectrophotometer. A systematic decrease in the absorbance of the HAP-curcumin and HAP-berberine in the solution with increasing time indicated continuous loading of drug onto HAP powder. A loading efficiency of 77% and 27% was estimated for curcumin and berberine, respectively. In previous such studies [7, 8], the surface modification of synthesised HAP rendered it suitable to be used as carrier which also increased the drug loading efficacy. But in the present work, our studies have revealed that HAP powder without any surface modification is also capable to enhance the drug uptake.

Experimental Section

Chemicals and reagents

Calcium nitrate tetrahydrate [$\text{Ca}(\text{NO}_3)_2 \cdot 4\text{H}_2\text{O}$, 99%], orthophosphoric acid (H_3PO_4), ammonium hydroxide [NH_4OH , 28%], berberine and curcumin were procured from Sigma Aldrich. During synthesis, deionized water (DI) from a Millipore system was used as solvent.

*Author for Correspondence: Sunita Kedia
E-mail: skedia@barc.gov.in

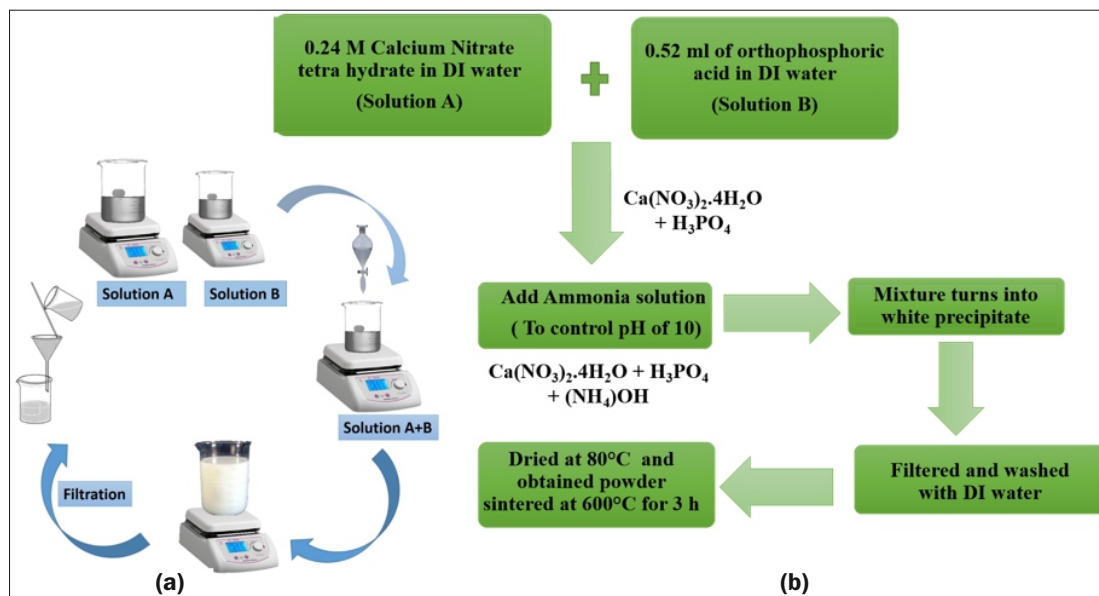


Fig.1: (a) Schematic representation of HAP powder synthesized by precipitation method and (b) flow chart of method of synthesis.

Preparation of HAP powder

HAP powder was synthesized by wet chemical precipitation method [9]. For this, about 0.24 M of $\text{Ca}(\text{NO}_3)_2 \cdot 4\text{H}_2\text{O}$ and 0.5 mL of H_3PO_4 were mixed in 25 mL of deionized water at room temperature in two separate beakers (Solution A and Solution B in Fig.1a). Both solutions were mixed and stirred for 30 minutes followed by dropwise addition of ammonia to maintain pH of the mixture at 10. The reaction was allowed to carry on along with continuous stirring for 2h. After the reaction, the precipitate was removed from the reaction solution by filtration and washed thrice with DI-water, as shown in Fig.1a. Then, it was dried at 80°C in an oven overnight and sintered at 600°C for 3 h to form a powder of HAP. A systematic flowchart of this reaction is shown in Fig.1b.

Characterization techniques

To identify the existence of functional groups in HAP powder, Raman spectrum was recorded (micro-Raman spectrophotometer, M/s. AIRIX Corp., Japan). The presence of crystallographic phases in the sintered HAP was estimated from XRD pattern using Cu K_α radiation ($\lambda = 1.5406 \text{ \AA}$). The XRD spectrum of the sample was compared with standard diffraction data (JCPDS # 09-0432) of pure HAP. The morphology and Ca/P ratio were studied by a scanning electron microscope (SEM, M/s. S&C, Korea) and Energy dispersive spectroscopy (EDS) respectively. For SEM analysis, the powder sample was dispersed in ethanol and spread over a carbon tape and dried at room temperature followed by gold sputtering. The drug loading efficacy was studied using UV-VIS spectrophotometer (Model No- UV 2700, Shimadzu

Corporation, Japan) in the range of 200-600 nm at absorption wavelengths of 264 nm and 347 nm for berberine and curcumin, respectively.

Encapsulation Efficiency (EE)

Fig.2a-c shows the absorption spectrum of HAP, curcumin and berberine at 1mM concentration dispersed in phosphate buffer saline (PBS, pH=7.4, 10X), respectively. PBS is a non-toxic solution used in many biological laboratories to prevent cell-rupturing or shrivelling up due to osmosis. Curcumin exhibits two distinct absorption peaks at 264 nm and 350 nm, the 264 nm being more prominent of the two. In the case of berberine, absorption occurred at 225 nm, 262 nm and 347 nm and prominent absorption was at 347 nm. Curcumin and berberine were added to HAP (dispersed in PBS) in the ratio of 1:1 separately and ultrasonicated for 30 min to ensure uniform dispersion of the drugs. Both solutions were kept undisturbed and drug loading was studied at regular intervals of 3h, 6h, 24h, 48h and 72h. For this, the solution was centrifuged at 12000 RPM for 15 min and supernatant solution was collected to record UV-VIS spectrophotometer absorption spectrum in the range of 200 to 600 nm. Centrifuging enabled settling down of the drug loaded HAP and unloaded HAP, leaving only the free drug in the solvent absorbance of which was measured.

The encapsulation efficiency (EE) was calculated using the following equation 1 [10].

$$\% \text{ EE} = \frac{C_T - C_F}{C_T} \times 100 \quad (1)$$

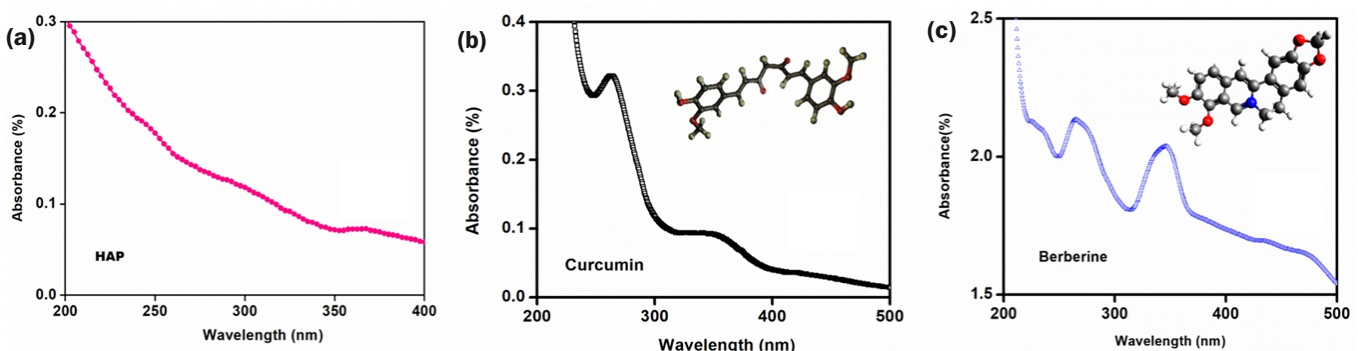


Fig.2: Absorbance spectrum of (a) HAP, (b) Curcumin and (c) Berberine.

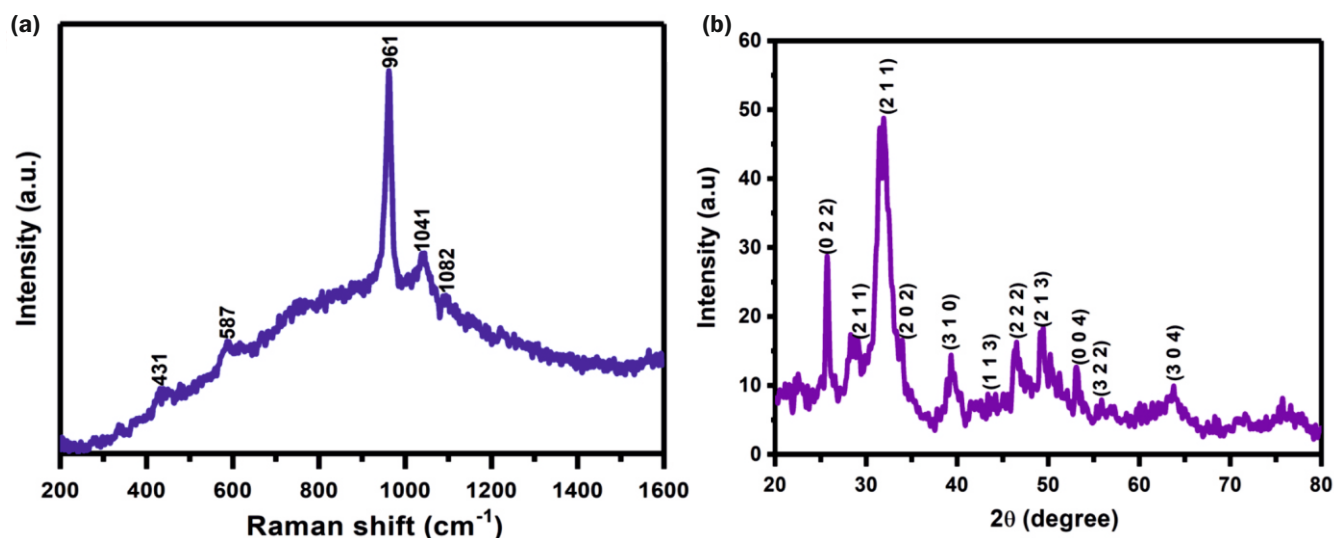


Fig.3: (a) Raman spectrum and (b) XRD pattern of synthesized HAP powder.

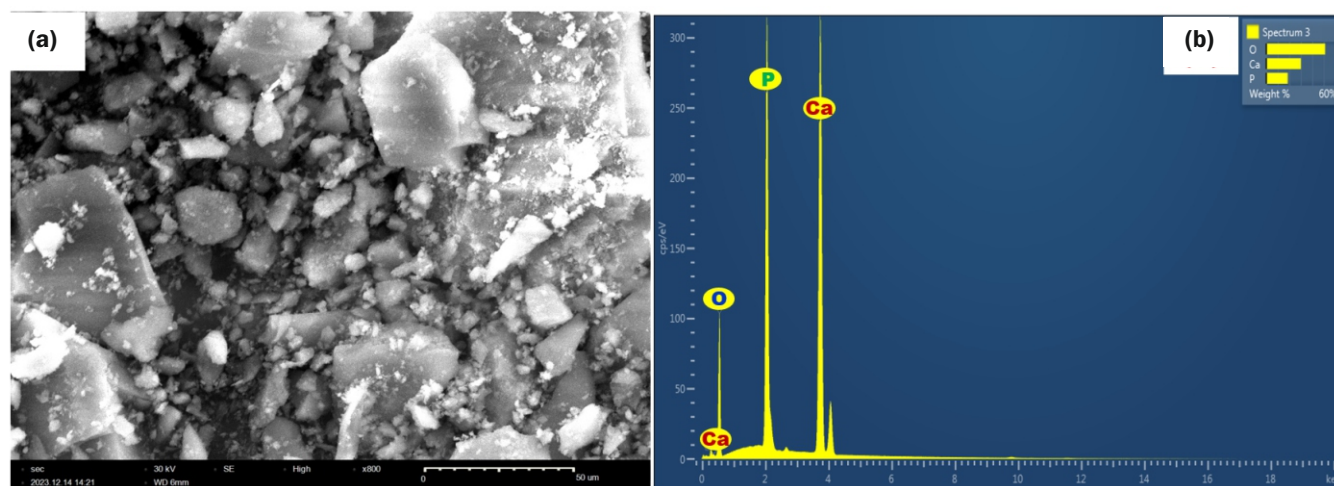


Fig.4: (a) SEM image (b) EDS spectrum of HAP powder.

Where C_T is the measured optical density corresponding to total concentration of curcumin/berberine (1 mM) added and C_F is the measured optical density corresponding to free curcumin/berberine present as supernatant after centrifugation at 12000 RPM.

Results and Discussion

Fig.3a shows the Raman spectrum of as synthesized HAP powder. The characteristic sharp Raman peak at 961 cm^{-1} is attributed to the symmetric stretching mode of $\text{PO}_4^{3-}(\nu_1)$ of HAP. The peaks at 431, 587, 1041 and 1082 cm^{-1} correspond to asymmetric bending mode of $\text{PO}_4^{3-}(\nu_2)$, asymmetric bending mode of $\text{PO}_4^{3-}(\nu_4)$, asymmetric stretching of $\text{PO}_4^{3-}(\nu_3)$ and asymmetric stretching of $\text{PO}_4^{3-}(\nu_3)$ respectively [11].

As seen in Fig.3b, the characteristic peak with highest intensity obtained at $2\theta=31.87^\circ$ corresponds to the (211) plane of HAP. Other peaks at $2\theta = 25.691, 28.284, 33.977, 39.383, 43.891, 46.544, 49.454, 52.941, 55.775,$ and 63.764 are due to diffraction from (002), (210), (202), (310), (113), (222), (213), (004), (322) and (304) planes of HAP respectively (JCPDS No: 09-0432) [12]. Presence of sharp, narrow and well-defined peaks in the diffraction pattern indicate highly crystalline nature of the synthesized HAP powder. All the diffraction peaks matched well with the standard diffraction data of apatite HAP and the planes of HAP powder reveal the expected hexagonal structure. Absence of

impurity peaks such as calcium phosphate and calcium hydroxide confirm the monophasic nature of the prepared HAP.

Fig.4a shows the SEM micrographs of HAP powder with agglomerated morphology. A large variation in particle size (10 to $100\text{ }\mu\text{m}$) was observed. EDS showed peaks corresponding to only Ca, P, and O. This too confirmed the absence of impurities in the synthesized powder. The average Ca/P ratio was measured as 1.60, which is very close to the theoretical Ca/P value of HAP (1.67) [2].

In Fig.5a, the dispersed colour of curcumin in PBS solution reduced with the increasing time as it loaded onto HAP. However, the colour of the liquid remains pale yellow at the end of 72h for berberine, indicating relatively lesser loading of this drug in the given time. The encapsulation efficiency (% EE) of curcumin and berberine conjugates by HAP powder was calculated using equation (1) on the basis of their optical densities at 264 nm and 347 nm respectively measured at 3h, 6h, 24h, 48h and 72h and plotted in Figure 5b and 5c. It can be noticed that from initial hours, the EE (%) of HAP was more for curcumin which remained high throughout the measurement. At the end of 72 hr the maximum EE (%) against curcumin and berberine were estimated as 77% and 27% respectively. In earlier reports, requirement of surface modifications of HAP before loading of curcumin (EE ~85%) [7] and berberine [12] was essential. However, here without any surface modification, we could observe a comparable value of 77% for curcumin

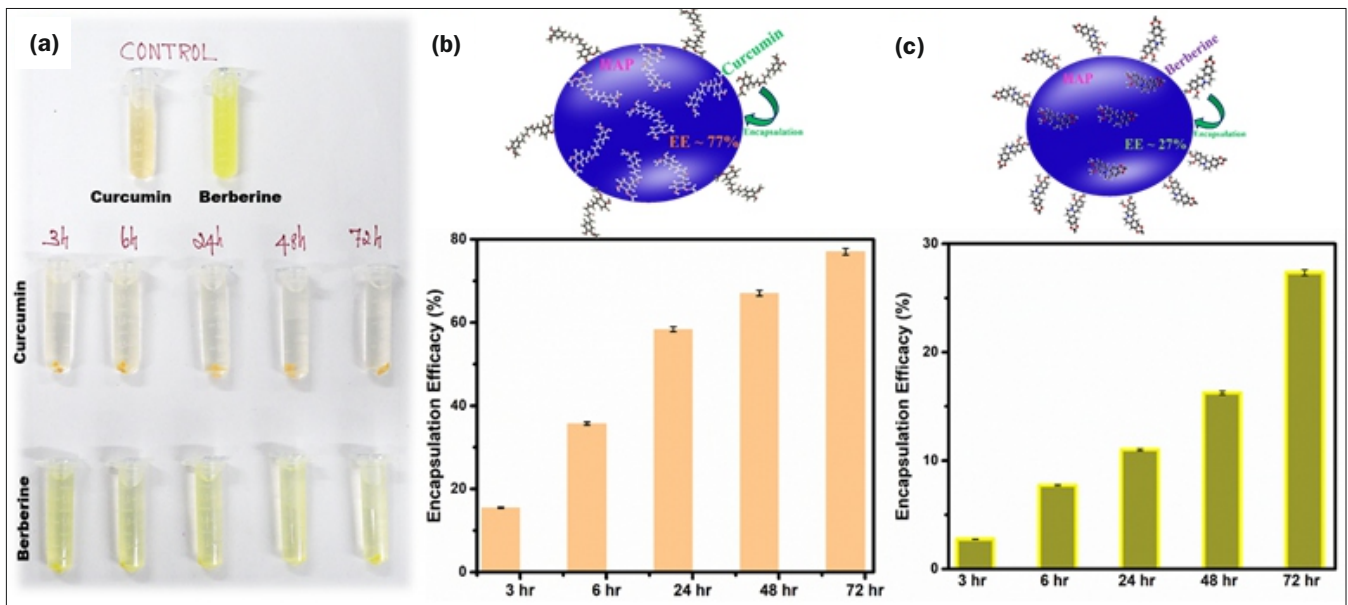


Fig.5: (a) Time dependent photograph of solution of HAP powder loaded with curcumin and berberine taken in Eppendorf tubes, Percentage encapsulation efficiency of HAP powder loaded with (b) curcumin, and (c) berberine.

loading. Hence, this approach of loading HAP with drug e.g., curcumin may be an effective method of its efficient transport and release in the intended region.

Conclusion

Quality of HAP powder synthesized by wet chemical technique was confirmed from the characteristics Raman and XRD peaks and from Ca/P ratio and was found to crystalline and pure with the required Ca/P ratio. Time dependent loading of curcumin and berberine drugs into HAP powder was monitored up to 72 hrs in PBS. The results showed that curcumin has a higher affinity towards the synthetic HAP prepared in this work with encapsulation efficiency about 77% as against 27 % for berberine. This study brings forth the possibility of using synthetic HAP under optimised conditions as an efficient carrier for drug loading applications.

Acknowledgement

Author would like to acknowledge valuable technical support from Nayna D. Jadhav, Laser & Plasma Technology Division (L&PTD), A.K. Sahu, Glass & Advanced Materials Division for EDS measurement, S.N. Achari, Chemistry Division for XRD measurement. They also are thankful to Head, L&PTD and Director, Beam Technology Development Group for their continued support and encouragement.

References

- [1] D. Xidaki, et.al., Synthesis of hydroxyapatite, β -tricalcium phosphate and biphasic calcium phosphate particles to act as local delivery carriers of curcumin: loading, release and in vitro studies, 11(4) (2018) 595.
- [2] A. Laska-Lesniewicz, et.al., 6-step manufacturing process of hydroxyapatite filler with specific properties applied for bone cement composites, 48(18) (2022) 26854-26864.
- [3] N. Safitri, et.al., Enhancing drug loading and release with hydroxyapatite nanoparticles for efficient drug delivery: A review synthesis methods, surface ion effects, and clinical prospects, (2023) 105092.
- [4] S. Lara-Ochoa, et.al., Hydroxyapatite nanoparticles in drug delivery: physicochemistry and applications, 13(10) (2021) 1642.
- [5] M. Iranshahy, et.al., Curcumin-loaded mesoporous silica nanoparticles for drug delivery: synthesis, biological assays and therapeutic potential—a review, 13(32) (2023) 22250-22267.
- [6] S. Khajavi, et.al., Design and synthesis of Berberine loaded Nano-hydroxyapatite/Gelatin Scaffold for bone cancer treatment, (2023).
- [7] K. Hemmati, et.al., In vitro evaluation of curcumin-loaded chitosan-coated hydroxyapatite nanocarriers as a potential system for effective treatment of cancer, 32(10) (2021) 1267-1287.
- [8] Mondal et al., Recent progress on fabrication and drug delivery applications of nanostructured hydroxyapatite, 10 (4) (2018) e1504.
- [9] A. Yelten-Yilmaz, et.al., Wet chemical precipitation synthesis of hydroxyapatite (HA) powders, 44(8) (2018) 9703-9710.
- [10] R.S. Fernandes, et.al., In vitro and in vivo effect of pH-sensitive PLGA-TPGS-based hybrid nanoparticles loaded with doxorubicin for breast cancer therapy, 14(11) (2022) 2394.
- [11] S. Sebastiammal, et.al., Curcumin-encased hydroxyapatite nanoparticles as novel biomaterials for antimicrobial, antioxidant and anticancer applications: A perspective of nano-based drug delivery, 57 (2020) 101752.
- [12] L. Chen, et.al., Berberine-Encapsulated Poly (lactic-co-glycolic acid)-Hydroxyapatite (PLGA/HA) Microspheres Synergistically Promote Bone Regeneration with DOPA-IGF-1 via the IGF-1R/PI3K/AKT/mTOR Pathway, 24(20) (2023) 15403.

Advanced Laser Technologies

3

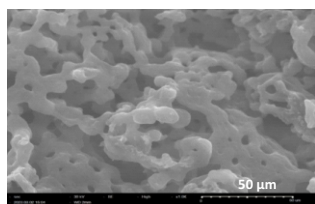
CW CO₂ Laser Induced Graphene on Biodegradable Surface

Tatsat Dwivedi^{1,2}, Hrithik Gupta³, Sunita Kedia^{1,2}, R. C. Das^{1,2} and J. Padma Nilaya*^{1,2}

¹Laser & Plasma Technology Division, Bhabha Atomic Research Centre, (BARC), Trombay-400085, INDIA

²Homi Bhabha National Institute, Anushakti Nagar, Mumbai-400094, INDIA

³Somaiya College, Mumbai University, Mumbai-423601, INDIA



SEM image of Coconut sample shell irradiated with CO₂ laser beam in 25 Watt and 0.9cm/sec .

ABSTRACT

Laser-induced graphenization of a surface of biodegradable substrate, viz. coconut shell, is reported. The setup involved a carbon dioxide (CO₂) laser, mechanical chopper, translation stage, and a detector for monitoring laser output power. Optimal laser fluence parameters and scan speeds were determined, which were at much variance with previous literature. Quality assessment of the graphene produced was performed using Raman spectroscopy. Scanning electron microscope images displayed varied LIG structures, including porous foam and fibrous bundles, based on the laser power employed. Additionally, XRD and sheet resistance measurements were conducted to evaluate the quality of the generated Laser-Induced Graphene (LIG).

KEYWORDS: Laser-Induced Graphene (LIG)

Introduction

Laser-Induced Graphene (LIG) is a versatile material used in various applications due to its exceptional properties [1,2,3,4]. It is created through a controlled, non-toxic laser irradiation process, offering advantages over the traditional chemical methods [3,4]. Any carbon precursor that can turn into amorphous carbon can be converted into graphene through laser irradiation. Amorphous carbon has a high absorption in the Infrared region and hence CO₂ laser, emitting at 10.6 μm is extensively used for this purpose. We present here the experimental results on the generation and parametric characterisation of LIG on coconut shell surface that contains high lignin content, employing an indigenous CO₂ laser system. Material properties were characterized using Raman spectroscopy, SEM, sheet resistance measurement, and XRD pattern. It is of interest to note that efficient LIG is reported here for laser parameters very different from those found in literature.

Experimental Work

The schematic diagram of the experimental set-up consisting of a in-house assembled CW-CO₂ laser operating with a gas mixture of CO₂:N₂: He :: 2:2:8 at a total pressure of ~12 mbar and capable of delivering ~80W in free running

mode is shown in Fig.1. The laser was pulsed by means of a mechanical chopper at 750 Hz giving a pulse duration of 650 μsec. The fluence was increased appropriately by focusing the beam using a 10 cm f lens resulting in a spot size of ~350μm. The laser power and the scanning speed were adjusted to optimise the LIG process.

The coconut shell sample substrates, cut to the size of ~1x1 cm² and surface polished, were mounted on a linear translational stage and placed at the focal point of the lens. They were irradiated at different laser powers spanning 5W to 40 W at three different scan speeds (0.18cm/sec, 0.36cm/sec, 0.90cm/sec). The change in the scan speed results in a change of laser pulse overlap, that in turn is responsible for altered rise in surface temperature and efficiency of graphenisation. These irradiated samples were first characterized with Raman spectrometer for confirmation of the formation of LIG. I_D/I_G ratios (described in next section) for all the samples were compared and samples having lowest I_D/I_G value for all scanning speeds were then characterized by SEM. The laser parameters and corresponding I_D/I_G ratios are shown in Table-1. Further information about graphene formed was obtained by XRD for the best LIG sample using Cu-Kα radiation (λ = 0.154 nm) in θ-2θ geometry.

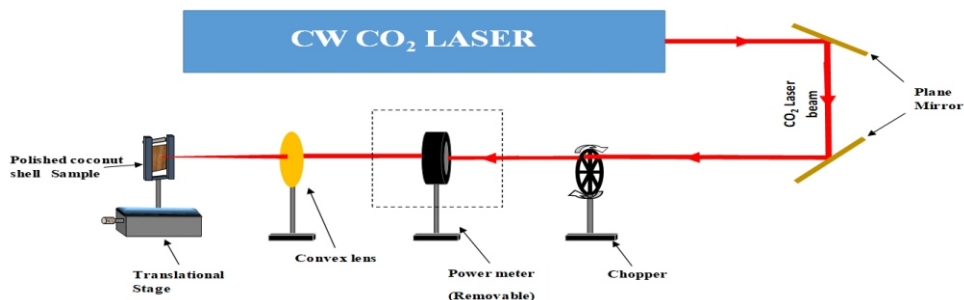


Fig.1: Schematic of Experimental set up for LIG generation using CW CO₂ laser.

*Author for Correspondence: J. Padma Nilaya
E-mail: jpnilaya@barc.gov.in

Table 1: Laser parameters and corresponding to I_D/I_G for three different scan speeds.

Scan speed	Overlapping Factor	Fluence (J/cm ²)	Power	I_D/I_G
0.9cm/s	96.45%	7.33	5	1.07
		14.66	10	1.02
		17.59	12	0.92
		21.99	15	0.83
		26.38	18	0.69
		29.32	20	0.63
		36.65	25	0.60
		43.98	30	0.75
		51.31	35	0.89
58.64	40	0.94		
0.36cm/s	98.57%	7.33	5	1.09
		14.66	10	0.80
		17.59	12	0.85
		21.99	15	0.87
		26.38	18	0.91
		29.32	20	0.91
		36.65	25	0.95
		43.98	30	0.96
		51.31	35	0.98
58.64	40	1.00		
0.18cm/s	99.28%	7.33	5	0.87
		14.66	10	0.89
		17.59	12	0.91
		21.99	15	0.91
		26.38	18	0.92

Results & Discussion

The micro Raman spectra shown in Fig.2 revealed three conspicuous peaks: D peak (~1350 cm⁻¹) indicating defects, G peak (~1580 cm⁻¹) representing crystallinity, and 2D peak (~2700 cm⁻¹) from second-order phonons. Lower I_D/I_G indicates higher crystallinity and fewer defects. Fig.2 depicts the spectra obtained for the laser power where lowest I_D/I_G values were obtained for the 3 scan speeds, viz., 0.60 for 0.90cm/s at 25 W, 0.8 for 0.36 cm/s at 10W and 0.87 for 0.18cm/s at 5W. It is to be noted that no LIG formation is seen for the laser power below 5 Watt. Thus we find that best graphene generation occurred for sample 25 Watt at

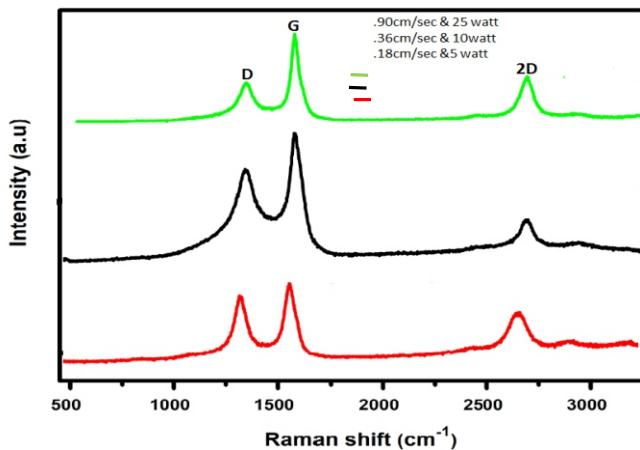


Fig.2: Raman spectra of coconut shell samples having lowest I_D/I_G for three scan speeds.

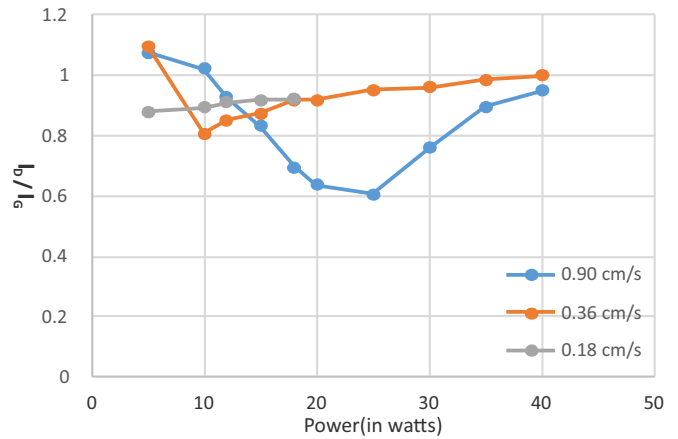


Fig.3: I_D/I_G Vs laser power.

0.90 cm/s scan speed. The ratio of I_D/I_G as a function of laser power for different scanning speeds is shown in Fig.3. It is also clear from this experiment that laser power has linear dependence on scan speed, which in accordance with the data available in literature [1]. The optimum rise in temperature required for formation of amorphous carbon that is converted into graphene by further exposure to laser pulse is governed by the laser power and duration of exposure. For a given scan speed, therefore, there exists an optimised laser power where the graphene conversion is maximum. At lower or higher incident powers these conditions are not efficiently met within the range of scan speeds employed here and hence result in poorer quality of the generated graphene. On similar lines, as the scan speed (exposure time of the substrate) increases, reduction in the exposure time of the sample surface to laser beam requires a proportionate increase in the laser power as observed experimentally. SEM images of best LIG samples for each scan speed are shown in Fig.4. For the case of low power (5Watt) the surface morphology is uniformly porous, with a structure like that of foam. This structure is known to be formed by the gas that is generated by the recombination of heteroatoms (Fig.4b). When the laser power reaches ~10Watt the fibrous clusters appear due to the overlapping domains of the adjacent scanning lines and this leads to the secondary carbonization and change of LIG structure, (Fig.4c)[5]. Most of the region remains still porous, although the size of pores are larger than those under 5Watt. When the laser power reaches to 25Watt, fiber bundles are formed and entangled with one another to form a network structure with the whole surface being covered (Fig.4d). The diameters of laser-induced fiber bundles under 25Watt are larger than those under 10Watt.

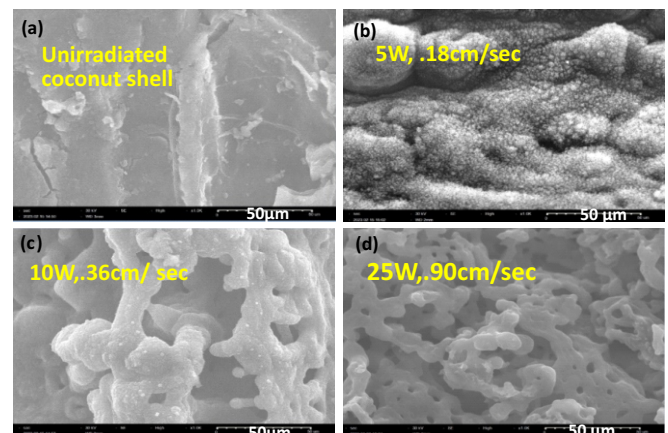


Fig.4: SEM image of Coconut sample shell irradiated with CO₂ laser beam (a) unirradiated coconut shell (b) 5 Watt and 0.18cm/sec, (c) 10 Watt and 0.36cm/sec and (d) 25 Watt and 0.9cm/sec.

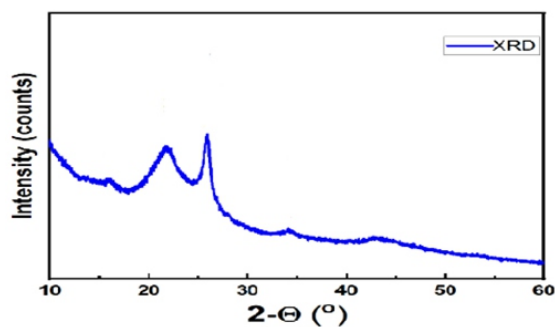


Fig.5: XRD of LIG generated from coconut shell at 25 Watt laser power & 0.90 cm/sec scan speed.

The XRD pattern of the sample irradiated with 25Watt laser power, at the scan speed of 0.9cm/s exhibited strong and sharp peaks at $\sim 2\theta = 26^\circ$ corresponding to the (002) reflection planes of graphite (Fig.5). This indicates high degree of graphitization. It is to be noted that the peak at nearly $\sim 2\theta = 22^\circ$ is characteristic of coconut surface as same peak is seen on unirradiated coconut sample's XRD pattern.

The sheet resistance of the lowest I_D/I_G sample (25W, 0.9cm/sec) was also measured using four probe set-up. The sheet resistance was found to be $\sim 4.6\Omega/\square$, implying high quality of graphene formed under these experimental conditions which differ widely from that reported in literature.

Conclusion

Laser-Induced Graphene (LIG) was created on the surface of coconut shell samples using a locally assembled CO₂ laser. The laser was fine tuned for fluence, pulse duration, and overlap factor. The optimal laser power for LIG formation

remained fairly consistent for a given scan speed but increased linearly as the scan speed increased. The best LIG formation with $I_D/I_G = 0.6$ and very low sheet resistance was achieved at 650 μ s, 750 Hz, 25W laser pulses and a 0.90 cm/second scan speed. These laser parameters differ from those reported in previous studies. As the laser power increased, the microstructure of the LIG changed from a porous structure to fibrous bundles. This unique combination of a porous graphene surface on biodegradable substrates makes it suitable for various electronic applications including super capacitors, RFID antennae, and sensors.

Acknowledgements

The authors acknowledge the help rendered by Dr. Shovit Bhattacharya Technical Physics division BARC for XRD and sheet resistance measurement related experiments. They also acknowledge the support and encouragement extended by Head, Laser and Plasma Technology Division, BARC and Director, Beam Technology Development Group, BARC.

References

- [1] Lin J. , Peng, Z., Liu Y., Ruiz-Zepeda, F., Ye. R., Samuel, E.L., Yacaman M.J., Yakobson B.I., Tour J.M., Nat. Commun. 5, 5714. (2014).
- [2] Peng Z. ,Lin, J., Ye, R., Samuel, E.L., Tour J.M., ACS Appl. Mater. Inter. 7 3414–3419 (2015).
- [3] Stanford M.G., Yang K., Chyan Y., Kittrell C., Tour J.M. ACS Nano, 13 3474–3482 (2019).
- [4] Chhetry A., Sharifuzzaman M., Yoon H., Sharma S., Park J.Y ACS Appl. Mater. Inter. 11 22531–22542 (2019).
- [5] Liu M, Wu J N, Cheng H Y Sci China Tech Sci 65 41–52 (2022).

Cold Plasma Applications

1

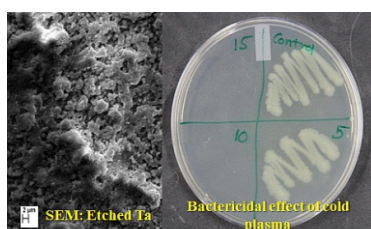
Indigenous Development of Cold Atmospheric Pressure Plasma Device for Multipurpose Applications

Rajib Kar^{*1,2}, Vishakha Bende², Vandan Nagar^{2,3}, Vanita Sekar¹, and Namita Maiti^{1,2}

¹Laser & Plasma Technology Division, Bhabha Atomic Research Centre, (BARC), Trombay-400085, INDIA

²Homi Bhabha National Institute, Anushaktinagar, Mumbai-400094, INDIA

³Food Technology Division, Bhabha Atomic Research Centre (BARC), Trombay-400085, INDIA



SEM image of plasma etched Ta substrate and some of the results of bactericidal study from developed cold plasma device

ABSTRACT

Cold atmospheric pressure plasma (CAPP) technology is gaining attention for/ due to its low cost, simplicity, and ability to create active species. It shows promise for coating, etching, surface treatment and medical applications. In the present study, we have used an indigenously designed 10 MHz atmospheric pressure plasma jet based on Tesla coil principle. The designed device was then applied for the chemical etching as well as bacterial inactivation to show its multipurpose efficacy. Our observations revealed that the device can manage complex molecular plasma gases such as CF_4 and O_2 . Effective bactericidal effects can be achieved with the device operating at power levels as low as approximately 20 watts, while efficient etching can be obtained when the device operates at around 80 watts of power.

KEYWORDS: Cold plasma, Tesla coil, Etching, Bactericidal effects

Introduction

Cold atmospheric pressure plasma (CAPP) has become a versatile tool with applications ranging from material processing to plasma medicine [1]. In recent years, there has been a significant surge in the research focused on atmospheric pressure cold plasma device [2, 3]. These devices offer the advantage of eliminating the need for expensive and bulky vacuum equipments [4]. Moreover, due to its low gas temperatures and generated reactive species, such type of plasma source finds versatile applications, ranging from industry to biology [5,6]. Atmospheric pressure cold plasma etching has found diverse applications in various industries. In the microelectronics sector, it is employed for the precise and high-resolution etching of semiconductor materials, enabling the production of smaller and more efficient electronic devices. In the automotive industry, it plays a role in improving adhesive bonding and surface treatments, enhancing the durability and performance of the components [7,8]. The medical field benefits from its ability to sterilize medical instruments, ensuring patient safety [9]. In packaging, it aids in surface activation for the improved adhesion of inks and coatings. Furthermore, its eco-friendly attributes align with sustainability goals, making atmospheric pressure cold plasma etching an increasingly valuable tool in modern industrial processes.

Materials and Methods

We have developed an innovative Tesla coil-based device entirely through indigenous efforts. Fig.1(a) illustrates the device's design concept, which comprises three key blocks. The first block involves an input DC source responsible for

powering the second block. This second block primarily consists of a MOSFET, a tank circuit, and protective elements. It is linked to a third block, featuring an air-cored coil serving as a Tesla coil. At the output of the second coil, we have a stainless steel electrode where the plasma discharge occurs. Our primary objectives are to optimize power transfer from the second to the third block and establish a resonance between them. To generate cold plasma, the output voltage V_2 must reach a sufficiently high level (several kilovolts). In our specific setup, the circuit operates at approximately 10 MHz, and we have introduced additional resistances strategically in the circuit. This well-engineered device is highly capable of producing uniform and exceptionally stable plasma.

The actual photograph of the operational device is shown in Fig.1(b), and Fig.1(c) shows the close-up view of the developed device during etching experiment. Fig.1(d) shows the dimensions of the different components of the complete CAPP set-up.

The effectiveness of this device was investigated for chemical etching of Ta substrate. A complex plasma with combination of Ar, CF_4 and O_2 was generated for this purpose. CF_4 is the primary etchant gas as it is expected to generate F after dissociation inside plasma to facilitate etching i.e. loss of material from bulk and O_2 is known to enhance the process of etching [8]. During experiment, a flow rate of Ar (8 LPM) and O_2 (100 SCCM) was kept fixed and CF_4 gas flow rate was varied from 0 to 750 SCCM. The etching rate completely depends on the efficient dissociation of Cf_4 into volatile F/F_2 . During experiment, operating power was kept constant around ~ 80 watts. Ar gas flow was kept 8 LPM during the experiments for 30 minutes. The etching rate has been measured for each experiment by weighing Ta before (w_1) and after (w_2) in a micro-balance for the given time period (t).

*Author for Correspondence: Rajib Kar
E-mail: rajibkar@barc.gov.in

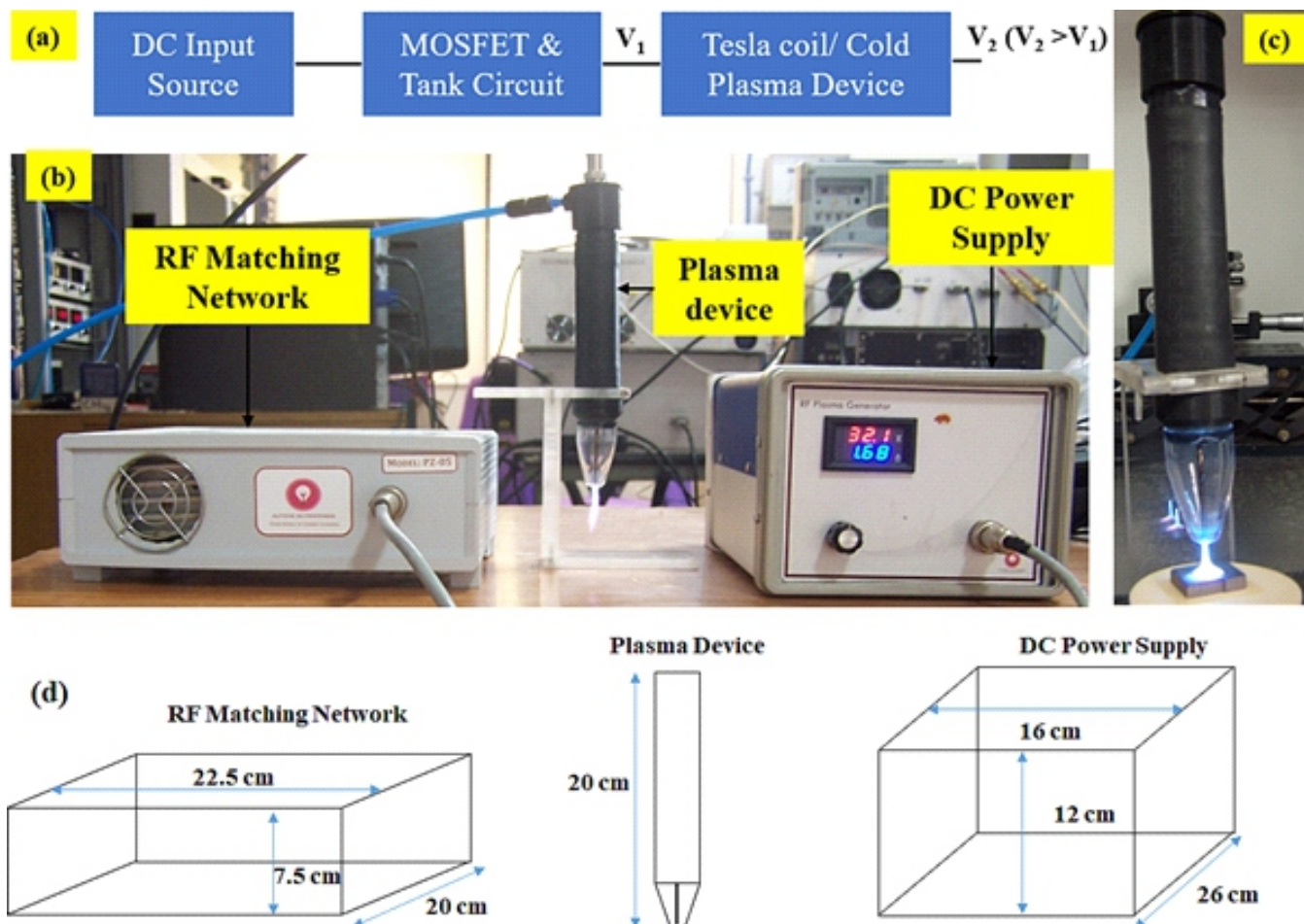


Fig.1: (a) A detailed block diagram of the CAPP device (b) The actual photograph of CAPP device, (c) close-up view of the device during etching experiment, (d) Dimensions of different components of the set-up.

$$\text{Etching rate} = \frac{w_1 - w_2}{t} \text{ (mg/min)}$$

Apart from etching, the efficacy of the device was also tested for bacterial inactivation. Two representative bacteria: *Staphylococcus aureus* (*S. aureus* ATCC 9144, Gram positive) and *Escherichia coli* (*E. coli* ATCC 700926, Gram negative) were used for this purpose. During experiment, 8 LPM Ar flow was kept fixed at an operating power ~ 20 watts. Experiments were conducted for 5 to 30 seconds with 5 sec interval. Separate control was kept in both cases. Both bacterial cultures were separately grown in 25 ml tryptic soya broth (TSB) at 37°C, 150 rpm overnight. Plasma treatment was carried out directly on the grown culture. A control sample containing untreated bacteria was also streaked on the agar plate. Following the experiment, agar plates were incubated at 37°C for 24 h and then checked visually for colony formation.

Result

Fig.2(a) shows photograph of Ta substrates before and after etching while Fig.2(b) shows the SEM image of these substrates. Post plasma etching, significant changes have been seen in the micrograph as machining marks have been changed into pits and voids. Fig.2(c) shows graphical representation of the study where it is seen that etching rate increases almost linearly with increasing CF₄ value which means with the increase of CF₄, enhanced generation of nascent fluorine helps to increase the etching rate. With the increase of CF₄ in the plasma, plasma plume length start

reducing slightly with each increasing step. As other parameters including the applied power is kept constant, now more energy of plasma was being used in dissociation of molecular CF₄ and eventually beyond 750 SCCM of CF₄ flow rate, the plasma could not be stabilized and it ceased to exist. There was not any significant change in the heat flux from plasma during this experiment. Inset photograph in Fig.2(c) depicts successful detection of F₂. Roughness of the etched and unetched area was measured using a white light source Solarius 3D optical profilometer. The result is presented in tabular form within Fig.2(c). It is seen that controlled etching has improved the roughness of the sample. As received Ta sample showed variation in roughness values as expected due to presence of machining marks.

Fig.3(a) shows the result of the bacterial inactivation experiment. It is seen that exposure of mere 10 seconds is enough to destroy both the bacteria when plasma is in contact with the bacteria. Fig.3(b) shows optical emission spectrum (OES) from the plasma. The spectrum shows presence of bactericidal OH and N₂ (SPS) emission bands in UV range. Presence of these two bands helps in effective destruction of bacteria along with energetic charged species and radicals present in cold plasma. It is important to note that, *S. aureus* and *E. coli* have thermal death point above ~ 60°C and hence cold plasma must have temperature lesser than this value to ensure plasma dominated effects. Fig.3(c) shows the set-up used for temperature measurement of a floating substrate. Here, a stainless-steel disc was kept in contact with plasma in floating condition allowing only radiation loss. Since, maximum

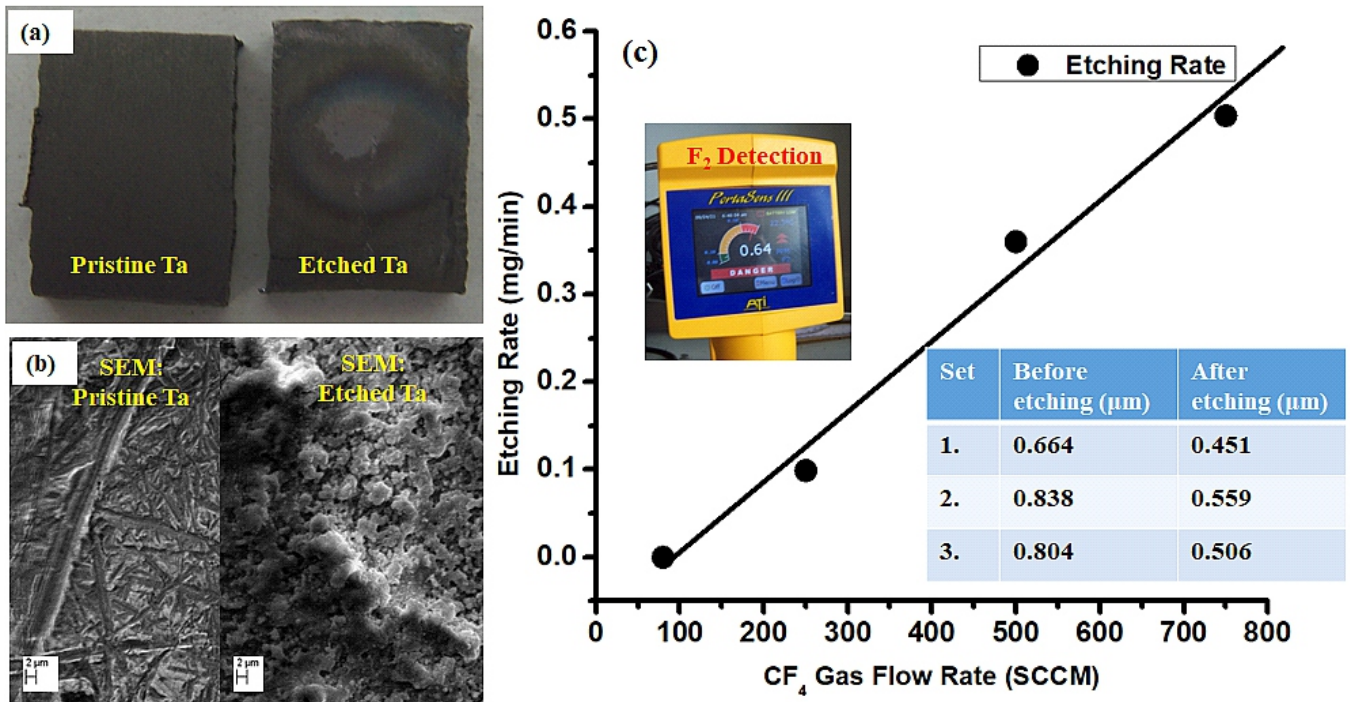


Fig.2: (a) Photograph & (b) SEM image of pristine & plasma etched Ta substrate, (c) Graphical representation of etching rate vs. CF₄ gas flow rate, inset photograph of F₂ detection. Table in the inset shows improvement in roughness post plasma etching.

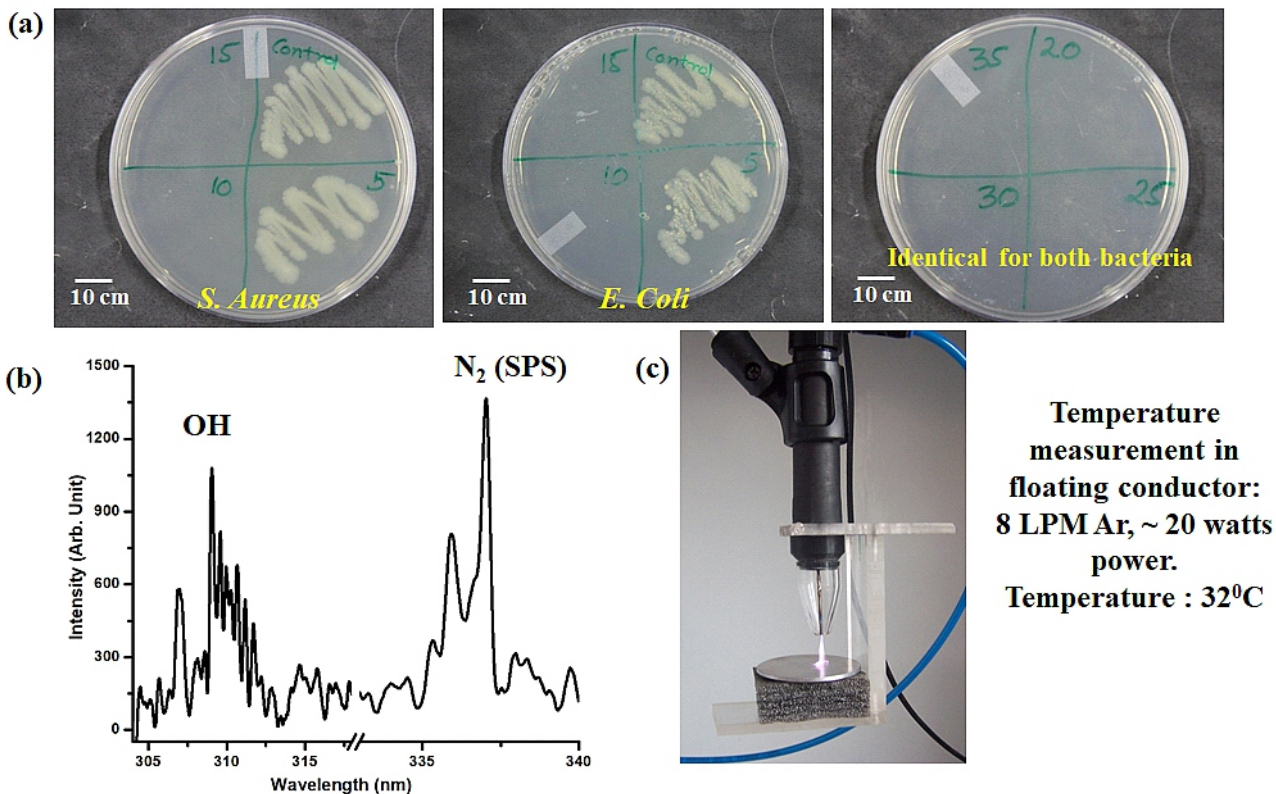


Fig.3: (a) Result of bactericidal study from developed cold plasma device, (b) OES spectrum of the plasma showing presence of OH and N₂ (SPS) bands, (c) set-up for temperature measurement of a substrate.

bacteria treatment time was 30 secs. The disc was kept in this condition for 1 minute and temperature was measured with IR thermometer which turned out to be 31°C.

Conclusion

This study shows development of an indigenous Tesla coil based 10 MHz plasma source which can be used in multipurpose applications. Two examples have been tested in the form of plasma etching and bacterial inactivation in the present case. It is seen that the device is capable of handling

complex molecular plasma gas in the form of CF₄ and O₂. The device can be operated as low as ~ 20 watts for effective bactericidal effect and efficient etching can be obtained from the device at ~ 80 watts power.

Acknowledgements

The authors gratefully acknowledge constant support and guidance of Head, Laser & Plasma Technology Division and of Group Director, Beam Technology Development Group.

References

- [1] Laroussi, Mounir. 2019. "1995–2005: A Decade of Innovation in Low Temperature Plasma and Its Applications" *Plasma* 2, no. 3: 360-368.
- [2] A. Schutze, J.Y. Jeong, S. E. Babayan, J. Park, Gary S. Selwyn, and R.F. Hicks. (1998). the atmospheric-pressure plasma jet: a review and comparison to other plasma sources. *IEEE Transactions on Plasma Science*, 26(6), 1685 – 1694.
- [3] T.H. Sasmazel , M. Alazzawi, Kadim Abid Alsaheb N, (2021) Atmospheric pressure plasma surface treatment of polymers and influence on cell cultivation *Molecule*, 26(6), 1665.
- [4] Bardos, Ladislav & Barankova, Hana. (2008). Plasma processes at atmospheric and low pressures. *Vacuum*. 83. 522-527. 10.1016/j.vacuum.2008.04.063.
- [5] Yilma B.B, Luebben J.F, Nalankilli G. (2020). Cold plasma treatment in wet chemical textile processing. *Fibres & Textiles Eastern Europe*, 28(6), 118-126.
- [6] M. Iaroussi. (2020). Cold plasma in medicine and healthcare the new frontier in low temperature plasma applications. *Frontiers in Physics*, 8, 74.
- [7] Chun, Inwoo & Efremov, Alexander & Yeom, Geun & Kwon, Kwang-Ho. (2015). A comparative study of $CF_4/O_2/Ar$ and $C_4F_8/O_2/Ar$ plasmas for dry etching applications. *Thin Solid Films*. 579, 136-143.
- [8] R. Kar, A. Bute, N. Chand, Z. Ahmed, N. Maiti, and D. S. Patil. (2020) Removal of Radioactive Waste by Non-thermal Plasma Etching: Trends for the Promising Future. In: Hussain, C. (eds) *Handbook of Environmental Materials Management*. Springer, Cham.
- [9] R. Kar, N. Chand, A. Bute, Namita Maiti, A. V. S. S. Narayan Rao, V. Nagar, R. Shashidhar, D. S. Patil, S. K. Ghosh, A. Sharma (2020) Cold Plasma: Clean Technology to Destroy Pathogenic Micro-organisms, *Transactions of the Indian National Academy of Engineering*, 5, 327-331.

High Power Pulsed Laser

5

Optical Power Enhancement of High Repetition Rate Copper Vapor Laser MOPA Chains

Anil S. Nayak*, Rajasree Vijayan, Dheeraj Singh, S. Mandal, B. V. Gangwane and V. S. Rawat

Advanced Tunable Laser Applications Division, Bhabha Atomic Research Centre, Trombay – 400085, INDIA



Typical Copper Vapor Laser with High voltage pulse power supply

ABSTRACT

Copper Vapor Laser (CVL) is a high power pulsed laser system with high repetition rate. The laser source is in the visible spectrum (510 & 578 nm) of electromagnetic radiation. One of the important applications is laser based Fortification of stable isotopes for generation of radionuclide to be used in Medical Applications (Lu, Yb, Sm) for cancer therapy. CVL acts as a pump source for precisely tunable narrow band dye lasers. This paper describes methodology to increase the optical power of the individual CVL, thereby increasing the power output from the CVLs configured in Master Oscillator Power Amplifier (MOPA) configuration. The power enhancement is attained by increasing the energy storage capacitance in the DC resonant charging circuit at the primary of the pulse transformer. This paper depicts the optical power enhancement of individual system as well as output from CVL MOPA chain and its long duration optical power stability. The effect of these modifications on the charging time, charge transfer time, propagation delay and voltage amplification at the secondary of the pulse transformer is aptly described in this paper.

KEYWORDS: Copper Vapor Laser, Storage capacitor, Pulse Transformer, MOPA, Magnetic Pulse Compression

Introduction

There has been ever increasing demand for radiopharmaceuticals like Lu-177 and Sm-153 for cancer therapy, bone pain palliation and synovectomy. Selective ionization of the desired isotope using laser beams of narrow linewidth, high repetition rate, and high intensity followed by collection of photo ions of desired isotopes using electromagnetic fields is used for this process. Dye lasers are most apt selection for purification process as they meet the requirements of wavelength tunability, high average power (few tens of Watt) and high repetition rates (few tens of kHz). The tunable dye lasers are optically pumped by the fixed wavelength laser systems such as CVL and diode pumped solid state lasers (DPSSL). The CVL MOPA chains with high average power are used as the pumping source for the generation of the tunable dye lasers. The high average power pump source is necessary for generating high average power dye lasers. This high average power is generated by the CVL MOPA chain. Hence, dye laser energy per pulse increases with increase in the energy per pulse of the CVL pump source.

The CVL is pumped by the pulsed electric discharge of suitable rise time [1]. The electrical excitation of the CVL takes place at pulsed voltage of 10–15kV at 9 kHz pulse repetition frequency [2,3]. This pulsed laser source provides laser wavelengths at 510 nm (green) and 578 nm (yellow) in the visible region of the electromagnetic spectrum. Scalability of optical power is one of the important features of CVLs; which can be achieved by synchronized optical temporal pulses and spatially overlapped laser beam in each amplifier module. In MOPA configuration, the oscillator provides a good quality seed

laser pulse which is further amplified using five consecutive CVL amplifier modules to extract maximum optical output power. The oscillator and the amplifiers are operated in 9 kHz pulse repetition frequency [4,5]. In order to further enhance the MOPA power efficiently, the power of the individual CVLs can be increased which is being described in this article.

System Description

The electrical excitation system of the CVL consists of a variable DC Switched Mode Power Supply (SMPS), and Pulse Generator Unit (PGU). The PGU consists of pulse forming network, pulse transformer and three MPC stage for generation high voltage pulse with fast rise time. The PGU provides 10–15kV of peak pulsed voltage of 70–90ns rise time [6,7]. The high voltage ensures breakdown in between the high voltage electrodes of the laser head. The laser head with water cooled electrodes placed at the end of cylindrical alumina tube of inner diameter 38mm and the length 1800 mm, which is encapsulated with alumina wool to provide thermal insulation so that the operating temperature inside alumina tube is maintained at ~1500°C. High purity neon gas is used as a buffer gas which provides electrical discharge and results in the collision between the electrons and the neon atoms to raise the temperature of the alumina tube. The solid copper pellets are evenly distributed along the length inside the alumina tube start and copper vapors are generated. The atomic transitions of copper provide the gain to fulfill lasing action under unstable resonator cavity configuration in the oscillator. The sharp rise time in the range of 70–90ns of the high voltage pulse ensures sufficient population inversion which is essential requirement for lasing action in the CVL [4,5]. The photograph of typical CVL system is shown in Fig.1.

*Author for Correspondence: Anil S. Nayak
E-mail: anilnsn@barc.gov.in

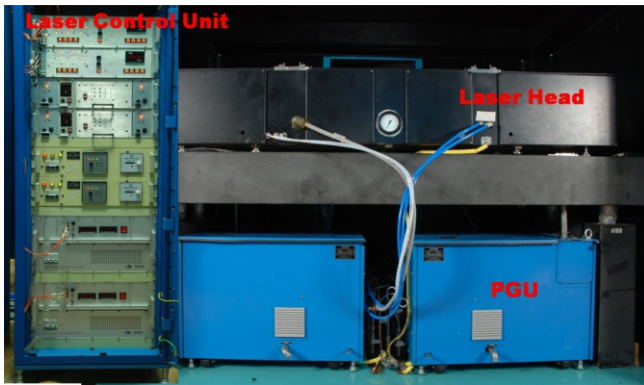


Fig.1: Typical Copper Vapor Laser with High voltage pulse power supply.

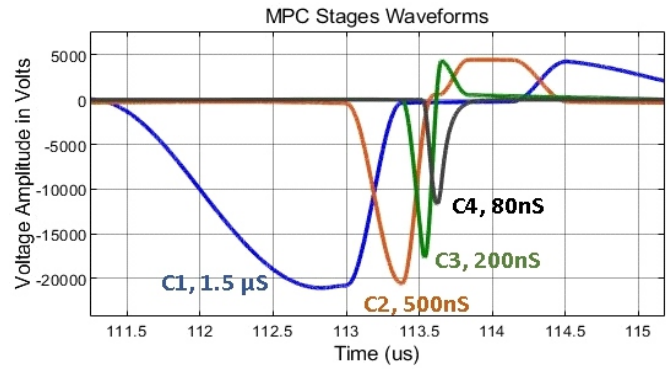


Fig.3: The Typical high voltage waveforms across the capacitors inside the PGU.

The PGU schematic is shown in Fig.2. The pulsed power source consists of High voltage SMPS (450 V and 25 A) is used to store the energy in the storage capacitor (Cs). The main energy storage capacitor Cs is charged approximately to double the SMPS voltage using resonant charging circuit. The resonant charging circuit includes the inductor of 150 μH and the main energy storage capacitor (Cs) of 1.98 μF. The IGBT switch SW-1 initiates the charging of the capacitor. Once the capacitor is completely charged in 54 μs (charging time = $\pi\sqrt{LC}$), the main discharge IGBT switch SW-2 closes thereby transferring the energy to the secondary side of 1:32 pulse transformer [8,9].

The rise time of the high voltage pulse appearing at the secondary of the pulse transformer is given by $\pi\sqrt{LC}$, where L=leakage inductance of the pulse transformer (0.22 μH) and C is the series combination of the primary storage capacitor (1.98 μF) and secondary capacitor C-1 referred to the primary ($2\text{ nF} \times 32^2 = 2.048\ \mu\text{F}$). Hence the rise time of the secondary voltage pulse is 1.48 μs. This high voltage pulse traverses through the three stage Magnetic Pulse compression (MPC) circuit. The high voltage pulse is compressed to 500 ns, 200 ns and 80 ns at the end of first, second and third stage respectively [6,7]. Thus the compression ratio is designed approximately to be in the range of 3, 2.5, 2.5. hence the rise time of the pulse is compressed to approximately 18.75 times the value at the secondary of pulse transformer. The

typical waveforms obtained at different capacitors in the PGU are shown in Fig.3.

The voltage pulse of 10–15 kV and rise time around 80 ns is applied to the laser head. The IGBT switch SW-3 is used for dissipating the residual energy on the storage capacitor before the arrival of next pulse. This command charging circuit helps in reducing jitter. The timing sequence of the command charging IGBTs i.e. SW-1 and SW-3 and main discharge IGBT SW-2 is generated by the IGBT gate driver circuit which includes the timer card, IGBT Driver and Booster cards.

Average current in the primary circuit: The Impedance of the resonant charging circuit comprising of the Inductor ($L=150\ \mu\text{H}$) and Capacitor ($C=1.98\ \mu\text{F}$) is given by,

$$Z_{pn} = \sqrt{L/C} = 8.7\ \Omega$$

The peak primary current (I_m) is given by,

$$I_m = V_o / Z_{pn} = 44.82\ \text{A},$$

where V_o is the operating SMPS Voltage viz. 390 V

The average primary current is given by,

$$I_{avg} = 2x(I_m / \pi) \times \text{Duty cycle} = 13.9\ \text{A},$$

Where duty cycle is the ratio of the time required by the capacitor to fully charge to the total time period between the consecutive pulses.

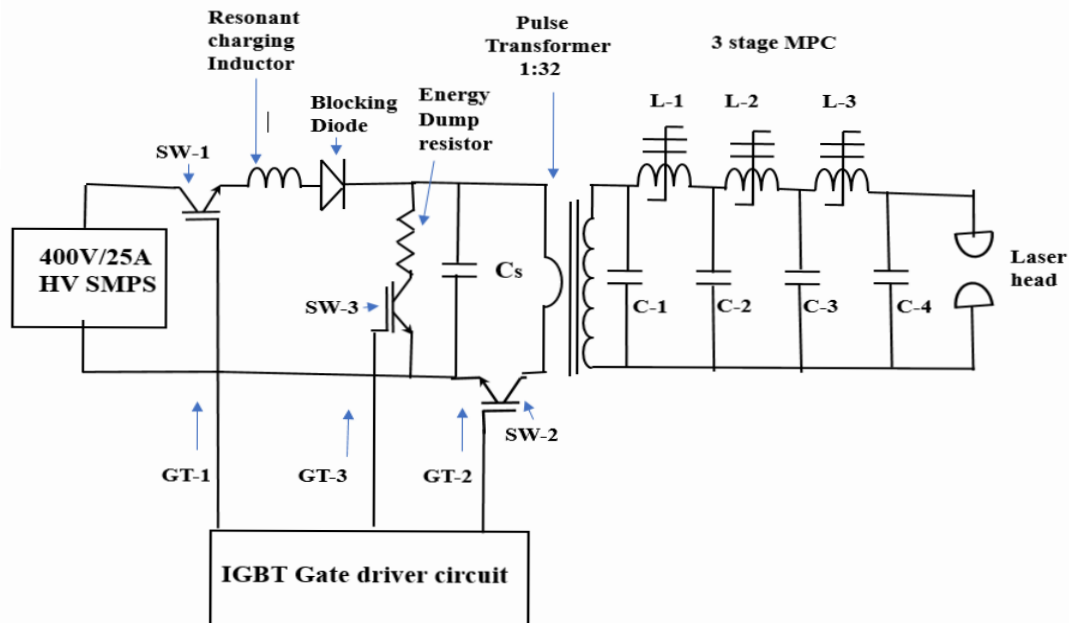


Fig.2: Schematic of Pulse Generator Unit.

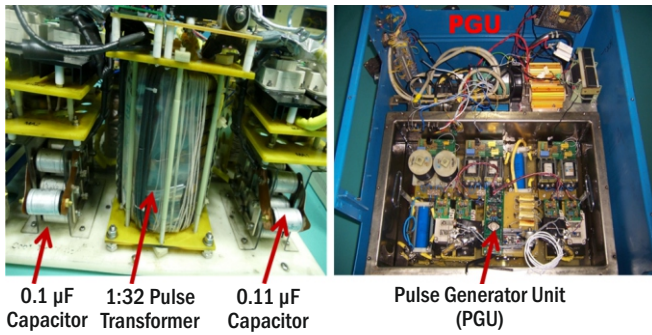


Fig.4: Photograph of capacitor addition across the parallel capacitor banks and Pulse Generator Unit.

Modification in the primary circuit

The primary circuit consists of two parallel sections, each section being identical, in which the primary storage capacitor is split into these two circuits. Each section consists of 9 capacitors (0.11μF, 1500 VAC, KP-12, ELCIAR make) connected in parallel in the capacitor bank. Thus overall primary capacitance results in 1.98 μF. In order to increase the optical power output from the each CVL, the pump power delivered into the individual laser head needs to be increased. The CVLs are arranged in the Master Oscillator Power Amplifier (MOPA) configuration to boost the overall optical power which is being utilized for pumping tunable dye lasers [5]. The optical output power of the dye lasers is directly dependent on the energy per pulse of the CVL. Hence the energy delivered per pulse needs to be increased. This is achieved by adding additional capacitor of 0.11 μF the two primary capacitor banks. The resultant capacitance value of capacitor bank with additional capacitors of 0.11 μF is 2.2 μF. The value of C_s in Fig.2 has been increased by 11.11%. The location of this modification carried out in the pulse generator units is shown in Fig.4.

Similar analysis of the charging time of the capacitor, primary impedance, peak primary current, average primary current, energy transfer time from primary to secondary is done and the results have been tabulated for comparison between the system before and after the modification.

Table 1: Comparison of system parameters before and after modifications.

Parameter	Before Modification	After Modification
Capacitor charging time ($n\sqrt{LC}$)	54 μs	57 μs
Primary Impedance ($\sqrt{L/C}$)	8.7 Ω	8.25 Ω
Average Current [$2x(I_m/n) \times$ Duty cycle]	13.9 A	15.4 A
Energy Transfer time from primary to secondary	1.48 μs	1.52 μs
Rise time of first stage MPC	500 ns	506 ns
Rise time of second stage MPC	200 ns	202 ns
Rise time of third stage MPC	80 ns	81 ns

As seen in the table 1, the capacitor charging time has increased from 54 μs to 57 μs. This value is within the limit of charging IGBT (SW-1) ON time of 60 μs. This was incorporated while conceptualising the modification. The Average primary current increased by 10.8% from 13.9 Amp to 15.4 Amp. In order to test the improvement of the modified system, a single laser head was configured in plane-plane resonator configuration. For comparison purpose the CVL was operated firstly with the unmodified PGU in which the optical output power was measured to be 26 W using Ms Ophir make power meter. The capacitor bank of the same PGU was increased to 2.2 μF and used with the same CVL head. The optical power

Table 2: Comparison of optical power additions of two MOPAs before and after modifications.

laser	MOPA 1 Power (Watts)		MOPA - 2 Power (Watts)	
	Before Modification	After modification	Before Modification	After modification
OSC	12 – 13	15-16	7 – 8	10 – 12
AMP -1	35 – 36	39 – 41	18 – 20	25 – 28
AMP -2	50 – 52	58 – 60	38 – 42	48 – 52
AMP -3	72 – 75	90 – 92	55 – 58	68 – 70
AMP -4	86 – 88	108 – 110	72 – 74	92 – 95
AMP -5	105 – 107	125 – 127	90 – 93	115 – 120

generated was around 35 W. Thus in plane-plane resonator configuration the optical power increased by ~ 34% from 26 W to 35 W. The value storage capacitances of all the PGUs in the two MOPA chains each consisting of one oscillator followed by five successive amplifiers were increased to 2.2 μF. The optical power additions at the end of the individual stages of both MOPAs have been summarised below in Table 2.

The above data mentioned in the table 2 has been generated keeping the SMPS Voltage of each laser system fixed at 390 V and partial pressure of the CVL systems around 40 mbar. As seen from the above table there is around 20–30% increase in the power addition of the CVL MOPA. The current drawn by the SMPS also increased by 1.3 A to 1.5 A in the MOPA systems. The average current drawn from the system earlier were in the range of 12.7 A to 13.6 A. These current in the modified PGU increased to 14.2 A to 15.2 A at SMPS voltage of 390 V. This ensures higher current drawn from the supply at the same SMPS voltage. The laser head voltage and current waveforms before and after modifications have been shown in figure 5 and 6 respectively. The laser head voltage was measured using 1000:1 high voltage probe while the current measurement was done using high frequency current monitor having sensitivity of 0.1 V/A. Since the current is measured across only one out of four of the return conductors, the voltage developed across current monitor is to be multiplied by 40 to get the peak value of current flowing through the laser head. There is an increase in the laser head voltage from 12.2 kV to 13.2 kV and laser head peak current from 420 A to 500 A as shown in figure 5 and 6.

The input electrical power drawn by power supply increased by around 11% while the electrical power coupled into the laser head as well as CVL MOPA optical output power increased by around 22–28%. The entire system is currently working with higher efficiency as compared to the system prior

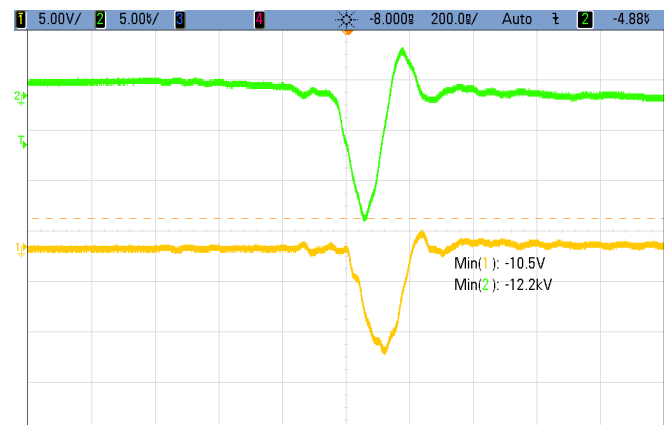


Fig.5: Laser head voltage & current waveforms before modification.

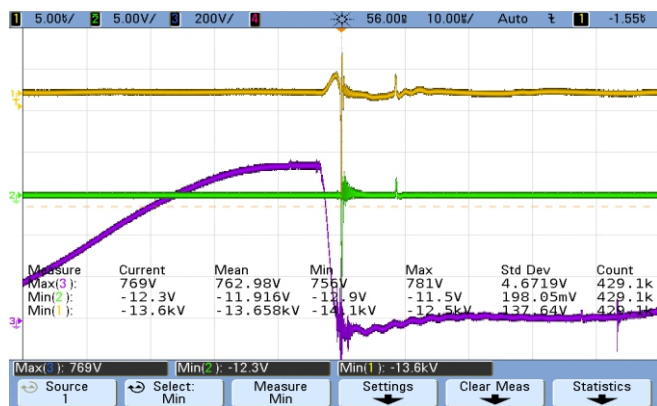


Fig.6: Laser head voltage & current waveforms after modification.

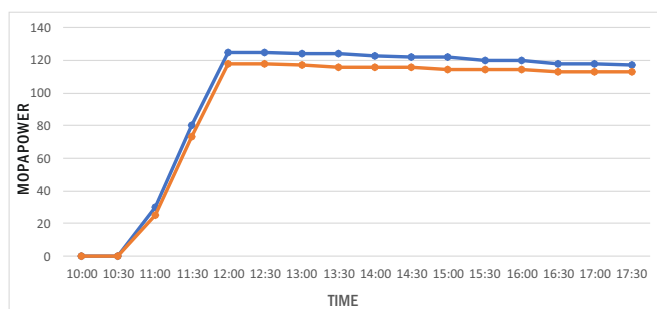


Fig.7: MOPA-1 Power (Blue) & MOPA-2 Power (Orange) v/s Time.

to the modifications in the PGU which is resulting in higher wall plug efficiency. In order to study the long term MOPA power stability, both MOPA-1 and MOPA-2 were operated and optical output power was monitored for five hours thirty minutes. The variation in the output power with time is plotted for each MOPA as depicted below in Fig.7.

As seen from Fig.7, The CVLs require around one hour forty-five minutes to two hours reaching the maximum optical power and this time is generally termed as warm up time for the CVLs. The optical powers remained almost constant within 5- 6% range for the entire duration of operation.

Conclusion

The optical power of the CVL MOPA chains has been enhanced by increasing the input energy storage capacitance value by 11.11%. Input electrical power drawn by the individual CVL increased around 11%. This resulted in the higher electrical energy coupled to discharge of the laser head. The single CVL operation in plane-plane resonator configuration resulted in the optical power enhancement of 34% while CVL MOPA optical power increased by around 22- 28%. The primary reason behind this is the increase in the energy gained by the

electron on account of increased voltage developed across the electrodes of the CVL. The excitation cross-section of the Cu atoms in vapor state also contributes to the increase in the optical power of the laser. The MOPA optical power remained stable for 330 minutes of continuous operation. This method of enhancement involves increasing energy per pulse of the CVL output which is essential one of the requirement of dye-laser pumping. This higher energy per pulse is advantageous in the laser based fortification process of stable isotopes to be used for generating radio isotopes.

Acknowledgement

The authors would like to express their sincere gratitude to Dr. Archana Sharma, Group Director, BTDG and Dr. S. Kundu, Head ATLAS for their interest and encouragement in this work. They also wish to thank their colleagues in the Laser Development section of ATLAS for their collaboration, technical discussions and dedicated efforts.

References

- [1] Little, C.E., "Metal vapour laser - Physics, engineering and applications". John Wiley & Sons Ltd publications, 1999.
- [2] S.V. Nakhe, "IGBT based pulse excitation circuit for copper vapour laser", Proceedings of DAE-BRNS National Laser Symposium, pp 187-188, 2002.
- [3] S.V. Nakhe, B.S. Rajanikanth and R. Bhatnagar, "Energy deposition studies in a copper vapour laser under different pulse excitation schemes", Measurement Science Technology, 14, pp 607-613, 2003.
4. Paramjit Rana, R. Vijayan, A.S. Rawat, Sunita Singh, L.M. Gantayet, "Performance characteristics of 9 kHz Copper Vapor Lasers", National Laser Symposium, NLS-08, 2009.
5. Paramjit Rana, S.K. Mishra, V.S. Rawat, Jaya Mukherjee, "Thermal Lensing in Copper Vapor Laser Oscillator-Amplifier Configuration: Its Measurement, Role and Compensation", Optik, 270, 169984, 2022.
6. R.K. Mishra, S.V. Nakhe, G.N. Tiwari and J.K. Mittal, "Development of insulated gate bipolar transistor-based power supply for elemental copper vapour laser", Pramana, Journal of physics, Indian Academy of Sciences, Vol. 75, No. 5, pp 967-973, Nov 2010.
7. D.K. Singh, Dikshit, B, Mukherjee J, Rawat V S, "Dynamics of magnetic pulse compression circuit of metal vapor laser", Journal of Physics: Conference Series, IOP Publishing, 1921, 2117, 2021.
8. D. Durga Praveen Kumar, L.M. Gantayet, Sunita Singh, A.S. Rawat, Paramjit Rana, Rajasree V, Sandeep K. Agarwalla, and D.P. Chakravarthy, "Analysis of temporal jitter in a copper vapor laser system", Review of Scientific Instrument, 83, 025105, 2012.
9. Dheeraj K. Singh, B. Dikshit, N.O. Kawade, Jaya Mukherjee, V.S. Rawat, "Exploration of jitter in pulse power supply of Copper Vapour Laser", Journal of Russian Laser Research, 41, 628 - 637, 2020.

Quantum Computing

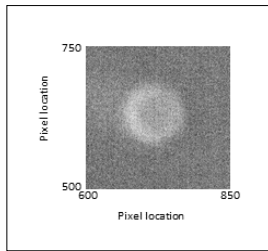
6

Laser Cooling of Atoms Down to Doppler Limit: A Step Towards Atomic Qubit

B. Pal¹, R. Behera¹, S. Baruah¹, T. B. Pal¹, S. R. Chowdhury¹, G. Sridhar^{1,2},
B. Dikshit^{*1,2}, S. Kundu¹ and Archana Sharma^{1,2}

¹ATLAD, Beam Technology Development Group, Bhabha Atomic Research Centre, (BARC), Trombay-400085, INDIA

²Homi Bhabha National Institute, Anushaktinagar, Mumbai-400094, INDIA



A typical photograph of cold atom cloud at steady state recorded by CCD camera

ABSTRACT

Atoms can serve as quantum bits (qubits) when trapped and controlled in predefined locations in space without undesired disturbances. Temperature of the atomic cloud needs to be lowered significantly to few microkelvin to efficiently trap the atoms in optical or magnetic micro traps. In an effort to demonstrate atomic qubits, we have recently trapped and attained the Doppler limited lowest temperature ($\sim 130\mu\text{K}$) of Caesium cold atom cloud using a magneto-optical trap. The temperature was measured by release and recapture technique. Our next goal is to reduce temperature further below by sub-Doppler cooling techniques up to $\sim 5\mu\text{K}$ so as to trap the atoms in optical lattice where entanglement of the qubits can be achieved.

KEYWORDS: Quantum computing (QC), Magneto optical trap (MOT), Caesium (Cs)

Introduction

Quantum computing (QC) has numerous future potential applications such as simulation of quantum processes, complex molecules, development of new drugs, storage and fast processing of huge data, secure communication, artificial intelligence etc. [1]. Different architectures are being explored for the experimental realization of quantum computing like superconducting qubit, ions traps, photons, nitrogen vacancy centers in diamond and neutral atoms [2]. Among these, atom based approach inherently offers scalability which is an important criterion of QC [3]. In this approach, thousands of ultra-cold atoms are loaded to optical or magnetic micro traps to create large array of individually controllable quantum system [4-5]. The quantum state is manipulated using laser or microwave pulses. In the atom-based quantum technology, the prerequisite is to cool the atoms by means of Doppler cooling technique and then trap them in a magneto optical trap (MOT). MOT is realised by overlapping three pairs of opposite polarization laser beams along with a quadrupole magnetic field [6]. In MOT, atomic gases can be cooled down to its Doppler limit which is typically $\sim 100\mu\text{K}$ for alkali atoms [7]. In all these applications of MOT, the knowledge of the characteristic parameters including the temperature and number of trapped atoms is indispensable. Many specialized techniques have been developed for the measurement of temperature of cold atom cloud in MOT. Among these, Release and Recapture method [8] and Time of flight method [9] are used most frequently.

In ATLAD, BARC, we are developing an experimental facility with an ultimate target of generation and manipulation of Caesium (Cs) atomic qubit. As an initial step, we have cooled and trapped Cs atoms in MOT and have estimated the temperature of the cold cloud by Release and Recapture method. The observed temperature has been found to be close to theoretically lowest possible temperature i.e. Doppler limit of the cooling process.

*Author for Correspondence: B. Dikshit
E-mail: bdikshit@barc.gov.in

Experimental Method and Results

The schematic and photograph of our experimental set up for cooling of the Caesium atoms in Magneto Optical Trap are given in Fig.1 and 2 respectively. The cooling laser is locked at a frequency red shifted by ~ 2.5 MHz from the cyclic transition $6s_{1/2} F=4 \rightarrow 6p_{3/2} F'=5$ (resonant frequency $\nu_0=351.7219605$ THz) of Cs. The re-pump laser is locked at $6s_{1/2} F=3 \rightarrow 6p_{3/2} F'=4$ transition (resonant frequency $\nu_0=351.7309022$ THz) of Cs. Magnetic field gradient is maintained at ~ 10 Gauss/cm. All the cooling and re-pump laser beam diameters are fixed at 5 mm. The optical power of the cooling laser and re-pump laser are kept at ~ 1.3 mw/beam and 0.3mW/beam respectively.

When the lasers are 'ON', cold atom cloud starts to build up in the trapping region due to the trapping force. Typically, within 500ms the cloud reaches to its steady state value where the momentum diffusion rate and the trapping rate balance each other. The fluorescence from the cold atom cloud at the trapping region is monitored by a CCD camera. Only the

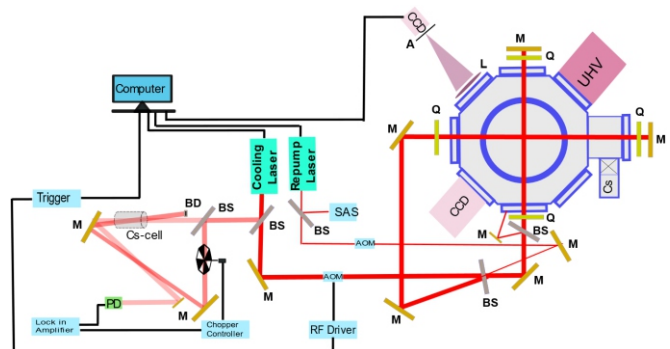


Fig.1: Schematic of experimental set up for cooling and measurement of temperature of Cs cold atom cloud in Magneto Optical Trap (MOT). UHV: Ultra high vacuum, Cs: Caesium atoms reservoir, Q: Quarter wave plate, AOM: Acoustic Optic Modulator, BS: Beam Splitter, M: Mirror, BD: Beam dump, L: Lens, PD: Photodiode, CCD: Charged coupled device. A: Aperture.

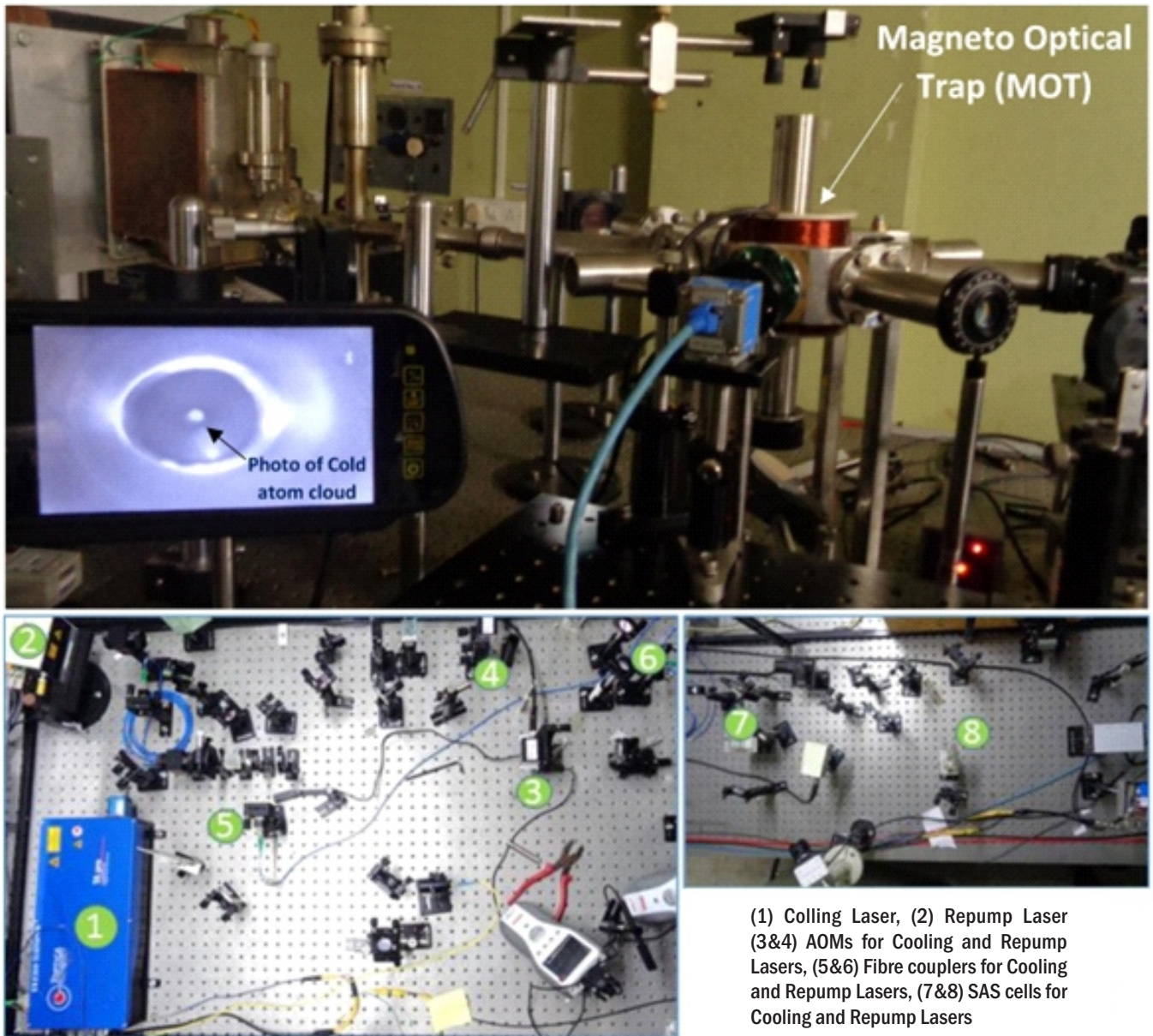


Fig.2: Photographs of Magneto Optical Trap (MOT) and Laser systems.

trapping region is focussed on the CCD sensor. Fluorescence from rest parts of the MOT is blocked from falling on the CCD sensor by an aperture. From the pixel count of the CCD, the total number of the cold atoms in the trapping region is measured [10].

Measurement of the temperature of cold atom cloud in MOT by Release and Recapture (RR) method is based on repeated release and recapture of atoms from the trapping region of the MOT. This is achieved by sequential 'ON' and 'OFF' state of the cooling beams. The duration of 'ON' and 'OFF' are adjusted by controlling the RF driver of AOM using a trigger module. Just before the 'OFF' period of the cooling beams, the cloud is in steady state. From the fluorescence image in CCD, the steady state number N_{ss} was evaluated and it was found to be 2.1×10^6 atoms and diameter of atomic cloud was ~ 0.65 mm. A typical steady state image is shown in Fig.3. Then the cooling beams are kept 'OFF' (i.e. releasing the cloud from trapping force) for a duration of t_{off} . There is no trapping force during this period and the cloud expands. As a result, the atoms are lost from the trapping region. After time t_{off} the cooling beams are brought back i.e. recapture of the remaining atoms

occurs, and the fluorescence image is taken in CCD. From this image, the number of left over atoms $N_{t_{off}}$ is given by [8],

$$f_r = \frac{N_{t_{off}}}{N_{ss}} = \left(\frac{m}{2\pi kT}\right)^{3/2} \int_0^{v_c} 4\pi \cdot e^{-\frac{mv^2}{2kT}} v^2 dv \quad (1)$$

where m is the mass of Caesium atoms, k is the Boltzmann constant, T is the temperature and $v_c = R_c / t_{off}$ is the velocity at which atoms reach the position R_c at time t_{off} . The value of integration is a function of t_{off} .

For different t_{off} , a plot of f_r vs t_{off} is experimentally generated as shown in Fig.4. Then, it is compared with the theoretically expected plots corresponding to different temperatures 'T'. Our experimental data matches with the theoretical plot at temperature $T \sim 130\mu K$. Thus, the measured temperature is very close to the Doppler limit of temperature of Cs which is $125\mu K$.

Conclusion

As temperature plays a critical role for controlling and manipulating the atomic qubits, we have attained the Doppler limited lowest temperature ($\sim 130\mu K$) of Caesium cold atom

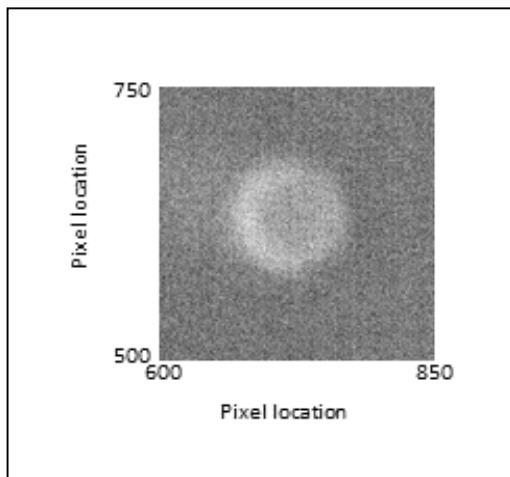


Fig.3: A typical photograph of cold atom cloud at steady state recorded by CCD camera.

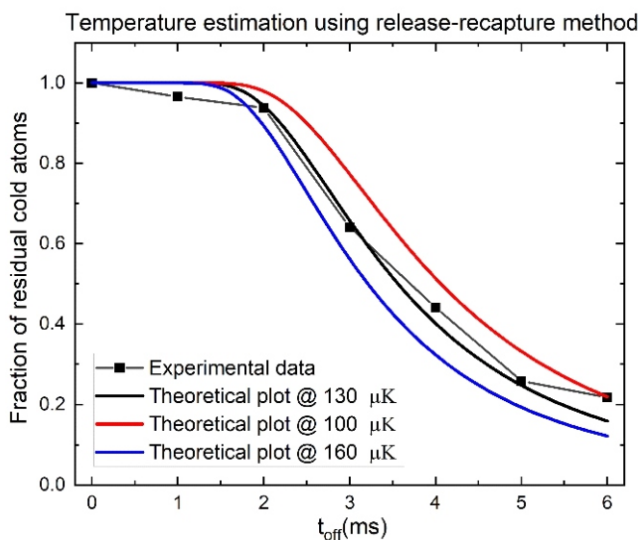


Fig.4: Variation of residual fraction of atoms in the trapping region of the MOT with 'off' period of cooling laser beams.

cloud trapped in a magneto-optical trap. We have measured the temperature by release and recapture technique. Since, lowering of temperature further below the Doppler limit up to about $\sim 5\mu\text{K}$ is required for trapping of single atoms in optical microtraps, we are at present in the process of implementing experimental techniques such as Sisyphus or polarization gradient cooling mechanism for obtaining sub-Doppler temperature of cooled Caesium atoms.

Acknowledgments

The authors would like to thank Dr. Someswar Rao and Sandeep Agarwalla of ATLAD, BTDR for providing optical components and support during the course of experiments.

References

- [1] Jonathan P. Dowling, Gerard J. Milburn, "Quantum technology: the second quantum revolution", *Phil. Trans. R. Soc. A.* 361.1655 (2003).
- [2] T. D. Ladd, F. Jelezko, R. Laflamme, Y. Nakamura, C. Monroe, J. L. O'Brien. "Quantum computers", *Nature* 464, 45 (2010)
- [3] DS Weiss and M Saffman, "Quantum computing with neutral atoms," *Phys. Today* 70, 7, 44 (2017).
- [4] D Barredo, V Lienhard, S De Leseleuc, T Lahaye, A Browaeys, "Synthetic three-dimensional atomic structures assembled atom by atom", *Nature* 561 (7721), 79 (2018).
- [5] M. Saffman, T.G. Walker "Quantum computer: Analysis of a quantum logic device based on dipole-dipole interactions of optically trapped Rydberg atoms", *Phys. Rev. A* 72, (2005).
- [6] EL Raab, M Prentiss, A Cable, S Chu, DE Pritchard, "Trapping of Neutral Sodium Atoms with Radiation Pressure", *Phys. Rev. Lett.* 59, 2631(1987).
- [7] R. Chang, A.L. Hoendervanger, Q. Bouton, Y. Fang, T. Klafka, K. Audo, A. Aspect, C. I. Westbrook, and D. Clément, "Three-dimensional laser cooling at the Doppler limit", *Phys. Rev. A* 90, 063407 (2014).
- [8] L. Russell, R. Kumar, V.B. Tiwari, S.N. Chormaic, "Measurements on Release-Recapture of cold 85Rb using an optical nanofiber in a magneto-optical trap", *Opt. Comm.* 309, 313 (2013).
- [9] TM Brzozowski, M Maczynska, M Zawada, J Zachorowski, W Gawlik, "Time-of-flight measurement of the temperature of cold atoms for short trap-probe beam distances" *J. Opt. B: Quantum Semiclass. Opt.* 4, 62(2002).
- [10] Daniel A. Steck, "Cesium D Line Data", available online at <http://steck.us/alkalidata> (revision 2.3.2, 10 September 2023).

Atomistic & Molecular Simulations

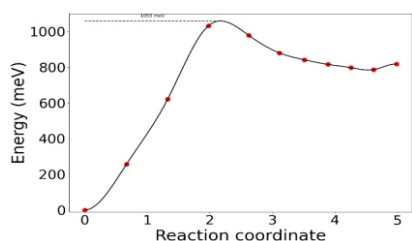
7

Atomistic Technology of Materials (ATOM) Software Suite for Computing Properties of Molecules and Materials

Nirbhay Chandorkar^{*1}, Anil Boda², Pooja Sahu², Kislay Bhatt¹, Sk. Musharaf Ali² and K. Rajesh¹

¹Computer Division, Bhabha Atomic Research Centre, (BARC), Trombay-400085, INDIA

²Chemical Engineering Division, Bhabha Atomic Research Centre, (BARC), Trombay-400085, INDIA



Activation barrier for Hydrogen on Metal Lattice

ABSTRACT

The ATOM (Atomistic Technology of Materials) initiative aims to develop a user-friendly software suite dedicated to streamlining input, output, and analysis for atomistic and molecular simulations. This letter focuses on the design and development of a sub module of ATOM software, specifically developed for calculations pertaining to the "Gas Storage and Permeation". Implemented using Python and the Django web framework, the application empowers users with functionalities such as job registration, viewing and editing existing jobs, file uploads and processing, and comprehensive analysis of calculated data. Through this platform, users can delve into diverse data sets, including energies, absorption energy, hydrogen gas diffusion, permeation, and solubility, enabling a thorough analysis. With a meticulously designed database schema, the application efficiently organizes and stores critical job-related information, files, energy profiles, parameters, and frequencies. Overall, this application stands as a valuable resource, offering both a user-friendly interface and robust analytical tools for managing and examining atomistic simulation data. Its significance lies in its potential to greatly benefit researchers operating in the fields of materials science and chemistry.

KEYWORDS: Atomistic modelling, DFT, Molecular Dynamics, SX and IX, Multi-component Glass, Barrier materials

Introduction

The recent advancements in computational chemistry and materials modeling along with computing technologies paved the way for design and development of novel materials with finest properties. Several material modeling software are presently available under open and private licenses. For example, the open software for material modeling includes GROMACS[1], LAMMPS [2], QUANTUM Espresso [3], etc. and private license software include TURBOMOLE [4], SCM-ADF [5], VASP [6], QUANTUM-ATK [7], etc. Each software has their own application and limitations for predicting the atomistic/molecular system and a single software cannot serve all the purpose. Hence, there is an urgent requirement for indigenous development of a software suite which can prepare the input, analyze and visualize the output and predict the molecular properties and work across all these types of software. Further, the computing solutions are very much required for visualization of properties of materials, the visualization will enhance the molecular study of various materials and will seed the next generation products to meet out the industrial requirements. The visualization technique is significant in bringing hidden physical properties of the material. The popular GUI are VMD [8], MERCURY [9], VESTA [10] etc. The main objective of ATOM software is to develop an Indigenous Integrated Environment which is capable of accepting the output of various atomistic simulation software and to extract meaningful information to further provide more complex

insights of the atomistic world. To design and develop this software it has been divided into six software modules which cater to following application areas: (i) Ion Extraction, Adsorption and Isotope separation, (ii) Gas Storage and Permeation, (iii) Water Purification and Desalination, (iv) Reaction Mechanism and Catalysis, (v) Multicomponent Glass, (vi) Energy Materials.

The present report describes the development and implementation of a software module for analyzing and managing atomistic simulation data for gas storage and permeation. This module is developed to analyze the material for gas storage (e.g., H₂) and permeation of gas through metals.

Chemistry of Gas Storage and Permeation

In a dense metallic membrane, hydrogen permeation occurs in seven steps as shown Fig.1, which are

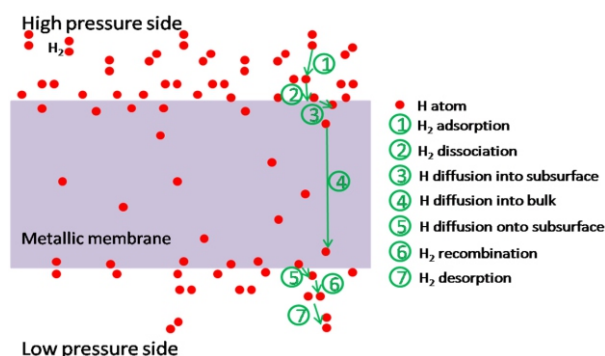


Fig.1: Schematic diagram of Hydrogen permeation through metal.

*Author for Correspondence: Nirbhay Chandorkar
E-mail: nirbhayc@barc.gov.in

- Adsorption of H₂ molecule at the high pressure side of the membrane surface.
- Dissociation of H₂ on the membrane surface.
- Penetration of H from surface to membrane bulk.
- Diffusion of H through the membrane bulk,
- Diffusion of H from membrane bulk to the surface on the collector side (low pressure) of the membrane,
- Recombination of H₂ molecule on the membrane surface.
- Desorption of H₂ from the collector side surface of the membrane.

Absorption or Adsorption Energies of H Isotopes in Bulk Metal or Surface

The absorption energy H atom in the bulk metal can be written as:

$$E_{ab} = E_{MnH} - E_{mn} - \frac{1}{2} E_{H_2}$$

Here E_(MnH) represents the energy of H atom in bulk supercell with n metal atoms. E_(Mn) represents the energy of bulk supercell with n metal atoms.

The zero point energy (ZPE): $ZPE = \sum_i \frac{(\hbar \nu_i)}{2}$

Diffusion of H and its Isotopes in the Surface/Bulk

Using harmonic transition-state theory in the classical limit and the random-walk model of interstitial diffusion in a lattice.

$$D = D_0 \exp \frac{-[\Delta E]}{kT}$$

D₀ in the Arrhenius expression for the temperature-dependence of the diffusion constant D can be expressed as:

$$D_0 = \frac{n}{6} a^2 \frac{\prod_{j=1}^{3N} \nu_j}{\prod_{j=1}^{3N-1} \nu_{\#j}}$$

Here, n is a geometrical factor for the number of equivalent jump paths (4 for H in the T-site), a is the jump length, and ν_j and ν_{#j} are the real normal mode frequencies at the initial state and the transition state, respectively.

The zero-point energy correction to barrier height can be considered using harmonic vibration frequencies and at room temperature.

$$E_a = E_{TS} - E_{stable} \quad \Delta ZPE_a = ZPE_{TS} - ZPE_{stable}$$

Permeation and Solubility

The permeability (Θ) can be evaluated using:

$$\Theta = \frac{1}{2} K_s(T) D$$

K_s(T) and D is the Sieverts constant (solubility) and diffusivity.

$$K_s(T) = \exp \left(\beta \left[\sum_i \frac{\hbar \omega_i}{4} - E_b - \sum_i \frac{\hbar \theta_i}{4} \right] \right) \frac{1}{\sqrt{\alpha}} \left(\sqrt{(1 - \exp[-\beta \sum_i \frac{\hbar \omega_i}{2}])} \right) \frac{1}{\prod_i (1 - \exp(-\beta(\hbar \theta_i)))}$$

with

$$\alpha = \left[\frac{2\pi m k T}{h^2} \right]^{\frac{3}{2}} \left(\frac{4\pi^2 I (kT)^2}{h^2} \right) \quad \beta = \frac{1}{kT}$$

ω_i and θ_i correspond to the vibrational frequency of isolated H₂ molecule and H atom in bulk metal. E_b is the binding energy of H atom with bulk metal. 'm' and 'I' represent the mass and moment of inertia of H₂ molecule. k, T and h are the Boltzmann constant, temperature and Planck's constant respectively. The atomistic simulations were performed using VASP and initial input was prepared using VNL.

Design and Development of Gas Storage and Permeation Module

The objective of Gas Storage and Permeation module is to calculate absorption or adsorption energies, diffusion, permeation and solubility constants of H and its isotopes in the metal surface or bulk. To achieve these goals, this module performs following three major tasks: (i) extraction of valuable information from the output files of various atomistic simulation software and to store them in the database., (ii) processing of the primitive data stored in database to compute more specific information related to "Gas Storage and Permeation", and (iii) a web based GUI to facilitate users to perform various operations such as uploading output files, data visualization and downloading generated results in form of excel sheets and plots.

Extraction of Important Data

This software module extracts the primitive information from the uploaded output files viz. OUTCAR, OSZICAR, CONTCAR etc., pertaining to structural optimization, single point and frequency calculations and folders from the Nudge Elastic Band (NEB) calculations using VASP software. This extracted information is stored in the database and uploaded files are stored against each job on the predefined area on the application server.

The module retrieves a list of all unprocessed job files from the database that are currently not being processed. Then, for each job file in the list, it retrieves, processes, and stores the information from job files in the database, ensuring that only unprocessed jobs that are not already being processed are processed. The first step is to set the job state to "is_processing" and then proceed with the processing. The job state is used to keep track of which jobs are currently being processed. If the file type is "OTC", "OTCI" or "OTCT", the function first reads the vibrational frequencies from the file, and calculates the zero-point energy (ZPE). It then saves the ZPE value to the database. It also saves the real and imaginary frequencies to the database as separate instances of the JobFreq model. If the file type is "TAR" or "ZIP", it first extracts the contents of the file (either tar or zip). The file is first extracted to a directory using either the zip file or tarfile libraries, followed by NEB analysis. It then calculates the initial energy, transition energy, transition index, and distance. These values are saved to the database using the JobParams and JobEnergies database models. Finally, the script generates a plot of the data and saves it before removing the extracted directory. Once all the processing is complete, the function marks the job as completed.

Computation of Absorption Energy, Diffusion, Permeation and Solubility of Gas

This module computes values of various coefficients and constants required for generating equations for gas diffusion, permeation and solubility. First, it computes corrected Absorption Energy with zero point correction. This amount energy is released by placing a H atom in the metal lattice. Second, it calculates gas diffusion coefficient and temperature dependent plots for the chosen range. Diffusion coefficient provide insights of thermal motion of gas particles through metal lattice. Next is calculation of solubility constant (K_s), alpha, beta and graphs of solubility constant against temperature. These are used in determining volume of gas that can be dissolved in a unit volume of metal. Solubility constant (K_s) is further used in calculation of permeation coefficient which provides estimates of penetration of gas through solid. This module also computes Thermal desorption spectrum

(TDS) of gas on the metal surface. Thermal desorption spectrum is simulated using AIMD simulations and Polanyi–Wigner equation to understand surface desorption kinetics. This module takes various inputs provided by the user such as participating molecules, order, gas coverage, pre-factor and starting and ending temperature. Then solves the Polanyi–Wigner equation using numerical method and plots the thermal desorption spectrum. Computed data and plots are archived for future reference.

Web based Graphical User Interface (GUI)

The graphical user interface facilitates users to use the application. It was decided to develop a web-based GUI instead of standalone (desktop based) application due its advantages over the later. Web based applications can be accessed over the network using browsers without requiring any installation at user end. These applications can be developed and updated efficiently and have wider reachability as they are independent of client machine's operating system. Following is the description of the various sections of ATOM web interface:

Login

This is the first page where user lands on accessing <https://atom.megh.barc.gov.in> through its web browser. Here, a registered ATOM user can login using the ATOM credentials. In case, a user forgets the password, a reset link is sent to his BARC email which enables it to change the password.

Register Job

This section allows users to submit a new job to the application. As per ATOM's nomenclature, a job is any simulation run whose output files are to be uploaded to ATOM for further processing. It has a form containing job name, molecule, job type, and job description fields. The molecule field is a small WYSIWYG editor in which users can add subscripts and superscripts. The job type is a drop-down field with the following options: Optimization Run, Optimization Run (Metal), and NEB. The frontend and backend validations are done before saving the job to the database. When a job is registered successfully, the user is redirected to a job list page, and a message is displayed confirming that the job has been registered. If there are any errors in the form, error messages are displayed to the user.

Job List and Update Job

Job list section contains a list of all the jobs registered by the user. The pagination is used to restrict the number of jobs to 10 per page. It contains the job name, molecule, job type, job status, and job creation date. It allows the user to delete the job and contains links to update the job, manage the job files, and show job energies. A job has the following status: Calculated, Ready to calculate, Calculating, Missing files, and Invalid files.

Update Job section allows users to update an existing job. It contains a form containing job name, molecule and job description fields. The molecule field is a small WYSIWYG editor in which users can add subscripts and superscripts. The frontend and backend validations are done before saving the job to the database. When a job is successfully updated, the user is redirected to a job list page, and a message is displayed confirming that the job has been updated. If there are any errors in the form, error messages are displayed to the user.

Manage Files

This section allows users to upload and view files associated with a specific job. If the job type is Optimization Run, then the form requires the user to upload OSZICAR and OUTCAR files.

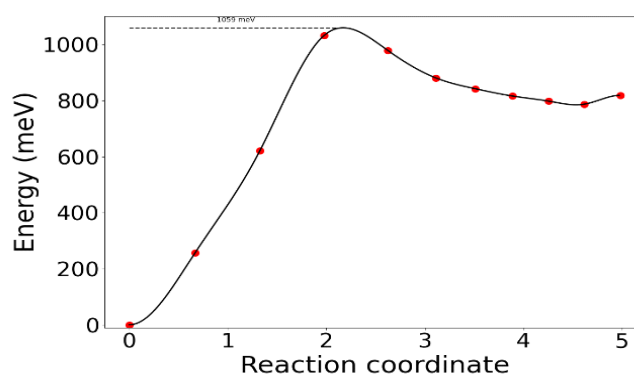
If the job type is Optimization Run (Metal), then the form requires the user to upload only an OSZICAR file. If the job type is NEB, then the form initially requires the user to upload a zip or tar file and the number of similar nearest neighbours. Once the uploaded file is processed, the user is given the index of the initial and transition states and is required to upload the respective OUTCAR files. As the files may be large, the user is shown a progress bar while the file is being uploaded. After the file is uploaded, the user is given the option to delete the file. If the file is being processed, the delete button is disabled. If the uploaded files are found to be invalid during processing, the user is notified and given the option to replace the file. The view also contains a link to the "Show Energies" section of the correlating job.

Show Energies

This section contains the job name, job type, molecule, job description, and job status. If the job status is "Calculated," the different parameters related to the job are displayed. If the job status is "Ready to Calculate," a "Calculate Now" button is displayed, which a user may click to process the job files; otherwise, the job files are automatically processed by the cron jobs. If the job status is "Calculating," a disabled button is

Show Energies

Job Name	Fe-H-0.5ML-desorption
Job Type	NEB
Molecule	Fe ₂₀ H ₂
Description	Desorption run for TDS
Job Status	Energy has been calculated.



Initial ZPE	0.0575 eV
Activation ZPE	0.0931 eV
ZPE Correction	0.0356 eV
Activation Energy	1059.4431 meV
Corrected Activation Energy	1.095 eV
Distance	4.9793 Å
Stable Image Index	0
Transition Image Index	3
Similar Nearest Neighbours	1
Real Frequencies (Initial)	51.7107 meV, 34.0341 meV, 29.2431 meV
Imaginary Frequencies (Initial)	13.7682 meV
Real Frequencies (Transition)	75.2256 meV, 73.7888 meV, 37.1435 meV
Imaginary Frequencies (Transition)	36.7213 meV
D ₀	0.0 cm ² /s

Fig.2: Show Energies page showing various job data.

displayed to indicate that the job files are being processed. If the user has not uploaded all the files, an "Upload Files" button linking to "Manage Files" is displayed. If the uploaded files are invalid, a "Replace Files" button linking to "Manage Files" is displayed.

Absorption Energy

This section is used to calculate the absorption energy. Firstly, the user is presented with a form to enter the number of reactants and products. After submitting the form, the form details are validated at the frontend and backend. If the form is valid, the user is presented with a form to select reactants and products using a drop-down menu and their respective coefficients, and a button to calculate the energy. The menu contains all the Optimization Run and Optimization Run (Metal) jobs, with only the jobs whose parameters are already processed. After clicking the "Calculate Energy" button, the form is again validated at the front and back ends, and if the form is valid, the equation along with absorption energy, ZPE correction, and corrected absorption energy are displayed.

Gas Diffusion

This section is used to calculate the gas diffusion rate over a range of temperatures. The user is presented with a form that contains a dropdown to select the NEB job (with only calculated jobs enabled) and fields for entering the starting temperature, ending temperature, step size, and multiplication factor. The user is also given a button that triggers a script that validates the data, generates various graphs, and calculates various parameters. The generated graphs and calculated parameters are shown to the user, and the user is given the option to download the graphs and the csv files containing the

calculated parameters and graph coordinates.

Gas Solubility

This section is used to calculate the gas solubility rate over a range of temperatures. The user is presented with a form containing an equation with fields for choosing a metal reactant from the dropdown containing Optimization Run (Metal) jobs, a gas reactant from the dropdown containing Optimization Run jobs, and a metal hydride product from the dropdown containing Optimization Run jobs. The form also contains fields for entering the starting temperature, ending temperature, step size, atomic mass, and distance. The user is also given a button that triggers a script that validates the data, generates various graphs, and calculates various parameters. The generated graphs and calculated parameters are shown to the user, and the user is given the option to download the graphs and the csv files containing the calculated parameters and graph coordinates.

Gas Permeation

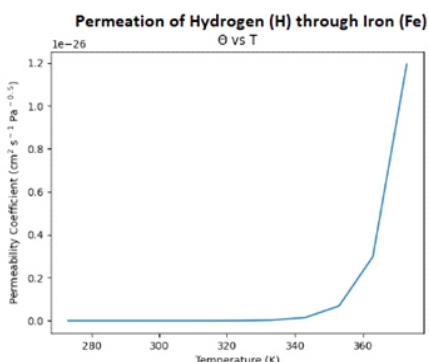
This section is used to calculate the gas permeation rate over a range of temperatures. The user is presented with a form containing an equation with fields for choosing a metal reactant from the dropdown containing Optimization Run (Metal) jobs, a gas reactant from the dropdown containing Optimization Run jobs, and a metal hydride product from the dropdown containing Optimization Run jobs. The form also contains a drop-down to select the NEB job and fields for entering starting temperature, ending temperature, step size, atomic mass, distance, and multiplication factor. The user is also given a button that triggers a script that validates the data, generates various graphs, and calculates various parameters. The generated graphs and calculated parameters are shown to the user, and the user is given the option to download the graphs and the csv files containing the calculated parameters and graph coordinates.

Conclusion

The ATOM (Atomistic Technology of Materials) represents an integrated module engineered to enhance the management of input, output, and analysis processes for atomistic and molecular simulations. Embedded within the ATOM Graphical User Interface (GUI) are four distinct sub-modules, each offering a suite of comprehensive tools. This report specifically outlines the development and deployment of a web application dedicated to the analysis and administration of atomistic simulation data, focusing on the Gas Storage and Permeation sub-module. In conclusion, the Gas Storage and Permeation module serves as a vital tool for researchers in materials science and chemistry, offering a comprehensive solution for analyzing atomistic simulation data. With its focus on calculating absorption energies, diffusion, permeation, and solubility constants of hydrogen and its isotopes in metal surfaces or bulk materials, this module plays a crucial role in advancing understanding in these fields. Through its intuitive web-based interface, users can efficiently manage input and output files, visualize data, and access results in formats suitable for further analysis. Overall, the Gas Storage and Permeation module stands as an indispensable asset, empowering researchers with the tools they need to conduct in-depth analysis and drive progress in atomistic research.

References

[1] Abraham, M.J. et al. (2015) 'Gromacs: High performance molecular simulations through multi-level parallelism from laptops to supercomputers', SoftwareX, 1–2, pp. 19–25.



NEB Job Name	Fe-H-0.5ML-desorption
NEB Molecule	Fe ₂₃ H ₂
Multiplication Factor	1.0
D ₀	2.494e-05
Corrected E _a	1.210e+00 eV
Mass	2.0 amu
Distance	1.0 Å
Moment of Inertia	8.303e-48 kg m ²
Binding Energy	6.193e-20 J
Gas Frequencies (Real)	414.6172 meV, 124.5908 meV, 124.499 meV
Product Frequencies (Real)	174.8075 meV, 173.1436 meV, 114.3856 meV
Gas Frequencies Sum (Real)	1.062e-22 J
Product Frequencies Sum (Real)	7.397e-23 J

Temperature (K)	Alpha	Beta	Permeability Coefficient (cm ² s ⁻¹ Pa ^{-0.5})
280			0.0
300			0.0
320			0.0
340			0.0
360			1.1

Fig.3: Permeation of Hydrogen in Iron computed using ATOM.

- [2] Thompson, A.P. et al. (2022) 'LAMMPS - a flexible simulation tool for particle-based materials modeling at the Atomic, Meso, and continuum scales', *Computer Physics Communications*, 271, p. 108171.
- [3] P. Giannozzi, O. Barone, P. Bonfà, D. Brunato, R. Car, I. Carnimeo, C. Cavazzoni, S. de Gironcoli, P. Delugas, F. Ferrari Ruffino, A. Ferretti, N. Marzari, I. Timrov, A. Urru, S. Baroni, *J. Chem. Phys.* 152, 154105 (2020).
- [4] TURBOMOLE V7.3 2018, a development of University of Karlsruhe and Forschungszentrum Karlsruhe GmbH, 1989-2007, TURBOMOLE GmbH, since 2007; available from <http://www.turbomole.com>.
- [5] G. te Velde, F.M. Bickelhaupt, E.J. Baerends, C. Fonseca Guerra, S.J.A. van Gisbergen, J.G. Snijders and T. Ziegler, *Chemistry with ADF*, *Journal of Computational Chemistry* 22, 931 (2001).
- [6] Kresse G, Furthmüller J. Efficient iterative schemes for ab initio total-energy calculations using a plane-wave basis set. *Phys Rev B*. 1996;54:11169-86.
- [7] Søren Smidstrup, Kurt Stokbro, Anders Blom, Troels Markussen, Jess Wellendorff, Julian Schneider, Tue Gunst, Brecht Verstichel, Petr A Khomyakov, Ulrik G Vej-Hansen, Mads Brandbyge and others *J. Phys: Condens. Matter (APS)*, Vol. 32, pp. 015901 (2020).
- [8] Humphrey, W., Dalke, A. and Schulten, K., "VMD - Visual Molecular Dynamics", *J. Molec. Graphics*, 1996, vol.14, pp. 33-38.
- [9] C. F. Macrae, I. Sovago, S. J. Cottrell, P. T. A. Galek, P. McCabe, E. Pidcock, M. Platings, G. P. Shields, J. S. Stevens, M. Towler and P. A. Wood, *J. Appl. Cryst.*, 53, 226-235, 2020.
- [10] Momma, Koichi, and Fujio Izumi. "VESTA: a three-dimensional visualization system for electronic and structural analysis." *Journal of Applied crystallography* 41.3 (2008): 653-658.
- [11] A. Boda, S.M. Ali, K.T. Shenoy, S. Mohan, *J. Phys. Chem. C*. 123 (2019) 23951-23966.
- [12] A. Boda, S. Bajania, S.M. Ali, K.T. Shenoy, S. Mohan, *J. Nucl. Mater.* 543 (2021) 152538.
- [13] A. Boda, M.A. Sk, K.T. Shenoy, S. Mohan, *Int. J. Hydrogen Energy*, 45 (2020) 29095-29109.

Robust Waste Management

8

Synthesis and Characterization of Lead Silicate Glasses for Radiation Shielding Window Application

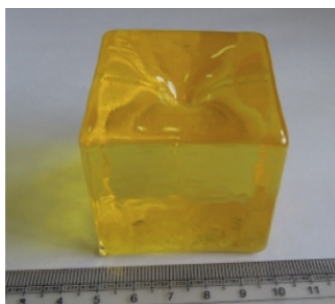
P. Nandi*¹, D. Dutta^{2,4}, B. Sanyal^{3,4}, R. Mishra¹, M. Goswami^{1,4} and A. K. Arya^{1,4}

¹Glass & Advanced Materials Division, Bhabha Atomic Research Centre, Trombay – 400085, INDIA

²Radio Chemistry Division, Bhabha Atomic Research Centre, Trombay – 400085, INDIA

³Food Technology Division, Bhabha Atomic Research Centre, Trombay – 400085, INDIA

⁴Homi Bhabha National Institute, Anushaktinagar, Mumbai – 400094, INDIA



Annealed glass block after melt casting

ABSTRACT

We have done the composition optimization of BaO-PbO-K₂O-B₂O₃-SiO₂ glass system with varying components. We achieved maximum density of 4.5 gm/cc having the necessary optical transparency of 80% at 550 nm in 10 mm thick sample. The glasses were irradiated in a Co-60 gamma chamber to study the changes in optical, thermal, mechanical, structural and radiation shielding properties. Linear attenuation coefficient remained same pre and post gamma irradiation, confirming the glass as a good radiation shielding material. Glasses doped with CeO₂ showed radiation resistance against browning up to 100 kGy. Raman spectra showed change in -Si-O-Si- ring structure post irradiation, causing the increase in refractive index. There was increase in non-bridging oxygen observed post irradiation resulting a decrease in transition temperature (T_g) and hardness of the glass. Using positron annihilation lifetime spectroscopy (PALS) measurements we have observed increase in voids/ free volumes post-irradiation. The lead silicate composition reported here is having required optical and shielding properties and have the potential radiation shielding window application.

KEYWORDS: Radiation shielding Glass, Irradiation effects, RSW, Optical Glass

Introduction

Radiation shielding window (RSW) glasses are optically transparent radiation shielding materials required for safe monitoring and handling of radioactive materials in the hot cells, nuclear plants etc. Compared to normal window glasses, RSW glasses are of higher density and have more attenuation coefficient against gamma radiations. At present RSW glasses required by various DAE units are mostly imported. The purpose of our present work is in-house development of these glasses as an import substitute for fulfilling the requirements of various nuclear facilities in India.

The first step towards development of RSW glass is to formulate the database of compositions having desired density, optical and radiation shielding properties. Commercial RSWs are Lead based glasses having density in the range 3.6 to 5.2 gm/cc but detailed compositions are not available. Based on literature survey we have chosen BaO-PbO-K₂O-B₂O₃-SiO₂ glass system and tuning of the composition was done with varying components to achieve maximum density without compromising the optical and radiation shielding properties necessary for RSW application. Further prepared glasses were irradiated in a Co-60 gamma chamber to study the physical, optical and structural changes. Linear attenuation coefficient, optical transparency, refractive index, glass transition temperature, and hardness were measured pre and post gamma irradiation. Concentration of CeO₂ was varied to study radiation resistance against browning with increasing doses of

gamma radiation. The post irradiation changes in physical properties were correlated with structural changes investigated by micro-Raman and positron annihilation lifetime spectroscopy.

Glass Synthesis

Glasses with varying compositions were prepared by melt quenching technique. 100 to 200 grams batches were melted in platinum crucibles in the temperature range of 1100-1150°C. For homogeneous mixing, the glass frits were pulverized to fine powder using planetary ball mill. The glass powder was re-melted and poured in a mold followed by annealing at ~ 400°C before slowly cooling down to room temperature. Prepared glass compositions (in wt%) are given below:

LG_1: 60PbO-10K₂O-30SiO₂

LG_2: 5BaO-55PbO-10K₂O-30SiO₂

LG_3: 10BaO-55PbO-10K₂O-25SiO₂

LG_4: 7.5BaO-55PbO-10K₂O-27.5SiO₂

LG_5: 7.5BaO-55PbO-10K₂O-25SiO₂-2.5B₂O₃

LG_6: 7.4BaO-55PbO-10K₂O-25SiO₂-2.5B₂O₃-0.1CeO₂

LG_7: 6.5BaO-55PbO-10K₂O-25SiO₂-2.5B₂O₃-1.0CeO₂

Addition of PbO increased the density of glass and was the main radiation shielding factor in the glass; SiO₂ was added as primary glass network former and K₂O acted as a network modifier & protected the glass from dielectric breakdown

*Author for Correspondence: P Nandi
E-mail: pnandi@barc.gov.in

Table 1: Density, Refractive index (RI), Hardness and glass transition temperature (T_g) of all prepared glasses.

Sample ID	Density (g/cm ³) ± 0.1	RI (n _D) @ 486 nm ± 0.0002	RI (n _D) @ 589 nm ± 0.0002	RI (n _D) @ 680 nm ± 0.0002	Hardness kg/mm ² ± 5	T _g (°C) ± 1
LG_1	4.4	1.6774	1.6543	1.6429	333	406
LG_2	4.3	1.6772	1.6534	1.6426	363	445
LG_3	4.6	1.6779	1.6547	1.6431	334	415
LG_4	4.5	1.6783	1.6550	1.6438	340	428
LG_5	4.5	1.6775	1.6542	1.6426	370	405
LG_6	4.5	1.6776	1.6541	1.6428	380	433

under gamma irradiation. BaO was gradually substituted in lieu of PbO to tailor the optical properties. B₂O₃ was substituted to decrease the melt viscosity and to increase homogeneity. CeO₂ doped glasses (LG_6, 7) was prepared to investigate radiation resistance against browning. The glass samples were exposed to different doses of gamma radiation in a Co-60 gamma chamber GC 5000 (BRIT, Mumbai) at FTD, BARC.

Results & Discussions

Physical properties

All the prepared glasses were found non-hygroscopic. The density of these glass compositions is given in Table 1. Density decreased in LG_2 as BaO was added in lieu of PbO. In LG_3 sample the density increased to 4.6 gm/cc due to increase in BaO content replacing SiO₂. The density remained at 4.5 gm/cc for LG_4, 5, 6 samples where PbO + BaO + CeO₂ percentage remained constant. In general, total percentage of PbO, BaO, CeO₂ is crucial for tuning the density in this glass system. Refractive index (RI) of the glass contributes to reflection losses, and higher RI leads to higher reflection loss. The relation of RI (n) and reflection loss (R) is $R = ((n-1)/(n+1))^2$. The reflection loss of ~6% from one surface was calculated for LG_6 glass at 589 nm. From Table 1, it was observed that when density increased, the RI of glass also increased and vice versa. Hardness of lead glass is generally low compared to other silicate glasses. However, hardness value increases with addition of BaO, B₂O₃ and CeO₂ as shown in Table 1. Thermal analyses of the glass samples were carried out to obtain the glass transition temperature (T_g), crystallization temperature. There was no crystallization peak observed in this glass and the T_g values are reported in Table 1. It was observed that the T_g

values increased with the addition of BaO and CeO₂, but addition of B₂O₃ in LG_5 glass decreased T_g compared to LG_4 without B₂O₃.

Radiation shielding properties

The radiation shielding parameters like linear attenuation coefficient (LAC), half value layer (HVL) was calculated using the Phy-X/PSD software [1] and are presented in Table 2. The values were calculated for gamma energy of 1.33 MeV, which is the maximum photon energy of Co-60 source. Lower value of HVL is favourable for shielding of gamma rays in confined areas like hot cells. Like density, HVL was also found to be dependent mostly on (PbO+BaO) concentration from our calculations. Experimental linear attenuation coefficient (LAC_E) of 1.33MeV gamma photons from Co-60 point source was measured using a LaBr₃ scintillation detector [2]. The intensity was measured with and without sample in between. The linear attenuation coefficient was calculated using the equation

$$N = N_0 e^{-\mu x}$$

Where N₀ is un-attenuated and N is attenuated intensity with sample in between, μ is the linear attenuation coefficient (LAC) and x is the thickness of the sample. The LAC values are experimentally measured before and after being exposed to gamma radiation are given in Table 2. In three samples LG_1, LG_5 and LG_6, slight decrease in LAC value was observed and in LG_4 slight increase in LAC value was observed after irradiation. No significant changes were observed indicating that all the exposed samples retained their radiation shielding capability post irradiation.

Table 2: Density and Radiation shielding parameters of the glasses pre & post gamma irradiation.

Sample ID	Glass Density (g/cm ³)	Mass attenuation MAC (cm ² /g) @1.33MeV	Linear attenuation LAC calculated (cm ⁻¹) @1.33MeV	HVL (cm) @1.33MeV [50% reduction]	LAC measured (cm ⁻¹) @1.33MeV Pre Irradiation	LAC measured (cm ⁻¹) @1.33MeV Post Irradiation
LG_1	4.4	5.783E-02	0.255	2.72	0.273	0.271
LG_2	4.3	5.746E-02	0.247	2.80	-	-
LG_3	4.6	5.718E-02	0.263	2.63	-	-
LG_4	4.5	5.732E-02	0.258	2.69	0.207	0.201
LG_5	4.5	5.729E-02	0.258	2.69	0.215	0.214
LG_6	4.5	5.729E-02	0.258	2.69	0.216	0.208

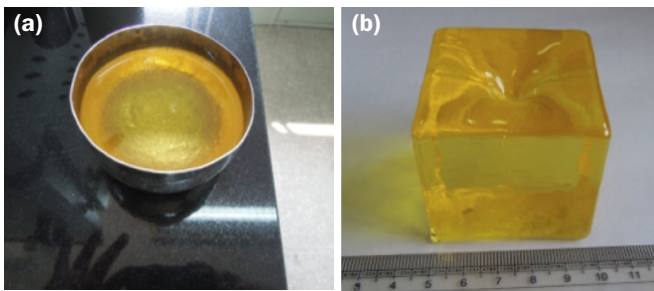


Fig.1: (a) Solid glass in platinum crucible before casting (b) annealed glass block after melt casting.

Preparation of lab scale glass block

For demonstration, we have successfully prepared a 600gm batch of LG_6 glass composition, calcined at 800°C for 24 hours followed by melting at 1100°C in a platinum crucible. The solid glass in platinum crucible is shown in Fig.1(a). Bubble free and transparent melt was obtained after cooling of the melt. Then molten glass was poured into a 50mm-50mm-50mm metal zig. The hot glass was immediately transferred to annealing furnace at ~400°C and slowly cooled to room temperature to release the thermal stresses. Annealed glass block without any visible casting defect is shown in Fig.1(b).

Effects of gamma irradiation

In order to study the post gamma irradiation effects on this composition, the polished glass plates and frits were exposed to gamma dose of 30 kGy. Fig.2(a) shows the glass plate LG_6 before irradiation and Fig.2(b) post irradiation. Immediately after irradiation, the glass turned brown in colour. The objects behind the sample were darker than the unexposed glass, because the transparency reduced post irradiation. However, the transparency was sufficient to see objects through the glass. Photograph shown in Fig.1(b) is indicative of the clarity of the objects we observed behind the glass. After 7 days the transparency of the glass was measured, showing an increase in transparency due to natural relaxation of colour centres. The glass was again tested for transparency after heat treatments at 100°C, 200°C, and 300°C for an hour. The transparency was gradually recovered after thermal annealing at 300°C.

Radiation resistance against browning

Radiation resistance against browning was studied as a function of CeO₂ concentration. Three glasses chosen were LG_5 (without Ceria), LG_6 (with 0.1 wt% Ceria) and LG_7 (with 1 wt% Ceria). Glass samples of each composition was cut and polished for transmission measurements before and after irradiations. Radiation doses up to 100 kGy were given cumulatively in all three samples in Co-60 gamma chamber. The change in glass colors for dose up to 100 kGy is shown in

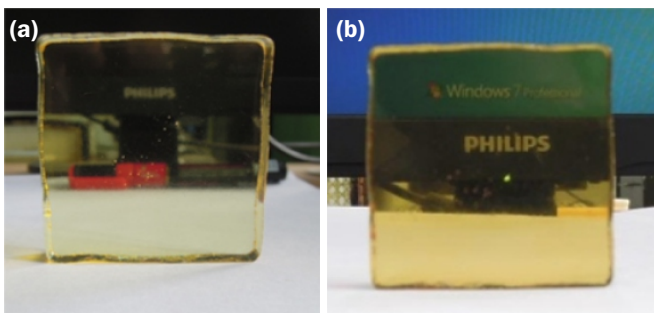


Fig.2: (a) is the pristine glass and (b) is the same glass post gamma irradiation. The glass turned slight brown due to formation of colour centres. However, it was sufficient to see the objects behind the glass as we can see in Fig.(b).

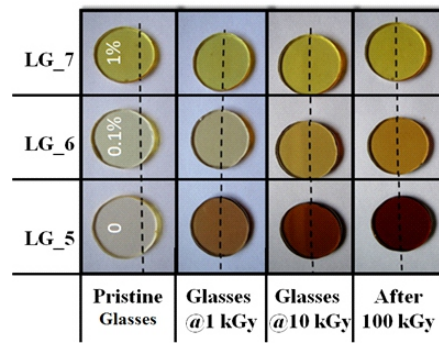


Fig.3: Change in glass color shown post irradiation at 1, 10 and 100 kGy dose. Dotted lines below the samples are given as a guide for the eyes to see the change in transparency post irradiation.

Fig.3. LG_5 turned brown in 1 kGy dose and become darker at 10 and 100 kGy. The reference black line behind the glasses was given as a guide for the eyes to visualize the transparency post gamma irradiation. LG_6 became slight brown at 10 kGy and beyond, but LG_7 showed no change in colour post irradiation up to 100 kGy. Analysis of optical properties, transmission and linear absorption coefficient (Fig.4) revealed that LG_5 can be given up to 1 kGy, LG_6 up to 10 kGy and LG_7 can be used beyond 100 kGy dose for radiation shielding application.

Radiation induced absorption

Radiation induced absorption (RIA) was measured to quantify the colour centres. It was calculated from transmission data. RIA was derived by the following equation as given in literature [3]:

$$T = T_0 e^{-(\alpha * L)}$$

$$\text{or, } \alpha = \frac{1}{L} \ln \left(\frac{T_0}{T} \right)$$

T₀ & T are % transmission before and after irradiation, and L is the thickness of the sample. The coefficient (α) was calculated for three glasses before and after irradiation shown in the Fig.4. LG_6 glass doped with 0.1% Ceria showed less absorption at all wavelengths after irradiation compared to LG_5 glass composition without doping. LG_7 glass doped with 1% Ceria, showed lowest absorption as expected from the glass colour. CeO₂ doping has improved radiation resistance against browning as observed in this glass system.

Effects of dose rate in radiation induced colour

The purpose of this study was to check the effect of dose rate on radiation induced absorption coefficient. Radiation induced absorption in LG_5 glass was studied at three

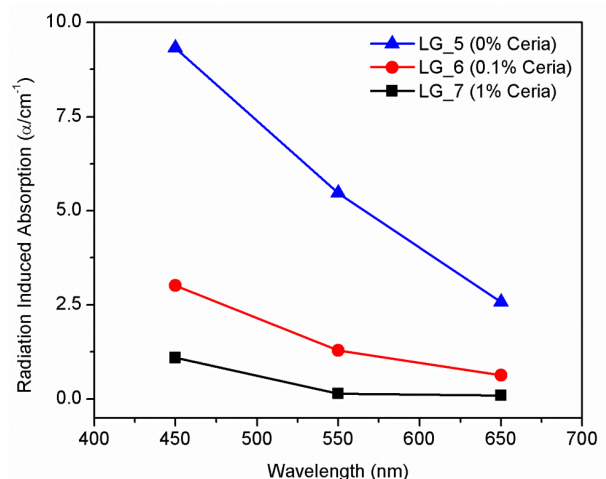


Fig.4: (Radiation induced absorption (RIA) measure for un-doped LG_5 and Ceria doped LG_6, LG_7 glass plates shown in the figure.

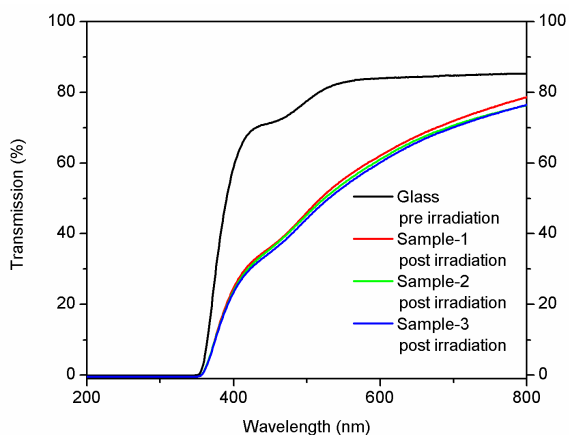


Fig.5: Transmission spectra of pristine glass and that of Sample 1, 2, 3 irradiated at three dose rates: 1 Gy/min, 15Gy/min and 78 Gy/min respectively, keeping total dose of 1 kGy constant for all three samples.

different dose rates. Total dose of 1 kGy was given at three different dose rates of 1 Gy/min, 15Gy/min and 78 Gy/min, in three different samples (1, 2, 3) prepared from one glass block. The transmission spectra are shown in Fig.5 for comparisons. At 550nm it was observed that the transmission (T) ~ 53%, 54% and 55% after radiation exposure in comparison with 83% in base glass. Similarly, at 650nm T% observed were 66%, 67% and 68% after irradiation compared to 84% in bulk glass. Apparently, transmission loss was indifferent of dose rate observed in this glass system.

Effect of UV annealing on colour centres

It was observed earlier that radiation induced colors can be efficiently annealed by heating of the samples upto 300°C temperature. However, heating of large RSW glasses are not recommended because of the risk involved. The purpose of the study of UV annealing was to find an alternative method of annealing color centers. Transmission was measured in pre and post irradiated samples. Subsequently, the radiation induced brown samples were kept under UV source for 1 to 8 hours and the transmissions were measured intermittently. The transmission measurements are shown in the Fig.6. After 8 hours of UV treatment a considerable improvement in transparency of the glass was observed. Though complete recovery of the transmission was not observed however, it was sufficient to see the objects clearly through the glass.

Refractive index post gamma irradiation

Refractive index (RI) was measured using multi wavelength Abbe refractometer (Model: Atago DR-M4). RI of LG_5 and LG_6 glasses were measured before and after irradiation. There was an increase in RI of glasses observed post irradiation in LG_5 and LG_6 glasses. RI of LG_5 increased from 1.6542 to 1.6554 at 589 nm green light. Similarly, RI of LG_6 increased from 1.6541 to 1.6551 measured at 589nm. It is reported in the literature that density and refractive index increase in borosilicate glasses after gamma irradiation [4]. Though, we could only measure the change in RI, most likely there was a change in density also. This change in RI could be due to the structural modification.

Hardness post gamma irradiation

The hardness of the glasses was measured by Vicker micro-hardness tester (Model: VMHT 30M, Leica). Indentations were made with a load of 50 g force applied for 5 seconds for hardness measurements. Hardness of LG_5 and LG_6 decreased after irradiation. The decrease in the hardness is generally linked to the increase in non-bridging oxygen (NBO) in

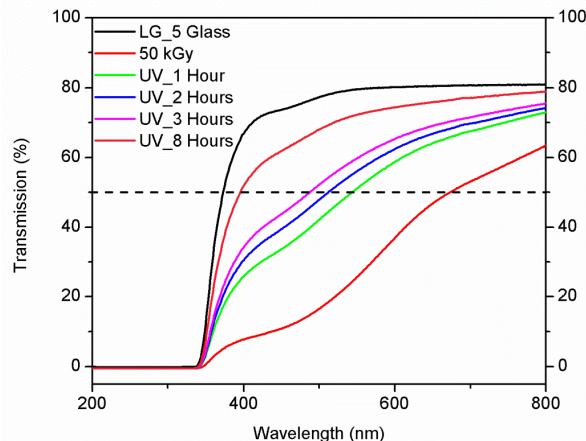


Fig.6: Transmission spectra of LG_5 glass pre-irradiation, post irradiation (50 kGy dose), and after UV annealing for different time periods (1-8 hours).

silicate glasses [5]. Accordingly, we assumed that there was a change in NBO in the glass after irradiation and has been confirmed by Raman study.

Glass transition temperature post gamma irradiation

DTA curves of LG_5 and LG_6 glasses were measured pre and post irradiation using differential thermal analysis (Setaram LABSYS). There was a decrease in T_g after irradiation observed in the glasses. In LG_6, T_g reduced from 433°C to 406°C; LG_5 T_g decreased from 405°C to 390°C. The difference in T_g in LG_5 and LG_6 was 16°C and 29°C, respectively. The decrease in T_g generally indicates depolymerisation of the glass network.

Structural analysis by Raman spectroscopy

Raman spectra were obtained using HR- Micro-Raman spectrometer (Model: Renishaw inVia). The samples were measured using 5 mW, 532 nm CW Laser. The literature suggested that the structural information of silicate glasses can be derived from the analysis of three important peaks in Raman spectra [6]. First peak at ~490 cm^{-1} corresponding to 3-member -O-Si-O- ring structure known as D1 peak. Second peak at ~606 cm^{-1} is known as D2 peak corresponding to 4-member ring structure. SiO_4 tetrahedron structure corresponds to the peak in the range 800-1200 cm^{-1} observed because of different Q_n structural units, where n is number of BOs in the silica network. Raman spectra of pre and post irradiated LG_6 glass sample are shown in the Fig.7. There is an increase in intensity of D1 and D2 peaks corresponding to 3 and 4 members SiO_4 ring structure. As the 3 or 4 member rings are more closed pack than 6 member rings, their increase will increase the density. Similar effect is also reported in the literature for quartz windows [7]. The increase in density can possibly explain the increase in refractive index after irradiation.

The increase in Q_n peak intensity was observed in post irradiated glasses. Q_n peaks were further deconvoluted to degenerate the individual Q1, Q2, Q3 and Q4 peaks as shown in the literature [6]. It was observed that Q4 tetrahedral units having all four BOs converted to other units like Q3, Q2, Q1 increasing NBOs in the structure. The increase in NBO explains the decrease in hardness and T_g post gamma irradiation.

Positron Annihilation Lifetime Spectroscopy (PALS)

PALS measurements have been carried out on lead glass (LG_5) pre and post gamma irradiation to compare their structural changes. The PAL spectra were analysed for discrete

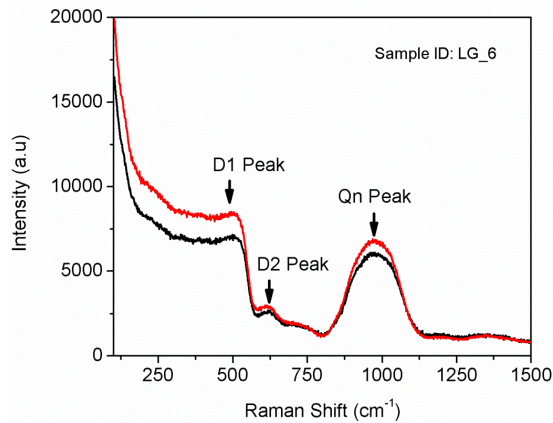


Fig.7: Raman shift measured in LG_6 samples pre irradiation (Black) and post irradiation (Red).

lifetime components derived using PALS fit analysis program [8]. The experimental spectra were best fitted with three lifetime components, namely τ_1 , τ_2 and τ_3 with corresponding intensity I_1 , I_2 and I_3 , respectively. The third component τ_3 and I_3 correspond to the ortho-positronium (o-Ps) pick-off annihilation in free volumes present in the sample. The τ_3 value was converted into average spherical free volume size in glass using Tao-Eldrup model. After gamma irradiation, the third component τ_3 increases from 1.28 ns to 2.10 ns, which correspond to increase in the voids or free volumes size in glass post gamma irradiation.

Structure-property correlations

We have investigated the correlation of the structural changes with changes in glass properties post irradiation. To understand the interaction mechanism of gamma rays with glass matrix a schematic is presented in Fig.8. Gamma rays enter the glass and ionize atoms leading to excited electrons and holes. These excited electrons ultimately get trapped in point defect or defect clusters already in glass matrix forming the colour centres. The electron trapped in colour centres can absorb certain part of visible light giving rise to the brown colour to otherwise colour less transparent glasses. Abrupt stopping of excited electrons created localized heating equivalent to its excess kinetic energy causing the structural changes. An increase in free volume was observed by PALS analysis. In the literature it is found that when free volume increases, it can push the silica network to have more compact network structure [9]. The same could be the reason what we observed as increase in 3 and 4 member Si-O-Si rings in Raman spectra leading to increase in refractive index of the glass after irradiation. Increase in NBO observed in Raman analysis could be responsible to decrease in T_g and hardness of glass post irradiation.

Conclusions

The composition optimization of BaO-PbO-K₂O-B₂O₃-SiO₂-CeO₂ glass system was carried out with varying components achieving density 4.5 gm/cc and transparency 80% at 550 nm for 10 mm thick glass. We have also synthesized a glass block of 50 x 50 x 50 mm³ for demonstration. Linear attenuation coefficient remained same pre and post gamma irradiation, confirm the glass as good gamma radiation shielding material. Glasses doped with CeO₂ showed radiation stability with respect to discoloration up to 100 kGy of gamma dose in Co-60 gamma chamber. We have also established structure-property correlations post gamma irradiation in this glass system. The glass composition with 1.0 wt % CeO₂ (LG_6) found to have good optical and radiation shielding properties suitable for RSW application. In future, scaling up of this glass composition

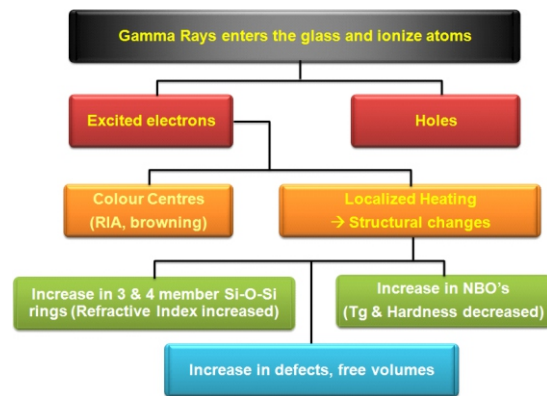


Fig.8: Schematic of the interaction of gamma rays with the glass matrix and subsequent changes in structure, properties are correlated in this figure.

for bigger dimensions will be taken up, where processing parameters like melting, homogenization and annealing will be optimized.

Acknowledgement

Authors wish to thank Dr. R. Tewari, Director, Materials Group for his valuable guidance in this project. We thankfully acknowledge Mr. Senthil Kumar, and Mr. P.A. Wagh for technical assistance in sample preparations.

References

- [1] Erdem Şakar, Özgür Fırat Özpolat, Bünyamin Alım, M.I. Sayyed, Murat Kurudirek, Phy-X / PSD: Development of a user friendly online software for calculation of parameters relevant to radiation shielding and dosimetry, Radiation Physics and Chemistry 166, 108496, 2020.
- [2] P. Nandi, D. Dutta, B. Sanyal, R. Mishra, M. Goswami, A. K. Arya; Structure-property correlation study of gamma irradiated BaO-PbO-K₂O-B₂O₃-SiO₂ glasses; Journal of Non-Crystalline Solids, 595, 121833, 2022.
- [3] E. J. Friebele, Radiation protection of fiber optic materials: Effect of cerium doping on the radiation-induced absorption, Applied Physics Letters 27, 210, 1975.
- [4] J. E. Shelby, Effect of radiation on the physical properties of borosilicate glasses, Journal of Applied Physics 51, 2561; 1980. (<https://doi.org/10.1063/1.327980>)
- [5] Arshpreet Kaur, Atul Khanna, Sapna Singla, Anupam Dixit, G. P. Kothiyal, K. Krishnan, Suresh K. Aggarwal, V. Sathe, Fernando González & Marina González-Barriuso, Structure-property correlations in lead silicate glasses and crystalline phases, Phase Transitions, 86:8, 759-777, 2013. (DOI: 10.1080/01411594.2012.707655)
- [6] Avadhesh Kumar Yadav, and Prabhakar Singh, A review of the structures of oxide glasses by Raman spectroscopy, Royal Society Chemistry Adv., 5, 67583, 2015.
- [7] Arnaud Zoubir, Clara Rivero, Rachel Grodsky, Kathleen Richardson, Martin Richardson, Thierry Cardinal, and Michel Couzi, Laser-induced defects in fused silica by femtosecond IR irradiation, Physical Review B 73, 224117, 2006.
- [8] P. Kirkegaard, J. V. Olsen, M. M. Eldrup and N. J. Pedersen. PALSfit. Roskilde: Danmarks Tekniske Universitet, Risø, National laboratoriet for Bæredygtig Energi. (Denmark. Forskningscenter Risoe. Risoe-R; No. 1652(EN)), 2009.
- [9] Madoka Ono, Kenta Hara, Masanori Fujinami, and Setsuro Ito, Void structure in silica glass with different fictive temperatures observed with positron annihilation lifetime spectroscopy, Applied Physics Letters 101, 164103, 2012.

Extreme Value Analysis of Rainfall at Tarapur

9

Comparison of Annual Maximum Series and Annual Exceedance Series

Saha Dauji^{*1,2}, Pankaj Srivastava^{*1}, Kapilesh Bhargava^{3,2}, A. Baburajan⁴, I. V. Saradhi⁵ and A. Vinod Kumar^{5,2}

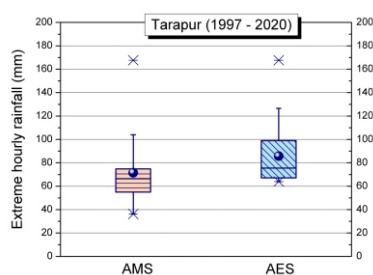
¹Nuclear Recycle Board, Bhabha Atomic Research Centre, Mumbai – 400094, INDIA

²Homi Bhabha National Institute, Anushaktinagar, Mumbai – 400094, INDIA

³Engineering Services Group, Bhabha Atomic Research Centre, Trombay – 400085, INDIA

⁴Environmental Survey Lab, Environmental Monitoring and Assessment Division, Bhabha Atomic Research Centre, Trombay – 400085, INDIA

⁵Environmental Monitoring and Assessment Division, Bhabha Atomic Research Centre, Trombay – 400085, INDIA



Box and whisker plot of extreme rainfall data by AMS and AES approaches for Tarapur during 1997 - 2020

ABSTRACT

Precipitation is an important consideration for ascertaining the design parameters for nuclear facilities and for flooding studies. Highest rainfall expected to occur at a site for a particular return period is estimated by extreme value analysis (EVA). For sample selection of EVA, two possible approaches are annual maximum series (AMS) and annual exceedance series (AES), each with respective strengths and limitations. In most of the studies on extreme precipitation for nuclear sites in general and Tarapur in particular, the annual maximum series approach had been adopted for discrete rainfall measurement. With continuous high-resolution (hourly) rainfall data now being available for 24 years (1997-2020) for Tarapur, the present article compares EVA of rainfall at Tarapur, conducted using both approaches in order to identify their respective limitations when applied for Indian rainfall conditions.

KEYWORDS: Extreme Value Analysis; Tarapur; Rainfall; Annual Maximum Series; Annual Exceedance Series

Introduction

Safety is one of the prime concerns during design of nuclear facilities, and safety against (external) flooding has attained renewed attention after the Fukushima accident in 2011. For the flooding analysis, the extreme rainfall that can be expected at a given site, corresponding to the designated return period for the facility, is generally ascertained by statistical analysis of the extreme rainfall values observed at site, also known as extreme value analysis (EVA). After Fukushima event, the design basis of flood protection measures for nuclear facilities in India, having offsite radiological hazard potential, has been upgraded from a return period of 1 in 1000 years to 1 in 10000 years [1]. AERB also provides the guidelines for extreme value analysis methodology for different meteorological parameters [2]. EVA consists of three steps: selection of a set of extreme values; finding the probability distribution function best suited to represent the selected sample; and finding the extreme value corresponding to the designated return period for the facility. Broadly, there are two different approaches for the first step, i.e. selection of a set of extreme values. These are called block maxima (BM) and peak-over-threshold (POT) approaches.

The BM approach initially specifies a certain block, generally chosen as a year owing to the annual periodicity of the seasons. Annual maximum series (AMS) is one BM approach in which the maximum (say, hourly) rainfall occurring in a year would be one sample; the maximum occurring in the next year would be the second sample, and so on – such that the final sample size would be equal to the number of years of rainfall records. The other approach, POT, first defines a threshold value of rainfall, and then selects all the rainfall

values higher than that threshold as the samples for EVA. In the former approach, high (say, hourly) rainfall occurring in two (or more) different instances in the same year would be missed and rainfall values less than these, but highest in other years could be selected – thereby affecting the EVA results. Annual exceedance series (AES) is one type of POT approach, which could be useful to overcome this limitation. However, in POT, the issue of fixing the threshold beforehand could be a serious limitation, as there are varied opinions regarding the selection of threshold across the hydraulic and statistical communities. The debate over the appropriate method for selection of threshold along with the requirement of extensive studies for the identification for a given problem has been discussed in literature [3, 4].

EVA has been reported for Tarapur based on the AMS approach in literature, using long term data spanning over 40 years [5]; 51 years [6]; and 60 years [7]. In this article, we present the results of EVA on Tarapur hourly rainfall data spanning over 24 years, conducted by both AMS and AES approaches.

Data and Methodology

The data for this study was obtained from Environmental Survey Laboratory, EMAD, BARC, Tarapur. This data was recorded by a continuous-recording rain gauge, and hourly rainfall values were aggregated for each hour. For the study, such hourly rainfall records were available for all 24 years, from 1997 to 2020. The quality checks were performed on the data received from this recording station and the results were found to be of very good quality as discussed in literature [8]. There was no gap in the data in any year, and this emphasizes the high quality standards maintained for data and records at ESL, Tarapur.

*Authors for Correspondence: Pankaj Srivastava and Saha Dauji
E-mail: pansriv@barc.gov.in and dauji@barc.gov.in

The earlier studies on extreme rainfall at Tarapur considered monthly [5], daily [5 – 7], and hourly [5] rainfall values of rainfall for EVA. Comparing the extreme daily rainfall value (539.9 mm for 50-years, and 657.1 mm for 100-years) estimated by Patel et al. [5] and those estimated by the recent study [7] as 629.88 mm for 50-years and 792.68 mm for 100-years, it can be observed that the inclusion of rainfall observations from the recent years have enhanced the probable maximum daily precipitation at the site. Compared to the extreme hourly rainfall values reported in literature [5] for Tarapur, as 107.1 mm for 50-year and 117.9 mm for 100-year return periods, the observed maximum rainfall at the site is higher (167.5 mm). The possible reasons for this phenomenon could be the enhanced precipitation in the recent years due to climate change effects, and the method of distribution fitting (graphical or least square technique) that was adopted for the study [5]. The aforementioned observations exemplify that EVA should be updated with new observed data and more advanced techniques. Updating the EVA for nuclear sites with latest data, and revisiting the hydrologic design in light of the same has been advised in the AERB standard as well [2]. In view of above, an attempt of examining the applicability of AES approach in estimate of extreme hourly rainfall for Tarapur has been made in this study.

For the comparison of the two approaches (AMS and AES), hourly rainfall values have been selected. The annual maximum values of hourly rainfall were taken from the data, and these 24 values formed the sample for EVA by a BM approach, known as AMS [9]. For AES approach, the threshold is selected such that the number of samples becomes equal to the number of years of record, making the sample size of AES same as that obtained in AMS approach [9]. The rainfall values higher than the threshold so selected were extracted from the 24-year records and this formed the sample for EVA by AES approach.

For maintaining uniformity, generalized extreme value distribution (GEV) is chosen for examining the suitability, as this was reported to fit the extreme rainfall values at this site [7]. The method of maximum likelihood estimation (MLE) is employed for estimation of the parameters of GEV distribution. MLE has been advocated by Srivastava et al. [7] for better estimates compared to the graphical [5] or Lieblein technique [6] for Tarapur, and the same has been adopted for this study as well.

Therefore, for each sample chosen by AMS and AES approaches, GEV distribution parameters were evaluated by MLE, as was mentioned earlier. After fitting a probability

distribution to a sample, the goodness-of-fit (GOF) needs to be examined before subsequent analysis. Compared to the GOF tests such as Chi-squared or Kolmogorov-Smirnov (K-S) tests, it is generally recommended to use Anderson-Darling (A-D) test in EVA, for proper evaluation of the fitted distribution towards the tails that are the zones of interest. The distribution functions, methods of parameter estimation, and GOF test are explained in textbooks [9 – 11]. After confirming from A-D test that the fitted distribution was acceptable for the data, the extreme rainfall values for various return periods pertinent for the nuclear facilities were estimated from the distributions obtained in the two approaches and the results are compared.

Results & Discussions

The descriptive statistics of the extreme hourly rainfall data obtained by adopting AMS and AES approaches are compared in Table 1 below, and the same is presented pictorially in Fig.1 as box and whisker plot.

From the data distribution presented in Fig.1, compared to the AMS approach, an upward shift of the extreme rainfall data can be discerned in the AES approach. One may also observe the descriptive statistics in Table 1, and note this as follows. The range of extreme rainfall reduced from 131.00 mm in AMS, to 103.50 mm in AES, whereas the maximum value remained the same for both. This shift of data was further reflected in a higher mean value as well as higher median value of rainfall for AES, when compared to AMS. Consequently the standard deviation as well as the COV has reduced for AES. The most note-worthy fact is that the non-zero skewness that indicates asymmetry of both the distributions, and the higher positive value for the AES series meaning that the variable (in AES) is more widely spread towards the upper extreme [11]. This property would result in higher values of extreme rainfall for lower probabilities of exceedance (higher return periods).

The empirical and fitted distributions are plotted in Fig.2(a) for AMS and Fig.2(b) for AES. From the figures, it is noted that both the distributions represent good fit to the data, which has been further corroborated by the A-D statistics as well. However, towards the upper end (cumulative probability closer to unity), whereas the fitted distribution lies above the empirical one (higher value) for AMS, it lies below (lower value) for the AES. This results in higher extreme rainfall values for low probability of exceedance in AES approach when compared to AMS.

The comparison of the extreme rainfall values obtained from the fitted distributions for various return periods are presented in Table 2, where it can be seen that the AES approach has

Table 1: Descriptive statistics of extreme hourly rainfall data at Tarapur during 1997-2020.

Statistics	AMS approach	AES approach
Count (nos.)	24	24
Maximum (mm)	167.50	167.50
Minimum (mm)	36.50	64.00
Range (mm)	131.00	103.50
Mean (mm)	71.46	85.68
Median (mm)	66.50	76.00
Standard deviation (mm)	29.34	24.96
Coefficient of variation (COV)	0.41	0.29
Skewness	1.82	1.86
Kurtosis	4.28	3.98

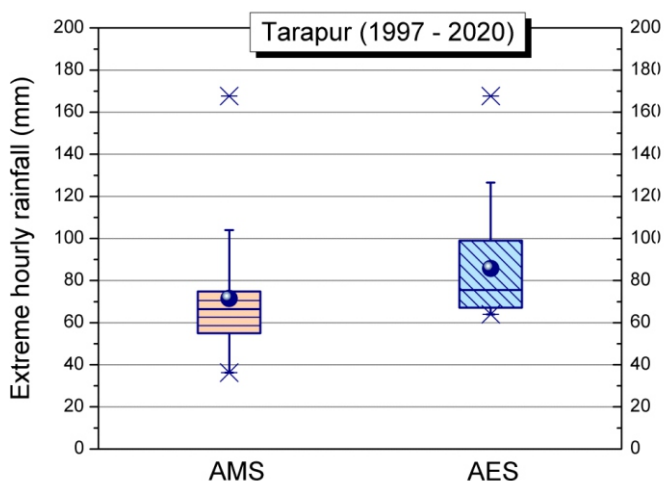


Fig.1: Box and whisker plot of extreme rainfall data by AMS and AES approaches for Tarapur during 1997 - 2020.

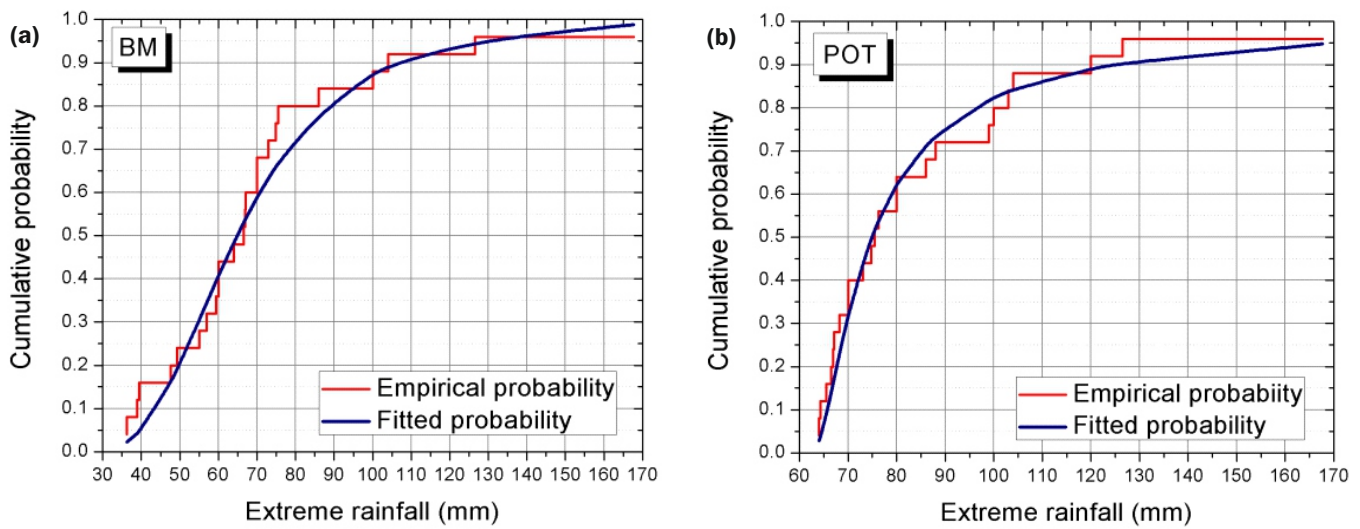


Fig.2: Empirical and fitted distributions, (a) AMS approach; (b) AES approach.

resulted in higher extreme rainfall compared to the AMS approach in each case considered. Additionally, the extreme hourly rainfalls for 50-year and 100-year return periods estimated (AMS as well as AES) from the recent 24-year data are substantially higher than those reported in literature [5] for Tarapur. A possible reason for this occurrence would be the inclusion of recent records in the present analysis, which were higher than those used by Patel et al. [5]. That the maximum hourly rainfall (167.5 mm) observed during the study period of 24 years is higher than the extreme rainfall at 50-year return period estimated in AMS approach indicates a limitation of that approach. In AES approach, this is overcome as the 50-year return period value is higher than the highest observed for the 24-year period. However, for larger return periods, it is observed that AES approach may lead to physically improbable values. In the present case, the extreme 1000-year hourly rainfall estimated in AES approach became comparable to the average annual rainfall for the site and much higher for higher return periods. This observation highlights that there is limitation in adopting AES approach as well. In literature, a similar observation was made for extreme 10000-year daily rainfall estimated using AMS approach for this site [7].

Summary and Future Scope

As reported in literature during last decade [6, 7], the extreme rainfall at Tarapur is observed to increase in recent years, possibly due to the climate change effects. This EVA study was conducted for hourly rainfall for Tarapur, with latest data (up to 2020) and comparison was made between such estimations performed in two approaches of EVA, namely, AMS and AES. The conclusions of the study are:

Table 2: Extreme hourly rainfall values for Tarapur from analysis of data during 1997-2020.

Return period (years)	Extreme rainfall value (mm)		
	AMS approach Patel et al. [5]	AMS approach (this study)	AES approach (this study)
50	107.1	153	289
100	117.9	176	451
1000	Not Reported	272	2351
2500	Not Reported	320	4685
10000	Not Reported	406	13443

- The extreme hourly rainfall for Tarapur has increased in recent years over those reported in literature two decades earlier [5].
- AES approach is successful in including more number of higher rainfall values in the sample when compared to AMS. This results in an upwards shift of the AES sample when compared to the AMS sample distribution with higher mean and median. The spread of the data reduces in AES compared to AMS, as was indicated by the lower standard deviation and COV. This would also lead to a more conservative design.
- The AMS approach conducted over 24-years data resulted in an estimate of extreme 50-year hourly rainfall value that was lower than the maximum observed value in the dataset used for the estimation. This indicated a shortcoming of the AMS approach, which was overcome in AES approach reported in this study.
- For return period of 1000 years or more, the AES approach yields hourly rainfall values that are physically impossible. These values are higher than the annual rainfall recorded till date at the site. This is indicated as a shortcoming of the AES approach that needs more investigation.

The results of this short comparison, using one approach of threshold selection, highlight the necessity of a comprehensive analysis of the meteorological parameters for Tarapur using different approaches, in order to arrive at updated design parameters applicable for the safety of infrastructure at this important industrial and nuclear site. Similar studies for other nuclear sites, having different meteorological and terrain conditions, with varying database, would provide deeper insights for optimal and safe designs, especially in context of extreme climatic behavior being witnessed.

Acknowledgements

Authors sincerely acknowledge the meticulous efforts of personnel at ESL, Tarapur for providing the high quality data used in this study.

References

[1] Atomic Energy Regulatory Board (AERB) (2014) Site evaluation of Nuclear Facilities, AERB Guide No. AERB/NF/SC/S (Rev.1). Atomic Energy Regulatory Board, Mumbai, India.
 [2] Atomic Energy Regulatory Board (AERB) (2008) Extreme Value

of Meteorological Parameters, AERB Guide No. AERB/NF/SG/S-3. Atomic Energy Regulatory Board, Mumbai, India.

[3] Bezak N, Brilly M, Sraj Mojca (2014) Comparison between the peaks-over-threshold method and the annual maximum method for flood frequency analysis, *Hydrological Sciences Journal*, Volume 59, issue 5, 959-977, <https://doi.org/10.1080/02626667.2013.831174>

[4] Tabari H (2021) Extreme value analysis dilemma for climate change impact assessment on global flood and extreme precipitation, *Journal of Hydrology*, Volume 593, 125932. <https://doi.org/10.1016/j.jhydrol.2020.125932>

[5] Patel PV, Patil SS, Kulkarni MR, Hegde AG, Gurg RP (2001) Extreme value analysis of meteorological parameters observed during period 1961 – 2000 at Tarapur. BARC Report No. BARC/2001/E/025. Bhabha Atomic Research Centre, Mumbai, India.

[6] Gupta A, Dauji S, Srivastava PK, Bhargava K (2018) Extreme Value Analysis by Graphical and Lieblein Techniques for Rainfall on Western Coast of India, *IWRA (India) Journal*, Volume 7, No. 2, July 2018, 38-45.

[7] Srivastava PK, Dauji S, Bhargava K (2023) Site- specific rainfall analysis to generate design parameters: A case study. *AIP Conference Proceedings*, 2721, 040001. <https://doi.org/10.1063/5.0153909>

[8] Harshanth R, Dauji S, Srivastava PK (2021) Quality Checks on Continuous Rainfall Records: A Case Study, In: Jha R., Singh V.P., Singh V., Roy L.B., Thendiyath R. (eds.) *Climate Change Impacts on Water Resources*. Water Science and Technology Library, vol. 98. Springer, Cham. https://doi.org/10.1007/978-3-030-64202-0_20

[9] Chow VT, Maidment DR, Mays LW (1998) *Applied Hydrology*, McGraw-Hill, Inc., USA.

[10] Coles S (2001) *An Introduction to Statistical Modeling of Extreme Values*, Springer – Verlag London Limited, Great Britain.

[11] Ang AHS, Tang WH (2007) *Probability Concepts in Engineering, Emphasis on Applications in Civil and Environmental Engineering*, John Wiley and Sons, New York.

HVAC System

10

Solar Powered Two Phase Variable Frequency Inverter Drive

Ashish Kumar Pandey*, Mahesh B. Patil, Vivek Sanadhya and S. Mukhopadhyay

Control & Instrumentation Division, Bhabha Atomic Research Centre, (BARC), Trombay-400085, INDIA



Hardware Full Load Test set up

ABSTRACT

This paper demonstrates the design and development of a two phase variable frequency drive (VFD) utilizing Insulated Gate Bipolar Transistor (IGBT) module in a three-leg inverter topology to control speed of single phase Induction Motor(IM) driving fixed speed reciprocating or rotary compressors, which are commonly used in air conditioning applications. The drive is capable of performing capacitor-less operation of single-phase induction motors up to power rating of 3 kW. It can be powered with both Solar PV panel and single phase AC power source. The key industrial features such as inrush current control, soft starting and various protection schemes have been incorporated into the VFD system design. The hardware design of a low-cost, compact inverter stack along with firmware implementation is presented. The Maximum Power Point Tracking-based (MPPT) algorithm have been implemented in the VFD and can be brought in if this solar inverter is the only load on the installed solar panel to maximize power utilization. Testing of the drive housed in a wall-mounted industrial enclosure, was conducted using a 2-TR air conditioning unit and the results are presented.

KEYWORDS: MPPT, Solar Insolation, Three leg topology, Capacitorless operation, Single phase induction motor

Introduction

The Heating ventilation air conditioning (HVAC) system powered by single phase 230V, 50Hz power supply make significant part of household/office load and conventionally operates in ON-OFF mode, because of fixed speed operation of compressor motor.

The commonly used single-phase IM in HVAC system are capacitor start (CS), capacitor start-capacitor run (CSCR) and permanent split capacitor (PSC) type which draws high current (8-10 times) at every turn on-turn-off cycle. Also due to fixed speed operation it is lossy and less energy efficient system [1]. Recently, HVAC system integrated with BLDC motor driven compressors in part load applications instead of IM was developed to increase system efficiency, ease of operation etc. However, this approach suffers from high capital costs. Moreover, this HVAC inverter systems powered by solar power have additional requirement of battery & associated controller [2].

This paper describes the design of a low cost VFD system which can be powered with solar PV panels without battery. This leaves an opportunity to run the same HVAC system on single phase 230V, 50Hz supply during night time when solar power is not available. The block diagram (Fig.1) shows that the main and auxiliary windings of single phase IM are connected to two legs, whereas the common point is connected to third leg of inverter. The dc link formed by capacitor C, C1 & C2 can be powered from solar PV panel or Voltage Doubler rectifier.

The signal conditioning board receives the signal from voltage sensors, current sensors and gate drivers. It generates appropriate control PWM pulses to drive IGBTs. The arm base MCU receives and transmits signal to User Interface along and signal conditioning board.

*Author for Correspondence: Ashish Kumar Pandey
E-mail: akpandey@barc.gov.in

Hardware Design and Development

The main challenge was to make the inverter compact, rugged, reliable, efficient, low cost and at par with commercial HVAC inverters. The low cost, compact (60mm x 55mm) SEMITOP series, Trench-4 IGBT module is used as inverter bridge. Each IGBT is driven by PWM switching pulses of magnitude +15V and -7V generated by optocoupler isolation based gate driver IC. Short circuit protection and under voltage protection are integrated in the gate driver IC. It conforms to UL 1577 and IEC60747-5-5 regulatory requirements.

The PV input voltage (V_{pv}) and DC link voltage measurement are carried out by high impedance isolated amplifier[5]. The amplifier has high input voltage range of 2V, $\pm 20\mu\text{V}/^\circ\text{C}$ drift error and high CMTI with fail safe mode operation. It provides galvanic isolation between high voltage DC link and signal electronics and enables accurate measurement of DC link voltages. The sensitivity of voltage sensors are 4.5mV/V. The DC link current (I_{dc}), PV input current (I_{pv}) and motor phase currents are measured by industrial grade, high precision isolated hall effect current sensor with accuracy of $\leq 1\%$ and sensitivity of 100mV/A. The hall effect sensors[6] provides CMTI of $\leq 50\text{kV}/\mu\text{s}$ and CMRR of 5uA/V with bipolar provision of current measurement.

The high temperature grade, high Comparative tracking index (CTI) Power PCB (Fig.2) with dimension 210mm x 160mm, 2mm thickness, was developed with integrated module type IGBTs mounted over aluminum heat sink. The power board houses the isolated voltage sensor, hall effect current sensor, gate driver for individual IGBTs, NTC temperature measurement, and short circuit protection circuitry. The layout design is carried out with IPC2221A directives and meeting standard EMI, EMC guidelines to minimize effect of high voltage noise on low voltage signal electronics. The board is designed with the voltage rating of

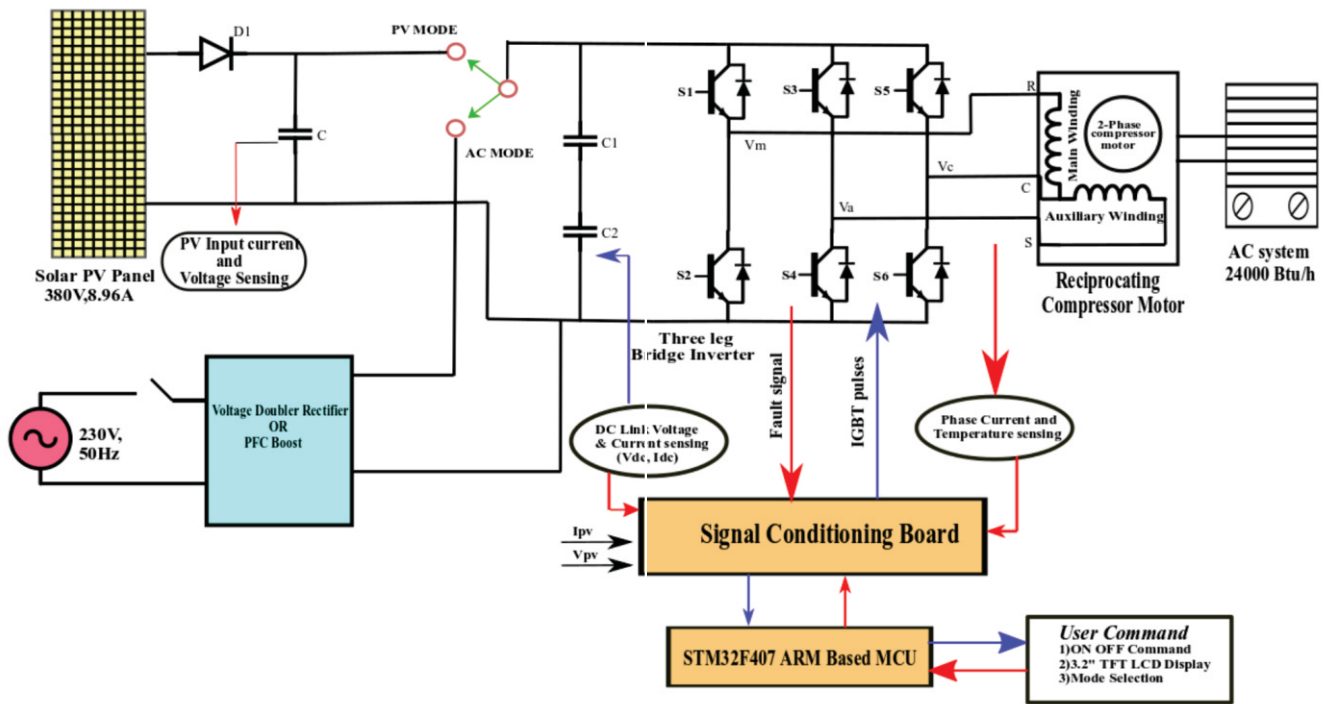


Fig.1: Block diagram of Air conditioning compressor drive powered by both solar power and 1-phase 230V, 50Hz AC supply.

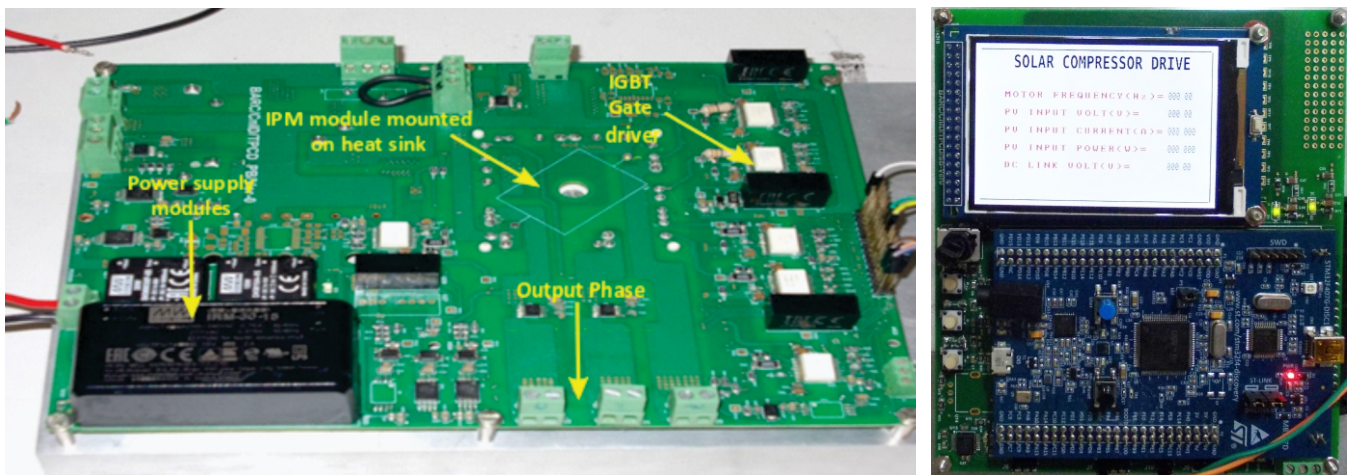


Fig.2: Power board with three leg IGBT Inverter module mounted on heat sink and Signal board with ARM based MCU unit, 3.2" LCD module and user interface.

1kV and track width to support 25Arms current. Phoenix make terminal connectors are provided on the board for connecting input power source from PV panel or 1- ϕ 230V, 50Hz and motor terminals directly. The Signal board (Fig.2) was developed which have microcontroller unit(MCU),operational mode selector rotary switch (Fig.3) and 3.2" TFT graphics LCD which displays essential parameters. The differential and single ended signals received from power board are conditioned by operational amplifier circuitry [7]. The signal board is mounted over the power board and housed in a wall mounted metal enclosure panel (Fig.3) with external MCBs and panel mounted switches.

Software Development

The control algorithm is implemented on a ARM based, 168MHz, 32bit MCU unit which have advanced PWM generation timers for motor control application. The two windings of single phase IM are powered with two orthogonal generated phases which ensures capacitorless operation and run as a two phase motor with a net starting torque. A carrier

based Sinusoidal pulse width modulation (SPWM) technique is implemented to generate 90° phase shifted IGBT control pulses [3]. The scalar control (constant V/F) algorithm for single phase IM [3] is used to control speed of compressor motor based on the available solar isolation. The Incremental conductance hill climbing MPPT [8] algorithm is implemented to maximize power output from the solar PV panels at any given solar insolation [4]. The drive can be operated in Solar mode and AC mode based on available solar insolation.

Results & Discussion

The performance characteristics are measured at various solar insolation by testing in different seasons to estimate the minimum and maximum power requirement of motor with the achieved cooling temperature. The Fig.4 shows voltage and current waveforms of motor windings at a minimum frequency of 14Hz and 31Hz at DC link of 325V (230Vrms). The voltage developed (Fig.4, c) at motor terminals are switching in nature due to IGBT switching. The current waveforms are smooth and sinusoidal in nature with lower

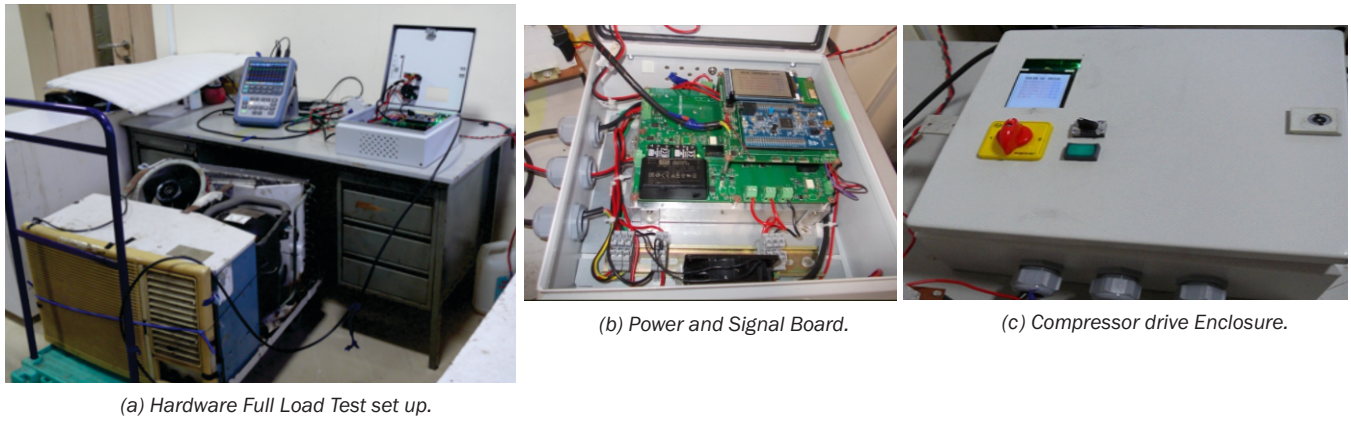


Fig.3: Air conditioning compressor drive powered test setup. (a) Inverter stack powering 2.3kW Compressor motor in 2-Ton AC unit. (b) Powered board and signal board assembled in a 300mm x 300mm x 210mm IP55 housing. (c) Compressor drive system in a wall mounted IP55 metal enclosure.

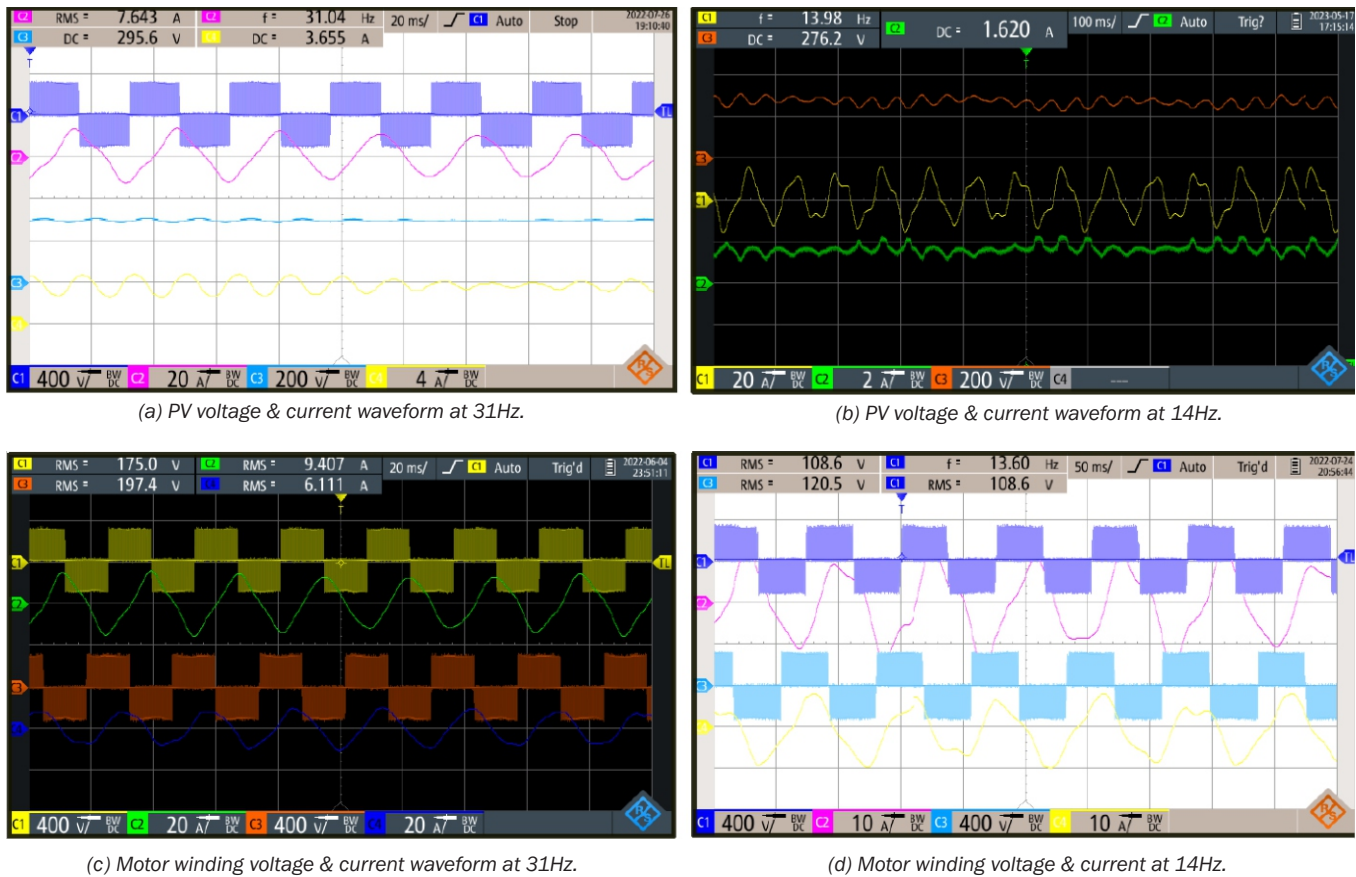


Fig.4: Test waveform at various solar insolation. (a) PV voltage, current main winding voltage & current at 31Hz. (b) PV voltage, current main winding current at 14Hz. (c) Voltage & current waveform at motor windings at 31Hz. (d) Voltage & current waveform at motor windings at 14 Hz.

distortion due to inductive nature of motor windings. The DC link voltage and current waveform are presented in Fig.4 (a,c). The minimum power requirement is around 450W at which the compressor motor runs at 840rpm (14Hz) and attains rated speed 50Hz with 450V(50Hz), 2.2kW input power.

The compressor is able to successfully regulate the temperature from 17°C to 25°C.

Conclusion

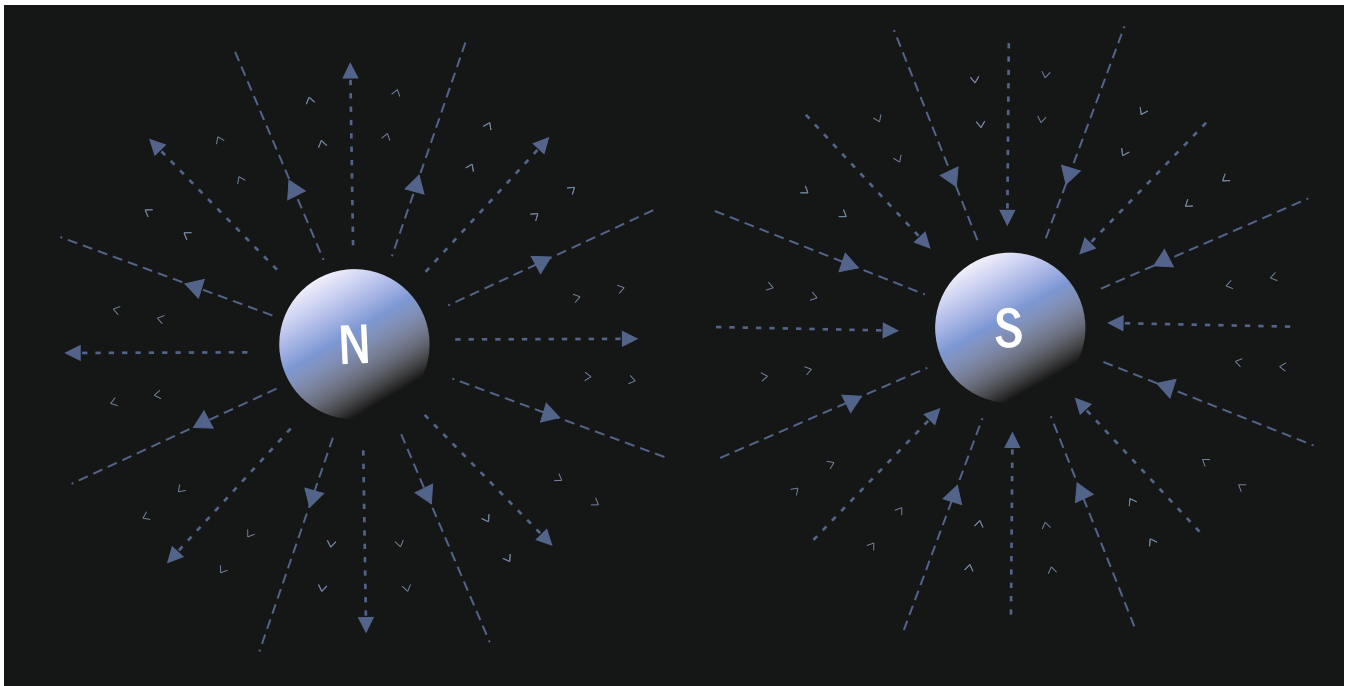
A low cost compact 3kW two phase variable frequency drive system is developed for single phase compressor motors. It is interfaced with Solar PV panel and AC source. The low power mode is tested at lower solar insolation levels. The drive

system is able to successfully drive a 2.3kW compressor motor at a power input of 450W at speed of 840rpm. The soft starting feature limits input current rise during transient condition to rated values. The low speed operation leads to power saving and speed regulation helps in achieving better temperature control and increased comfort level.

References

[1] A.S. Ba-thunya, R. Khopkar, Kexin Wei and H.A. Toliyat, "Single phase induction motor drives-a literature survey" IEMDC 2001. IEEE International Electric Machines and Drives Conference (Cat. No.01EX485), Cambridge, MA, USA, 2001, pp. 911-916, doi: 10.1109/IEMDC.2001.939428.

- [2] Singh, S., & Singh, B. (2015). Solar PV water pumping system with DC-link voltage regulation. *International Journal of Power Electronics*.
- [3] Kumsuwan, Yuttana et al. "A carrier-based unbalanced PWM method for four-leg voltage source inverter fed asymmetrical two-phase induction motor." *The 2010 International Power Electronics Conference - ECCE ASIA - (2010)*: 2469-2476.
- [4] Songbai Zhang, Zheng Xu, Youchun Li and Yixin Ni, "Optimization of MPPT step size in stand-alone solar pumping systems," 2006 IEEE Power Engineering Society General Meeting, Montreal, Que., 2006, pp. 6, doi: 10.1109/PES.2006.1708887.
- [5] AMC1311x High-Impedance, 2-V Input, Reinforced Isolated Amplifiers datasheet (Rev. C).
- [6] TMCS1101 1.5% Precision, Basic Isolation Hall-Effect Current Sensor With ± 600 -V Working Voltage datasheet.
- [7] OPAx192 36-V, Precision, Rail-to-Rail Input/Output, Low Offset Voltage, Low Input Bias Current Op Amp with e-trim datasheet (Rev. E).
- [8] T. Esum and P.L. Chapman, "Comparison of Photovoltaic Array Maximum Power Point Tracking Techniques," in *IEEE Transactions on Energy Conversion*, vol. 22, no. 2, pp. 439-449, June 2007, doi: 10.1109/TEC.2006.874230.



Hunting the Magnetic Monopoles

Krishna Kumar Singh

Astrophysical Sciences Division, Bhabha Atomic Research Centre, Trombay - 400085, India
 Homi Bhabha National Institute, Anushakti Nagar, Mumbai - 400094, Maharashtra, India
 E-mail: kksastro@barc.gov.in

A new pathway in basic and fundamental research has opened up due to the development of many state-of-the-art instruments for carrying out multi-messenger astronomy in the present era. These current generation astronomical instruments are capable of exploring the corners of Universe under extreme physical conditions and with kinetic ranges not accessible at man-made terrestrial accelerators and other laboratory environments. Thus, astrophysical observations provide unique and complementary opportunities for searching new particles as well as physics beyond the standard model and science in general. This contribution highlights the searches for an elusive particle known as Magnetic Monopole which was speculated in quantum mechanics in 1931 by Dirac in his study on quantized singularities in the electromagnetic fields.

More than a century ago, Max Planck introduced the natural units of measurement in 1900 and wrote: "All systems of physical units including the so-called absolute C.G.S.- system, appeared up to now due to accidental circumstances, as the choice of basic units in each of these systems occurred not from a general point of view valid for any place and time, but from the needs of our earthly culture" [1]. And, units for length, mass and time were derived in terms of three constants of nature: the speed of light in vacuum (c), the Planck constant or Dirac constant (h or $\hbar=h/2\pi$) and Newton's gravitational constant (G) and referred to as the Planck unit or scale [1,2,3]. These units have their

natural meaning as long as the laws of gravitation and of light propagation remain valid. As the fundamental principles of physics mainly emphasise the role of c , \hbar and G , a broad structure of different theories in physics can be described by a *Cube of Theories* through a suitable choice of units and setting the numerical values of these constants to unity. The cube of theories is located along three orthogonal axes marked by c^{-1} , \hbar and G in a three dimensional space. Moving along the c^{-1} -axis (with $G = \hbar = 0$) leads to the special theory of relativity wherein space and time are parts of a continuum instead of being separate entities. Non-relativistic quantum mechanics is invoked along the \hbar -axis (with $G = c^{-1} = 0$). The path along the G -axis (with $\hbar = c^{-1} = 0$) takes to non-relativistic, classical, Newtonian theory of gravitation. The origin of cube (with $G = \hbar = c^{-1} = 0$) represents an ideal non-relativistic mechanics and its vertices provide better and more accurate description of nature than the regions close to the origin. The vertex at $G = \hbar = c^{-1} = 1$ represents the study of quantum field theory in curved space-time, leading to the quantum gravity and the futuristic theory of everything.

Use of electromagnetic fields has now opened a new window in the fundamental physics research. Focused laser pulses are used to create extreme environments to study the high density and simultaneous interaction of particles and their dynamics. Formation of high density electron-positron plasma in the laboratory-mimicking the astrophysical environments in the Universe, can be exploited to produce particles and radiation sources with extraordinary physics properties. The particle dynamics is significantly modified in the presence

of strong electric and magnetic fields, giving rise to new physics phenomena which are generally not encountered in the classical or quantum theories of electromagnetic interactions. In order to illustrate such phenomena, a new cube of theories (analogous to the above described cube) has been proposed [4]. In this cube, the G -axis is substituted by a critical field of quantum electrodynamics (E_{cr}). In the theory of quantum electrodynamics, the critical electric field, E_{cr} , is defined as

$$E_{cr} = m^2 c^3 / e \hbar = 1.323 \times 10^{18} \text{ Vm}^{-1} \quad (1)$$

where mc^2 is the characteristic rest mass energy of electron and e is the unit electric charge. The equivalent critical magnetic field, B_{cr} , is given by

$$B_{cr} = E_{cr} / c = 4.41 \times 10^9 \text{ T} \quad (2)$$

These strong electric (E_{cr}) and magnetic (B_{cr}) fields also represent critical fields corresponding to the so called *Schwinger limit* of pair production [5] and are ubiquitous in understanding the quantum effects in strong electromagnetic fields. E_{cr} can be interpreted as an electric field which does work equal to the electron rest mass energy over a single reduced Compton length ($\lambda_c = \hbar/mc \sim 3.86 \times 10^{-13} \text{ m}$) and gyroradius of an electron in a magnetic field equivalent to B_{cr} would be equal to λ_c . When an electromagnetic field is characterized as strong or weak, its magnitude is implicitly compared to the scale of E_{cr} and B_{cr} . The vertex of cube of theories located at (c, \hbar, E_{cr}) encompasses quantum electrodynamics in ultrastrong fields. The strong-field aspect of quantum electrodynamics significantly alters the physics giving birth to new physics concepts which can be encountered only in the astrophysical environments in the space.

Magnetic Monopole

Magnetic Monopoles (MMs) are hypothetical particles explicitly predicted by several extensions of the standard model of particle physics, the widely accepted model for describing the subatomic Universe, as well as in theories describing the fundamental laws of physics. French physicist Pierre Curie was first to mention the idea of isolated magnetic charges in 1894. In 1931, English physicist Paul Dirac speculated about the point-like particle possessing an isolated magnetic charge in quantum mechanics by formulating the first field theory of a point-like MM interacting with quantum charged matter and proved that the existence of MM is necessary for quantization of electric charge [6]. He also proved that this hypothesis offers an explanation for the observation that electric charge is quantized. From the *Dirac Quantization Condition*, the allowed magnetic charges are given by

$$q_m = N e / 2\alpha \quad (3)$$

where N is an integer and α is the fine structure constant. $N = 1$ corresponds to the smallest allowed magnetic charge ($e/2\alpha$) known as the Dirac charge (q_d). Thus, the unit magnetic charge q_d of 1.09×10^{-17} Coulomb is much higher than the unit electric charge (e). In the Dirac's theory, MMs are treated as elementary particles with their mass as a free parameter which can be constrained experimentally. Moreover, in solutions of the grand unified theories (GUTs) of the known forces in nature, MMs appear as composites of the fundamental non-Abelian gauge and Higgs fields [7]. The masses of MMs are expected to be close to the GUT scale of $10^{16} \text{ GeV}/c^2$ and therefore cannot be produced in a realistic terrestrial collider experiment. The stability of MMs is attributed to the Higgs field configuration that cannot be smoothly transformed to a vacuum configuration having spatial uniformity. MMs have also been predicted by string theories and their masses are much lower than the GUT scale

depending on the string scale [8]. The composite monopoles of GUTs may have an internal structure unlike Dirac's point monopoles. Finite energy MMs with masses of a few TeV have also been proposed using the spontaneous symmetry breaking and Higgs mechanism in various theories beyond the standard model [9]. This gives prospects for plausible existence of magnetic monopoles in terrestrial collider laboratories.

The famous Maxwell equations of classical electrodynamics, introduced by the Scottish mathematician James Clerk Maxwell in 1870 by incorporating the electric and magnetic forces, offered the first hint of a possible unification of fundamental forces of nature. These set of beautiful equations appear asymmetric due to the absence of magnetic charges or monopoles. However, a magnetic current and a magnetic charge density can be introduced in Maxwell equations without loss of internal consistency or contradiction with experimental results. Thus, Maxwell equations also allow the existence of MMs to maintain their symmetry. They could have been formed in the early Universe as the temperature of the primordial plasma dropped below the energy scale of the GUT symmetry breaking. The expected production rate depends on the unknown nature of this phase transition, but it leads to a production comparable to the amount of baryons. This predicts a relic density of MMs at present epoch above the current observational limits. This is referred to as the *monopole problem* [10]. The primordial density of MMs can be brought to a level consistent with observations through inflation. Remaining MMs will be accelerated along the Galactic and extragalactic magnetic field lines.

Search for the Magnetic Monopoles

MMs are characterized as the isolated magnetic charge similar to a single north or south pole. Despite being allowed in theory, evidence of creating an isolated MM by separating a north pole from its south has not been found. Most searches for MMs, based on particle accelerator experiments, look for products of collisions between elementary particles such as electrons or quarks. But the strong coupling of MMs to each other and other standard model particles, as predicted by the Dirac's theory of point-like monopoles, makes it difficult to estimate the expected monopole yield. Although MMs have not been detected experimentally so far, searches for their existence are being continuously attempted with more powerful tools, opening a new pathway for exotic physics in fundamental research. In this direction, the current scenario from different physics and astrophysics experiments are described below:

■ **Schwinger mechanism in strong magnetic field:** In 1951, the US physicist Julian Schwinger demonstrated that electrically charged particles can be produced by the decay of a strong electric field [5]. This is referred to as *Schwinger mechanism*. Therefore, the principle of electromagnetic duality (electric and magnetic fields are linked) suggests that MMs can also be produced in a sufficiently strong magnetic field by the Schwinger mechanism [11]. Recently, an attempt has been made at the Large Hadron Collider (LHC) to search for MM production by the Schwinger mechanism in the enormous magnetic field induced by Pb-Pb heavy ion collisions [12]. The trapping detectors were exposed to $\sim 10^9$ Pb-Pb collisions with about 5TeV center of mass energy per collision. The magnetic field strength of $\sim 10^{16}$ T (approximately 10^4 times stronger than the surface magnetic field of neutron stars) was the strongest magnetic field measured on Earth so far. A superconducting quantum interference device (SQUID) magnetometer scanned the trapping detectors for the presence of magnetic charge which would induce a persistent



MACE Telescope facility under night sky.

current in the SQUID. No statistically significant signal of a magnetic charge trapped in the detector was found and therefore existence of Schwinger monopoles with magnetic charges of q_D , $2q_D$ and $3q_D$ and masses up to $75\text{GeV}/c^2$ was excluded at the 95% confidence level. This sets limits on the expected yield of MMs produced by strong magnetic fields and provides a lower mass limit for finite-size MM from a collider search.

■ **Atomic physics techniques in synthetic magnetic field environment:** Motivated by the analogues of MMs found in the exotic spin ices and other systems, a small group of researchers in the USA have demonstrated the creation of Dirac monopoles in the synthetic magnetic field produced by a spinor Bose–Einstein (BE) condensate [13]. The synthetic magnetic field arises in the context of a ferromagnetic spin-1 Rb-atom BE condensate in a tailored excited state. The BE condensate is described by a quantum mechanical order parameter, and the synthetic gauge potentials describing a north magnetic pole are generated by the spin texture. The phase variations of synthetic magnetic field accompany spatial variations in the intrinsic angular momentum or spin of the Rb-atom. The preferred spin varies in space in an engineered environment. Direct imaging is used to identify zero-density Dirac string that terminates within the BE condensate at the Dirac monopole. These results provide an unprecedented opportunity to observe and manipulate quantum mechanical entities in a controlled environment and lead to further exploration of the dynamics and excitations of a Dirac monopole.

■ **Astrophysical neutrino observatory:** The initial velocity of MMs must have slowed down to the non-relativistic speed. However, dynamo effects in magnetic fields of cosmic ray accelerators (galaxy clusters, active galactic nuclei, pulsars, magnetars) could have re-accelerated a fraction of MMs. A magnetic monopole traversing a magnetic field B with

coherence length L gains $E = q_m BL$ in kinetic energy. For typical galaxy cluster with $B = 3\mu\text{G}$ and $L = 1\text{kpc}$, the energy gain corresponds to $E = 1.8 \times 10^{11}\text{GeV}$. This mechanism allows that MMs could be associated with ultra high energy cosmic rays [14].

In the passage through matter or a dielectric medium, MMs moving at a speed faster than $0.75c$ would behave like an electric charge with strong exciting and ionizing power. Therefore, MMs can induce Cherenkov light like any other relativistic charge particle in a medium if their kinetic energy (E) is greater than a threshold energy given by

$$E_{th} = \frac{m_0 c^2}{\sqrt{1-1/n^2}} \quad (4)$$

where $m_0 c^2$ is the rest mass energy of charge particle and n is refractive index of medium. Therefore, Cherenkov detectors can be utilized to search for cosmic monopoles. IceCube neutrino observatory is equipped with a cubic-kilometer array of digital optical modules deployed at $\sim 2.5\text{km}$ depth below the surface of the glacial ice at the South Pole. It uses the ice both as target and detection medium to detect the Cherenkov light from secondary particles produced in neutrino interactions. It is also sensitive to searches for any new particles that can produce light that is detectable by the optical modules. It can be easily shown that a relativistic monopole produces $(q_m n/e)^2$ times as much Cherenkov light as an electron in a medium. In ice ($n=1.33$), a single charge monopole above the Cherenkov threshold emits about 8300 times more photons per unit length than a minimum ionizing muon. In a recent study, the IceCube collaboration has reported an all-sky 90% confidence level upper limit on the cosmic flux ($2 \times 10^{-19} \text{cm}^{-2} \text{s}^{-1} \text{sr}^{-1}$) of the relativistic Dirac monopoles with speeds between $0.75c$ and $0.995c$ without any explicit restriction on the monopole mass [15].

■ **Very high energy gamma-ray telescopes:** An MM can start producing Cherenkov light in the Earth atmosphere at a height of ~ 80 km from the ground. This emission may last throughout the full length of monopole track and will be confined within a narrow Cherenkov cone with angle starting from 0.1° increasing to 1.2° at the ground. The Cherenkov light produced by MMs can be recorded by the state-of-the-art *Imaging Atmospheric Cherenkov Telescopes* (IACTs) operating around the globe for very high energy gamma-ray astronomy. The magnetic monopole would be observed as a double-spot system in the camera of an IACT like MACE (Major Atmospheric Cherenkov Experiment): a first due to the very high altitude emission, and a second due to the low-altitude emission. The emission from the central part of the track would not be geometrically focused. The images of MMs in the camera of an IACT will mostly consist of small clusters of very bright pixels, for the high-altitude signal, or very bright fraction or rings, for low-altitude emission. Thus, illuminated pixels in the imaging camera will show extremely high signal due to large Cherenkov yield of MMs, at least 1000-times larger than that of muons. This will lead frequent saturation of photomultiplier tubes in the camera. The H.E.S.S. (High Energy Stereoscopic System) telescope at Namibia, an array of five IACTs, has performed a long-term search of MMs. For a total of 2400 Hours of data collected in 5 years, no MM candidate is detected. This null result has provided an upper limit of $4.5 \times 10^{-14} \text{ cm}^{-2} \text{ s}^{-1} \text{ sr}^{-1}$ on the cosmic flux of MMs [16]. This is an extremely poor constraint, orders of magnitude less constraining than IceCube limits. These limits are taken as conservative limits in a very simplified scenario, and further exploration is required. This gives a strong motivation to fully exploit the potential of the MACE telescope for fundamental research. MACE (depicted in figure) is a state-of-the-art current generation telescope for very high energy gamma-ray astronomy at Hanle (altitude ~ 4.3 km above mean sea level) in the UT of Ladakh, India. It has capability of detecting cosmic gamma-ray photons of energy above 20GeV through imaging atmospheric Cherenkov technique with high point source flux sensitivity. Thus, MACE stands a potential instrument for searching the cosmic magnetic monopoles in the coming future.

Outlook

The existence of magnetic monopoles is a mystery as they are hypothetical fundamental particles predicted by the theories beyond the standard model of particle physics. They are predicted to have a wide range of masses and need not be point-like. Low mass monopoles have a substructure and can be produced in particle accelerators. The implications of the existence of magnetic monopoles are far reaching. The unification theories, advocating for the existence of magnetic monopoles, motivate the development of a popular

cosmological model to explain the inflation phase during which the volume of space expanded exponentially. Many investigations are ongoing for evidence of magnetic monopoles - by searching in the Universe, and by attempting to produce and detect them in high-energy particle collider experiments on Earth.

References

- [1] On irreversible processes of radiation M. Planck; *Annals of Physics* 4 (1900) 69-122.
- [2] The fundamental constants of physics Lev B Okun'; *Soviet Physics Uspekhi* 34 (1991) 818.
- [3] An interpretation of the Cosmological Constant from the Physical Constants K. K. Singh; *BARC newsletter* 377 (2021) 22-25.
- [4] Electromagnetic cascade in high-energy electron, positron, and photon interactions with intense laser pulses S. S. Bulanov, C. B. Schroeder, E. Esarey, W. P. Leemans; *Physical Review A* 87 (2013) 062110.
- [5] On Gauge Invariance and Vacuum Polarization J. Schwinger; *Physical Review* 82 (1951) 664.
- [6] Quantised singularities in the electromagnetic field P. A. M. Dirac; *Proceedings of the Royal Society A* 133 (1931) 60.
- [7] Magnetic monopoles in unified gauge theories G. 't Hooft; *Nuclear Physics B* 79 (1974) 276-284.
- [8] Electric and magnetic charges in superstring models X. G. Wen, E. Witten; *Nuclear Physics B* 261 (1985) 651-677.
- [9] Magnetic monopoles revisited: models and searches at colliders and in the cosmos N. E. Mavromatos, V. A. Mitsou; *International Journal of Modern Physics A* 35 (2020) 2030012.
- [10] Magnetic Monopoles J. Preskill; *Annual Review of Nuclear and Particle Science* 34 (1984) 461-530.
- [11] Monopole pair production in a magnetic field I. K. Affleck, N. S. Manton; *Nuclear Physics B* 194 (1982) 38-64.
- [12] Search for magnetic monopoles produced via the Schwinger mechanism B. Acharya et al.; *Nature* 602 (2022) 63-67.
- [13] Observation of Dirac monopoles in a synthetic magnetic field M. W. Ray et al.; *Nature* 505 (2014) 657.
- [14] Signatures for a cosmic flux of magnetic monopoles S. D. Wick et al.; *Astroparticle Physics* 18 (2003) 663-687.
- [15] Search for Relativistic Magnetic Monopoles with Eight Years of IceCube Data R. Abbasi et al.; *Physical Review Letters* 128 (2022) 051101.
- [16] Signatures of ultrarelativistic magnetic monopoles in imaging cherenkov telescopes G. Spengler; Master's thesis, Humboldt-University of Berlin, 2009.

Indigenous IRMA Kit for Routine Estimation of Serum Thyroglobulin in Thyroid Cancer Patients

Radiation Medicine Centre, BARC
Completing a Decade of Accomplishment

Chandrakala Gholve and Nawab Singh Baghel

Radiation Medicine Centre, BARC, Mumbai-400012.
E-mail: kalagholve@barc.gov.in

Introduction

Radiation Medicine Centre (RMC) is one of the largest referral bases in India for the management of patients with various thyroid disorders including differentiated thyroid cancer (DTC) [1]. Constant efforts are being put in both *in-vivo* and *in-vitro* diagnostics for better care and management of the patients. RMC is a pioneer in Nuclear Medicine and due to its established infrastructure, various radioisotopic assays for thyroid analytes [Total T4, Free T4, anti-thyroid peroxidase autoantibody (TPOAb), serum thyroglobulin (Tg) and anti-Tg autoantibody (TgAb)] have been developed and validated here and some of them also found its applications for routine *in-vitro* patient services. Serum Tg is one of these in-house developed assays which was first developed in RMC and is still being used as a ‘tumor marker’ in the monitoring of thyroid cancer patients for almost 40 years. Thyroid cancer is the most common type of endocrine malignancy. About 90% of thyroid neoplasms are differentiated thyroid cancers with low malignant potential and a very good prognosis [2]. Serum Tg measurement is clinically useful for the postoperative monitoring of patients diagnosed with DTC with detectable and/or increasing Tg concentration indicating possible recurrent or persisting disease.

Evolution of Tg Assays at RMC: From where we Begin! A Look Back at the Past

At our Centre, in the early 80s, patient's sera were initially quantitated for serum Tg by an in-house developed radioimmunoassay (RIA) procedure [3]. The assay involved a primary incubation of radiolabelled Tg (¹²⁵I-Tg) and rabbit anti-Tg for 72 h and an additional 18 h incubation for precipitation of antigen-antibody (Ag-Ab) complex with goat anti-rabbit serum (GARS) in combination with *S. aureus*. Thus, in all, it took 90 h to report on a test sample. Therefore, there was a need to significantly reduce the overall total reporting time. Towards this, the initial approach had been to modify the second incubation step by using goat anti-rabbit antibody coated-magnetic particle (GAR-Ig-MP) as a mobile solid-phase in the separation system of the assay instead of GARS and *S. aureus*. With this method, the second incubation period was significantly reduced from 18 h to 2 h and facilitated an easy centrifugation-free separation system to separate the bound fraction from the free [4]. During this period, the sample load had started increasing gradually. Due to the long turnaround time (TAT) required by Tg RIA, the assay was performed once a week. RIA for Tg suffers from practical disadvantages [5] and due to these shortcomings, commercial assays favor the immunometric assay (IMA) format which comparatively offers higher sensitivity and precision with shorter TAT enabling quick reporting. Thus, this was the period when we decided to switch over from RIA to immunoradiometric assay (IRMA). Hence, to cater to the increasing patient load we switched over to imported commercial IRMA kits (a window period). The

commercial kits being highly expensive prompted us to standardize a two-step solid-phase IRMA using antibodies coupled to Magnetic particles (MP) and polystyrene-coated tubes (CT) as different solid-phases. Among the two developed IRMA formats, the CT-IRMA had better possibilities to be implemented for routine use in terms of sensitivity, precision and automation with a significant reduction in the TAT (14 h) thereby making the reporting time rapid. Figs.1-6 depicts the various steps involved in the manual immobilization of antibodies (one of the laborious steps in the production of in-house Tg IRMA kits).

Thus, the CT-IRMA came into routine practice for monitoring thyroid cancer patients from Nov 2013 onwards which is still being used satisfactorily in RMC. So far, we have produced approximately 2000 Tg IRMA kits and have analyzed more than 40,000 serum samples for Tg estimation in the follow-up cases of thyroid cancer patients. The cost of a commercial (Izotop) Tg IRMA kit is approximately Rs. 17,500/kit (100 Determinations) whereas an RMC-Tg IRMA kit costs approximately Rs. 2500/kit (100 Determinations). Hence, the overall cost of 2000 commercial kits would be approximately Rs. 35 million whereas for in-house kits it is Rs. 5 million. Hence RMC, BARC has saved the expenditure of Rs. 30 million and in addition, has generated a revenue of approximately Rs. 4 million from 40,000 samples in the last decade.

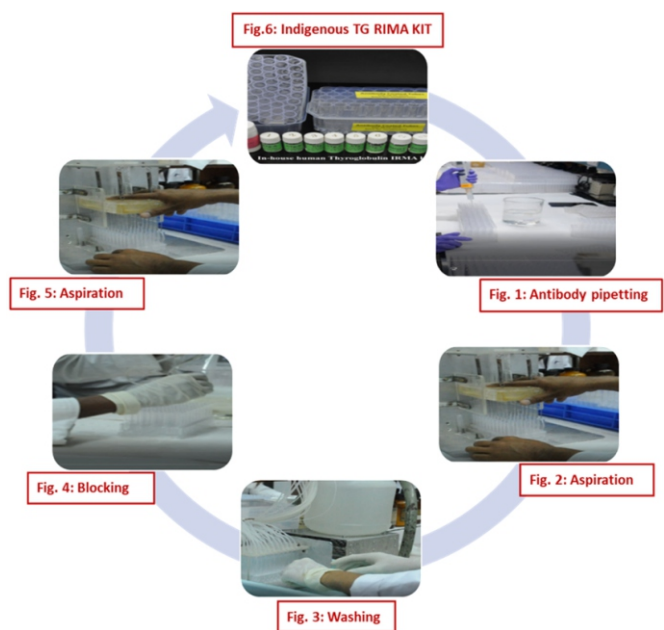


Fig.1-6: Various steps involved in the manual immobilization of antibodies at RMC for in-house Tg IRMA kit production.

Conclusion

This report concludes that RMC, BARC have completed a decade of accomplishment by taking a step forward towards self-reliance (Atmanirbhar Bharat) in securing the stock of entirely indigenously produced and highly economical Tg IRMA kits for routine thyroid cancer patient use. Thus, RMC has continued to deliver on its mandate the application of radiation technology solutions to address societal issues in the areas of healthcare and medicine.

Acknowledgements

Authors express sincere gratitude to Dr. Savita Kulkarni, former Head TIID Section, RMC; the Former Heads of RMC, M.G.R Rajan, Dr. Sharmila Banerjee, Dr. P. K. Pujari and Dr. T.K. Tyagi for their support and encouragement. The authors thank Dr. J. Kumarasamy, Jayendra Mori, U. Shaikh, Dinesh Bagul, Keshar Singh and Rahul Kashid for their involvement at various stages of this work. Sincere thanks to collaborators Dr. S.K. Ghorui, Senior Scientist, Former Director(s), N.V. Patil and Rajesh Sawal, ICAR-NRCC, Bikaner for their continuous support during the course of the work.

References

- [1] Gholve C., Kumarasamy J, Damle A., Kulkarni S., Ghorui S.K. Development of immunoradiometric assay kit for measuring serum thyroglobulin in differentiated thyroid cancer patients. BARC Newsletter. 2022:9-12.
- [2] Prpić M., Franceschi M., Romić M, Jukić T., Kusić Z. Thyroglobulin as a tumor marker in differentiated thyroid cancer—clinical considerations. Acta Clinica Croatica. 2018 Sep;57(3):518.
- [3] Kumar A., Devdhar M.N., Shah D.H., Ganatra R.D. Use of double antibody & Staphylococcus aureus as a separating agent in RIA of thyroglobulin. The Indian journal of medical research. 1985 Sep; 82:248-53.
- [4] Gholve C., Kumarasamy J., Damle A., Kulkarni S., Venkatesh M., Banerjee S., Rajan M.G. Comparison of serum thyroglobulin levels in differentiated thyroid cancer patients using In-house developed radioimmuno assay and immunoradiometric procedures. Indian Journal of Clinical Biochemistry. 2019 Oct; 34:465-71.
- [5] Crane M.S., Strachan MW, Toft A.D., Beckett G.J. Discordance in thyroglobulin measurements by radioimmuno assay and immunometric assay: a useful means of identifying thyroglobulin assay interference. Annals of Clinical Biochemistry. 2013 Sep;50(5):421-32.

Up-gradation of Animal House from a Conventional one to a State-of-the-art Facility

Experience at BARC’s Radiation Medicine Centre in Mumbai

Yogita Shete and Sandip Basu

Radiation Medicine Centre, BARC, Mumbai-400012.
E-mail: yogeshwarivet@gmail.com

Introduction

The ‘Animal House facility’ (AHF) in a research healthcare setting is a broad terminology that encompasses the housing of the small or large laboratory animals. By the definition it connotes a place where animals are housed either for breeding or for experimental work or both for the purpose of pre-clinical use. In the guidelines, the laboratory animals (also referred to here as animals) are defined as any vertebrate animal produced for or used in research, testing, or teaching (Guide, 2011). Generally, laboratory rodents are extensively used for biomedical research and pharmaceutical industries for testing and evaluation of safety margin for human and veterinary medicine (Barre-Sinoussi & Montagutelli, 2015).

At the Radiation Medicine Centre, BARC, Parel, the Animal house facility is running since 1963, keeping the view of its importance towards the development and evaluation of new radiopharmaceuticals and examining its in vivo quality control before administration in the patients. Principally, the RMC Animal House facility is a conventional experimental animal facility, where conventional work culture was adopted as compared to barrier facility or animal bio-containment facility protected by providing additional barriers, advanced instruments with multiple controlling systems like environmental control, engineering control and enrichment facility for the animals. However, in each animal facility, the risk factors are different and it depends on the use. To mitigate the risk factor, it must be identified and a strategy plan must be made to define an acceptable level (NIH guidelines, 2019).

Over the period of time, new advancements and updated guidelines have been formulated for animal usage used with the intent of its application with humane care and they are followed worldwide. To ensure ethical humane care and scientific requirements in laboratory animals, a defined program is started to address the esteems of animal value. This forms the core requirements of the guidelines and an important system and support for self-regulation (Klein and Bayne 2007). To have better scientific outcome from the animal experiments, animal husbandry practices, animal house designs, layout planning and minimum requirement needs to be defined as per the national and international guidelines (AALAAC, CCSEA guidelines 2018).

The animal house facility at RMC is involved in various animal experiments primarily for development of new PET, SPECT and therapeutic radiopharmaceuticals, their biodistribution studies and development of polyclonal antibodies for radioimmunoassay (Fig.1). Different laboratory animals like rats, mice, rabbits and immunocompromised animals are employed to this purpose. The use of small animal models constitutes an important & integral part of testing of new radiopharmaceutical agents and its mandatory

requirement from the regulatory clearance authority for human trials (Pawar et al., 2020). As mentioned before, the animal bio-containment and radioactivity are the two hazards of working within the facility. Therefore, the modification of conventional animal house layout to demarcate specialized work areas was planned. All the necessary approvals obtained from different safety committees of BARC like RMC local safety committee, ULSC-RO and OPSRC, and additionally, from the animal ethics committee from BARC. For minor structure changes approval from DCSEM, Civil Engineering Department, Vikram Sarabhai Bhavan, Anushaktinagar and the Civil Engineering Department, Tata Memorial Hospital, Mumbai was obtained.

The main Objective and Spectrum behind the AHF Modification was Characterized as follows

Animal research facilities involved with animal experiments & radioactivity work are considered to harbour bio-hazardous factors. Therefore, the facility associated concerns and risk factors are accordingly considered and addressed. To meet all the requirements at an acceptable level it is wise to construct the facility with versatility built-in to allow for a wide range of research projects and ensure safe environment.

The existing layout of the facility is as follows

Total number of Rooms- 9; Animal Colony: 3, Radioactive work: 1, Waste storage: 1, Quarantine Room: 1, Autoclave and Washing:1, Staff seating and Feed storage: 1, Animal House Admin: 1.

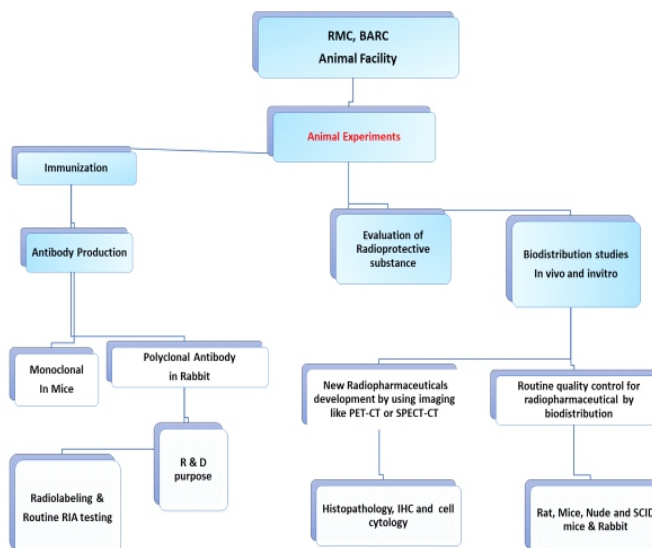


Fig.1: Work function of RMC, Animal House Facility.

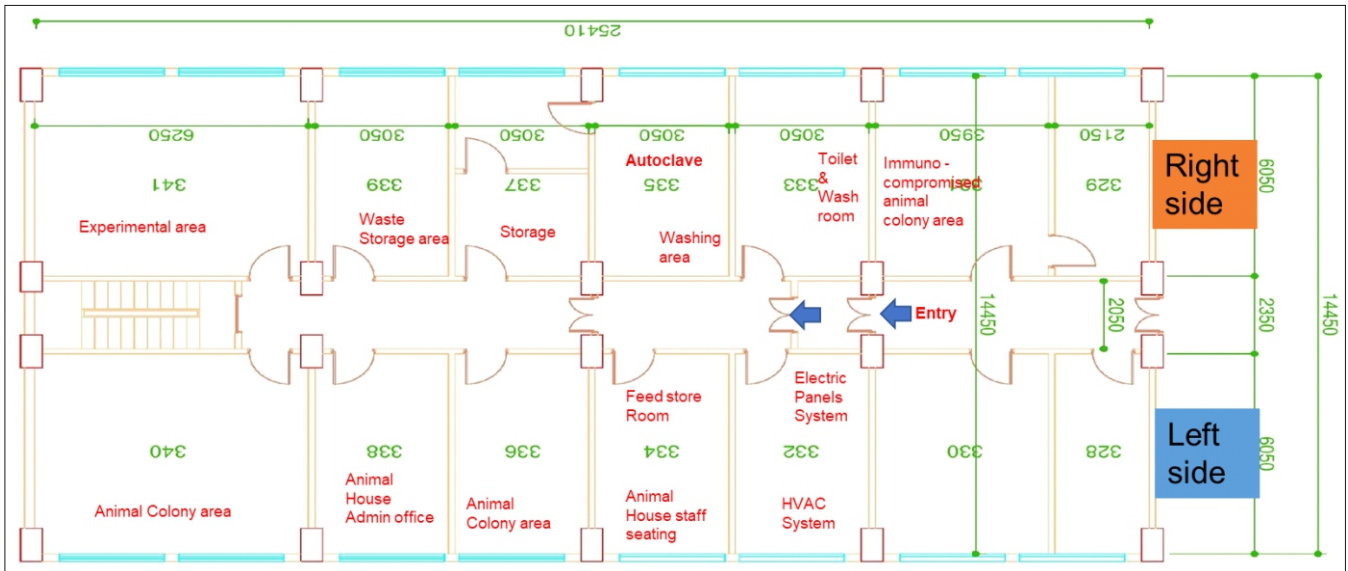


Fig.2: Current Layout of the RMC Animal House Facility.

Considering the current layout and mandatory requirement of safety guidelines the above modification was planned and approved by the different BARC safety councils.

To manage the work-safety and control or reduce the hazards elimination, substitution, engineering controls, good work practices and use of personal protective equipment kit must be considered (Wald and Stave, 2003). However, in view of the space constraints and necessity of the facility, the elimination and substitution of hazards components were unable to be implemented. Therefore, a modification of plan was made with the AHF design rearrangement, engineering control, good work practice, advanced instrument control, barrier construction like air barrier, physical barrier, use of PPE kits and training for the staff. These were considered to mitigate the associated risk factors and generate a safe working environment.

Modified layout of the Animal House Facility at RMC (BARC), Parel

Total Rooms - 9; Animal Colony: 3, Radioactive work: 1, Waste storage: 1, Quarantine Room: 1, Autoclave and Washing

:1, Analyzer and Feed storage: 1, Animal House Admin and Staff seating: 1, Access control with read circle.

Limited access control to the facility: The animal house staff and the administrative authority have access control cards for the facility. The electronic access control cards are provided to the animal house staff and facility related authority to have limited authorised access during working hours. Radioactive work areas with limited access control with manually operated systems are provided. There is no access to the other staff/common public. The facility common passage is under CCTV surveillance monitored by RMC, security staff and security have main door key withdrawal authority post working hours for the general surveillance (Fig.4).

Engineering control in facility: There are controls on air flow, the flow rate being done by the central heating, ventilation, and air conditioning (HVAC) system and effective centralized exhaust system. The air flow within the animal colony will be maintained. A standard 15 to 18-air changes per hour is maintained in the animal colony. The additional air curtain lock was planned to fit outside each animal housing room.

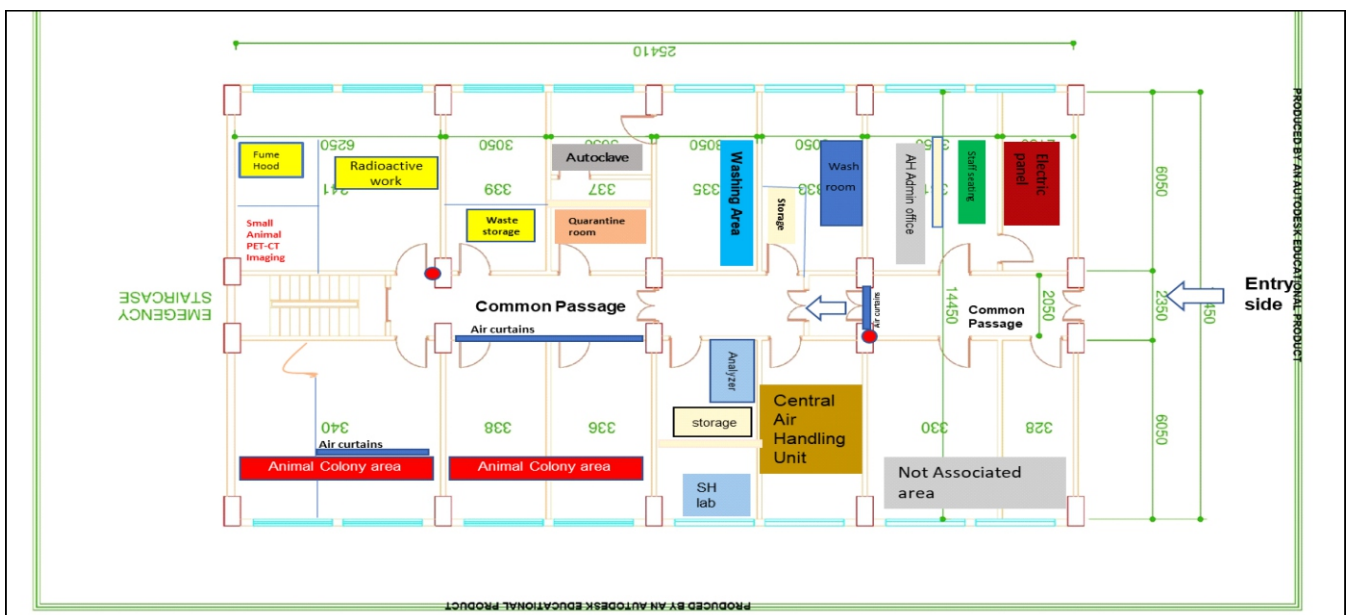


Fig.3: Modified layout of the Animal House Facility at RMC (BARC), Parel.



Fig.4: Electronic Door Lock: Access control door lock facility for animal house main entrance door.



Fig.7: Fume-hood facility: Employed for handling radioactivity for animal experiments.



Conventional cage system

IVC cage system

Fig.5: Conventional cage system upgraded to IVC cage system for rats.



Fig.8: Single Door High-Pressure High-Vacuum (HPHV) semi-automatic rectangular autoclave: Sterilization of cages, water bottles, bedding material and disposable aprons.



Fig.6: Animal cage change station: Daily routine use for cage changes in the rat and mice.

Instrument control: It is employed for animal housing, associated daily husbandry practices and radiation safety. It is introduced as safe work practices when working with animals and radioactivity.

■ Individually ventilated cage (IVC) system: A new individual ventilated cage system is installed for the wistar rats. The system is very much safe for the handlers and animals or vice-versa as filtered air goes inside and filtered air comes outside (Fig.5).

■ Animal Cage Change station: It is used routinely to change the cages of the animals. Due to its pre-filter and HEPA filter system, it protects the staff working with animal allergens. Hence it will provide health safety to the workers and animals (Fig.6).

■ Fume-hood: New fume-hood is fabricated as per the space availability and requirements. The work involving radioactivity in animal experiments is handled, injected and disposed off inside the fume-hood only (Fig.7).

■ Steam sterilizer: Introduction of single door High-Pressure High-Vacuum (HPHV) semi-automatic rectangular autoclave is used on daily basis for sterilization of animal cages, bedding material and water bottles. It helps to keep the bacterial contamination in check (Fig.8).

■ Animal tattooing machine: Animal marking is important in specifying experimental groups. Tattooing is done with AIIMS ink and tattooing machine with recommended ink and pattern. This is useful in identification of animals and prevents the missing of animals or reading wrong data related to human errors (Fig.9).

■ Veterinary Haematology Analyzer: Periodical animal health monitoring is a much-required aspect of AHF facilities. The parameters are standardized for laboratory animals like mice, rats and rabbits. This will be useful for rapid screening of any health issues in the animals.

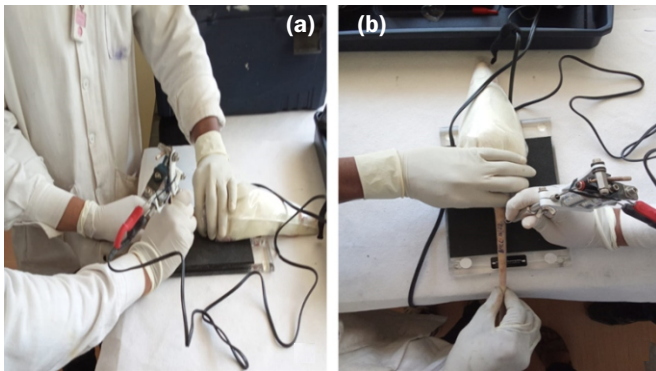


Fig.9: Animal marking with tattooing machine: (a) One person holding the animal cone and another person holding the tattooing gun for marking. (b) Process of 'Tail tattooing' by using tattoo machine.

■ Serum Biochemistry analyzer: Serum biochemistry machine helps in the identification of different organ functions based on levels of enzymes, hormones, proteins and waste products generated during the process of metabolism. They are useful for subclinical case identification and subserve as markers for animal health status (Fig.10).

■ Air curtains: Air curtains are provided outside each animal colony door, radioactive work area and at the main entrance of the facility. It will improve the air quality inside and outside of the working area (Fig.11).

■ Enrichment in the animal cages: Laboratory animals are considered social animals and hence measures taken to enhance natural physical activity and normal behaviours within the captive animals. Minimum enrichment should include nesting material, refuge area, tunnels and cons for small rodents like rats and mice (Fig.12). In rabbits chew sticks, hay blocks and nest boxes can be provided. The enrichment aids in maintaining and improving the quality of captive animals, decreasing the frequency of abnormal behaviour, and having a positive impact on the research outcome (Baumans, 2005).

■ Biosafety cabinet: The biosafety cabinet will be utilized for animal work that is not radioactive, including injections, administration, blood collection, and dissection for organ collection and necropsies. By doing this, contamination in the working area is reduced and thereby staff safety will be enhanced.



Fig.10: Veterinary Haematology and serum biochemistry analyzer: (a) Haematology Analyzer. (b) Serum Biochemistry analyzer.



Fig.11: Air Lock System: Animal colony with air curtain and limit switch at entry door.



Fig.12: Enrichment of animal cages with tunnels & nesting material: (a) Mice using the tunnels (b) Nesting material collection by individual mice (c) Mice using nesting materials and (d) Tunnels in mice colony.

■ Radiation monitoring unit: Area Gamma Monitor is installed in radiation experimental area for monitoring the area.

Personal Safety

To achieve personal protection disposable apron, disposable face mask, plastic/cotton shoe covers, head cap, double gloves are kept inside the facility. Staff/Person/Students who wish to enter inside the animal house needs to wear before entering inside the animal facility. Staff/Person is wearing personal protective equipment (PPE), which will protect the user against health or safety risks at work and reduce the contamination, generation of aerosols and small dust particles transmission from human to animal and animals to humans. Personal radiation monitoring batches like Thermoluminescent Dosimeter (TLD), Pocket dosimeters used by the staff while handling the radioactivity in animals. Animal house entry and exit must be done in the animal house log book with date and time.

Conclusion

The inclusion of laboratory animals is essential for pre-clinical studies along with maintenance of proper husbandry and in-vivo imaging techniques to assess the data. In pre-clinical veterinary nuclear medicine facilities, similar to other veterinary practices, risk evaluation is a crucial rational process that should safeguard the animals, working staff and the environment. The major experimental work involved is

either imaging or biodistribution. The radioactivity associated risk factor begins with the injections, handling, restraining during procedures like transporting, imaging, biological sample collections and euthanasia during the experiments. To mitigate the experimental risk factors, standard operating procedures like use of sedative drugs during injections, animal restraining instruments, use of a partial containment system with air flow control etc for each study need to be defined. This will enhance the safety of the personnel working with the animal. During the procedure, use of anaesthetics drugs, animal carrying containment box with cotton & absorbent sheets, animal holding baskets increases the distance and shielding from radioactivity injected animals. It additionally safeguards the working environment. The personnel protective clothing, monitoring batch, gloves, mask, safety shoes or shoe cover ensure the workers' safety. Application of safety equipment, good husbandry practices with general radiation safety principle (time, distance and shielding) generate a safe environment for both animals and humans. However, it is a complex approach that necessitates regular evaluation and discussion of hazards that may come from the infectious agents within the animals, radiation safety and different research protocols.

In conclusion, knowledge, expertise, training, and the precise safety of the equipment and features of facility design are crucial factors to perform safe research and disposal of biocontainment within the facility. In this direction, the use of well-defined research and routine protocols in containment are especially important when animals and radioactivity are used and are evolved further based upon unexpected situations that may occur from time to time.

References

- [1] Klein H.J., and Bayne K.A., 2007. Establishing a culture of care, conscience, and responsibility: Addressing the improvement of scientific discovery and animal welfare through science-based performance standards. *ILAR journal*, 48(1), pp.3-11.
- [2] NIH guidelines for research involving recombinant or synthetic nucleic acid molecules (NIH guidelines) April 2019.
- [3] AAALAC (2022). Association for Assessment and Accreditation of Laboratory Animal Care (AAALAC) International. Frederick, US. https://www.aaalac.org/14-accreditationprogram/directory/directory-of-accredited-organizations-searchresult/nocache=1#adv_acc_dir_search. Accessed on 2 nd November 2022.
- [4] Wald P.H. and Stave G.M., 2003. Occupational medicine programs for animal research facilities. *ILAR journal*, 44(1), pp.57-71.
- [5] Yogita P., Hemant S., Agnivesh S., et al., 2020. The role of advance nuclear medicine imaging techniques in preclinical drug development and three R's in animal model. *JLAS.*, 6(2), pp. 11-13.
- [6] Wald P.H. and Stave G.M., 2003. Occupational medicine programs for animal research facilities. *ILAR journal*, 44(1), pp. 57-71.
- [7] Barre-Sinoussi F, Montagutelli X. 2015. Animal models are essential to biological research: issues and perspectives. *Future Sci OA.*, pp. 1:4.
- [8] Baumans, V., 2005. Environmental enrichment for laboratory rodents and rabbits: requirements of rodents, rabbits, and research. *ILAR journal*, 46(2), pp.162-170.

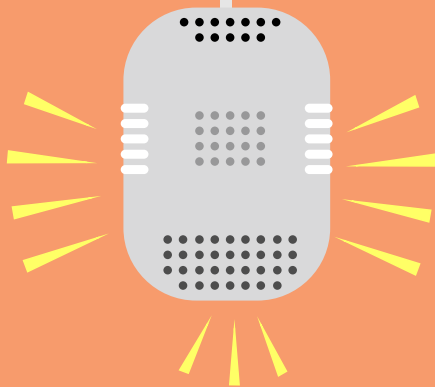


trombay
colloquium*
March 27 • 2024

Indigenous Indian Vaccine

The Story of Human Compassion & Cooperation

The story of human compassion, cooperation and resilience; on how India fought the Covid-19 pandemic valiantly. The stories of India's success and triumphs paying tribute to Indian scientists, doctors, health care/frontline workers, bureaucracy, defense services and the Indian citizens. The story of the development of the indigenous vaccine amidst all hindrances, doubts and naysayers.



Prof. (Dr.) Balram Bhargava
Chief of Cardiothoracic Centre, AIIMS

*The Trombay Colloquium is a key window of opportunity for the BARC community to brainstorm with eminent individuals belonging to a wide spectrum of science and allied domains. Prominent scientists and technologists are invited to BARC Trombay to deliver captivating talks on emerging domains of science, and the transformative effect of new technological innovations.

Water - The elixir of life

BARC water technologies now bring smiles to train commuters

Chemical Engineering Group & SIRD Editorial Team
Bhabha Atomic Research Centre, Trombay - 400 085, India

Bhabha Atomic Research Centre (BARC) has taken yet another stride in its pursuit to make available its water purification technologies for the benefit of wider sections of the society. Under the pilot project for demonstration and deployment of water technologies across India, BARC has joined hands with Indian Railways to cater to the drinking water requirements of commuters at prominent railway stations in Mumbai region.

Ten units of water purification systems equipped with BARC's ultrafiltration membrane technology were commissioned at busy railway terminals and stations, with 3 units capable of processing 750 litres per hour (lph) deployed at CSMT, 4 units of 500 lph capacity at LTT, 2 units of 500 lph capacity at Dadar; and 1 unit of 750 lph capacity at Dockyard Road Station were deployed on a pilot mode.

These water purification-cum-dispensation units were officially handed over on 27th of January this year. Senior scientific officers of BARC, Department of Atomic Energy (DAE) and Indian Railways officials and BARC technology partner (licensee) M/s. Osmotech Membranes Pvt. Ltd graced the event.

BARC water technologies are characterised for their uniqueness, cost-effectiveness, and place-and-case-specific membrane-based robust systems for effective treatment of ground/surface water to make water free from suspended solids, microbial contamination, arsenic, iron, fluoride, heavy metals, nitrate and salinity etc., both at domestic as well as community-scale.



Senior officials of DAE, BARC and Indian Railways present during the handing-over ceremony of water purification systems. BARC Photo.



Above: BARC technology equipped water purification-cum-dispensation unit commissioned at CSMT railway station, Mumbai. BARC Photo.

Reports from conferences, theme meetings and workshops



NSD-2024

BARC celebrates National Science Day

National Science Day is celebrated every year to commemorate the discovery of 'Raman Effect' by India's eminent scientist and Nobel Laureate Professor C.V. Raman. For this year's edition of National Science Day during 28th February to 1st March, 2024, BARC celebrated the event with the pertinent theme of Atoms for Society: Securing Water, Food, and Health to showcase its unique feats in areas of science and technology which are considered an integral part of our day-to-day lives. The event was jointly organized by Chemical Engineering Group and Bio-Science Group, BARC. The welcome address of the event was delivered by Dr. A.K. Tyagi, Director, Chemistry Group and Director, Bio-Science Group, BARC. The introductory addresses were delivered by Shri Vivek Bhasin, Director, BARC and Dr. A.K. Mohanty, Chairman, AEC and Secretary, DAE. Prof. K. Vijayaraghavan, Homi Bhabha Chair Professor was the chief guest of the occasion and delivered the inaugural address.

In his address, Prof. Vijayaraghavan stressed about the role of BARC in coming up with new technologies for societal applications along with the nuclear applications. A souvenir on the event theme was released by the Chief guest. The vote of thanks was delivered by Dr. Sulekha Mukhopadhyay, Head, Chemical Engineering Division, BARC. There were three invited talks by veterans of BARC topics related to water, food and health, respectively. The event saw participation of 700 students and teachers from 34 schools in the vicinity of Mumbai. The 3-day program covered audio-visual presentations, quiz competitions, skits. An exhibition was also held to showcase the latest scientific and technological achievements of BARC in vital areas of food, water, and health.

Reports from conferences, theme meetings and workshops



Participants of the 5-day practical training course pose for a photograph at A-Block Auditorium in BARC, Trombay.

BARC, Central Ground Water Board **join hands for Capacity Building in Isotope Hydrology**

The Isotope and Radiation Application Division of Radiochemistry and Isotope Group (RC&IG) of BARC conducted a practical training course on Isotope Techniques and their applications in groundwater studies for the officers of Central Ground Water Board (CGWB, Govt. of India) during January 8-12, 2024. Twenty three officers from 19 different states of the country have been trained in this course.

The exercise involved training of CGWB officers on various aspects that are key to carrying out isotope hydrological investigations, starting from sampling to measurements using advanced equipment to interpreting the isotope data to arrive at more precise conclusions.

The participants were handed over completion certificates by Dr. P.K. Mohapatra, Associate Director, RC&IG, BARC and Dr. H.J. Pant, Head, IRAD, RC&IG during the valedictory event of this 5-day program.

At the request of Jal Shakti Mantralay, Government of India, BARC started this training course on Isotope Hydrology for Water Resources Development and Management for officers of CGWB in the year 2022. The current one is second in the series and coordinated by Dr. K. Tirumalesh, Head, Isotope Hydrology Section, IRAD.

The training course includes theory classes held at Rajiv Gandhi National Ground Water Training & Research Institute (RGNGWTRI), Raipur and practical demonstration at IRAD in BARC, Trombay.

Newly erected fountain in the precincts of Van de Graff facility in BARC Trombay



Edited & Published by
Scientific Information Resource Division
Bhabha Atomic Research Centre, Trombay, Mumbai-400 085, India
BARC Newsletter is also available at URL:<https://www.barc.gov.in>